Doctoral Dissertation
Doctoral Program in Metrology (36^{th}cycle)

Applied Metrology for the digital transition in Healthcare

A metrological approach to the development of assistive solutions for *Health 4.0*

By

Luigi Duraccio

******

Supervisor(s):
Prof. Nicola Donato, Supervisor
Prof. Pasquale Arpaia, Co-Supervisor

Doctoral Examination Committee:
Prof. Guido Perrone (President), Polytechnic University of Turin
Prof. Emanuele Piuzzi (Reviewer), Sapienza University of Rome
Prof. Francesco Lamonaca (Reviewer), University of Calabria
Prof. Yuval Golan, Ben-Gurion University of the Negev
Prof. Nicola Giaquinto, Polytechnic University of Bari

Politecnico di Torino
2023

Declaration

I hereby declare that, the contents and organization of this dissertation constitute my own original work and does not compromise in any way the rights of third parties, including those relating to the security of personal data.

Luigi Duraccio
2023

* This dissertation is presented in partial fulfillment of the requirements for **Ph.D. degree** in the Graduate School of Politecnico di Torino (ScuDo).

To those who strive for a better future

Acknowledgements

Italian

Il momento della difesa della propria tesi di dottorato rappresenta senz'altro la conclusione di un percorso caratterizzato da innumerevoli passaggi significativi. La ricerca, come d'altronde la vita, è un cammino meraviglioso, ma spesso irto di ostacoli: non sempre tutto va come schedulato ed il fallimento è sempre dietro l'angolo. Tuttavia, è anche grazie a questi momenti negativi che si ha l'opportunità di migliorare e di raggiungere i propri traguardi. Questi tre anni, non ho dubbi, hanno contribuito a rendermi una persona migliore, prima che un buon ricercatore. Ho avuto modo di ricevere suggerimenti, imparare dagli errori, affrontare problemi, sbatterci la testa, sudare sette camicie, risolverli, e poi gioire.

E tutto ciò non sarebbe stato possibile da solo. Ho sempre creduto nell'importanza di fare squadra, di essere parte di qualcosa e lavorare per un obbiettivo che non riguardasse solo le proprie ambizioni, ma che andasse anche oltre.

Per questo motivo, non posso fare a meno di ringraziare tutti i membri di *ARHeMLab* con cui ho avuto la fortuna di interagire nel corso degli anni, con una menzione speciale per il Prof. Pasquale Arpaia, che ne è a capo, e per il Prof. Egidio De Benedetto, che ha avuto la pazienza di confrontarsi quotidianamente con me.
Un ringraziamento sentito va anche ai Proff. Marco Parvis e Nicola Donato, i quali mi dato l'opportunità di accedere al percorso di dottorato di ricerca presso il Politecnico di Torino.

Infine, ma non perchè meno importanti, ringrazio di cuore i miei affetti più cari, perchè so che ci saranno sempre per me ogni qual volta io ne abbia bisogno e perchè questo mio traguardo è un po' anche il loro. Grazie!

English

The moment of defending one's doctoral thesis undoubtedly represents the conclusion of a journey characterized by countless significant steps. Research, much like life, is a wonderful path, but often fraught with obstacles: things don't always go as scheduled, and failure is always lurking around the corner. However, it is also thanks to these negative moments that one has the opportunity to improve and reach their goals. These three years, without a doubt, have contributed to making me a better person, before being a good researcher. I have had the opportunity to receive suggestions, learn from mistakes, face problems, hit my head against the wall, work tirelessly, solve them, and then rejoice.

And all of this would not have been possible alone. I have always believed in the importance of teamwork, of being part of something and working towards a goal that goes beyond one's own ambitions.

For this reason, I thank all the members of *ARHeMLab* with whom I have had the privilege to interact over the years, with a special mention to Professor Pasquale Arpaia, who leads it, and Professor Egidio De Benedetto, who had the patience to interact with me daily.

A heartfelt thank-you also goes to Professors Marco Parvis and Nicola Donato, who provided me with the opportunity to embark on the doctoral research path at the Polytechnic University of Turin.

Lastly, but not least, I sincerely thank my family, my girlfriend, and my dearest friends because I know they will always be there for me whenever I need them, and because this achievement of mine is a bit theirs too. Thank you!

Abstract

This doctoral thesis discusses the design and implementation of a series of assistive solutions developed in the context of the digital transformation of the healthcare sector. Digital transformation in healthcare represents a highly relevant topic in the current socio-healthcare context. This process involves the adoption and integration of the enabling technologies derived from the fourth industrial revolution to improve the efficiency, accessibility, and quality of healthcare services. For this reason, it is often referred to as *Health 4.0*. Among the main challenges addressed are the digitalization of clinical data, the implementation of telemedicine systems, the use of Artificial Intelligence for medical data analysis, the enhancement of clinical treatments, and the security of healthcare information.

In the era of Health 4.0, where digital technologies revolutionize healthcare, metrology is pivotal. As a matter of fact, the integration of metrology with Health 4.0 technologies, including Artificial Intelligence (AI), Internet of Things (IoT), and Augmented Reality (AR), enhances precision in measurements, ensures data accuracy, and contributes to the reliability of advanced healthcare systems. It provides a foundational framework for calibration, quality assurance, and standardized measurements, fostering the seamless convergence of digital innovations in healthcare.

Going into the details of this work, the first Chapter briefly provides a historical overview of the four industrial revolutions that have marked the past centuries. Subsequently, particular attention is devoted to the introduction of enabling technologies of the *4.0* paradigm, such as Augmented Reality, Artificial Intelligence, and the Internet of Things. The Chapter concludes by explaining how the principles underlying the fourth industrial revolution can also be applied in other contexts, including healthcare, demonstrating new declinations and their respective benefits with respect to traditional practices.

Subsequently, this doctoral thesis elucidates the aforementioned assistive solutions. Chapter 2 focuses on the development of Brain-Computer Interfaces based on Steady-State Visually Evoked Potentials induced through Augmented Reality technology, aiming to create highly wearable and portable systems not confined to laboratory settings. In a nutshell, Brain-Computer Interfaces are an integration of hardware and software systems that establish a direct communication path between users and external devices. After a metrological analysis of the performance of the developed systems, two illustrative application scenarios are briefly presented, demonstrating the efficacy and potential of such systems. The first scenario delineates a hands-free interaction mode within an operating room by the medical team. This mode facilitates the monitoring of both the patient and their health status through augmented reality visualization of vital parameters. The second scenario highlights an innovative therapy approach for school-age patients with attention or learning disorders. In both cases, the developed system exhibits capabilities that surpass traditional systems.

Chapter 3 describes the development of a patient monitoring system in the operating room based on Augmented Reality. Traditionally, the medical team is divided between monitoring the patient's vital parameters displayed on the electromedical instrumentation monitors and those who directly operate on the patient. Sometimes, the shortage of medical staff necessitates performing both tasks, occasionally risking distraction and an inability to respond promptly in case of deteriorating patient health conditions. For this reason, the developed system aims to display the patient's vital parameters in real-time through augmented reality to the medical team, ensuring that the operators do not lose sight of the patient and can act promptly in case of danger. In this case as well, a metrological characterization of the system has enabled an understanding of its performance in terms of communication accuracy and latency, demonstrating how such a system can be effective and efficient compared to traditional practices.

Chapter 4, finally, describes the development of two clinical decision support systems. In brief, a decision support system is a system that, based on collected data, provides real-time objective information to the medical specialist. Systems of this kind find application especially in contexts where decisions are made based on the experience of the medical specialist. In this thesis work, two systems are presented. The first system concerns the evaluation of the effectiveness of scoliosis braces. Specifically, the system is based on the acquisition and processing of thermal images

of the patients' backs collected through infrared thermography instrumentation. The temperature difference measured between different areas of the patient's back is caused by the varying pressure exerted by the brace in different back zones. The system can provide a statistically-based result regarding the correctness of the applied pressure and, therefore, the effectiveness of the brace, thus avoiding frequent X-ray prescriptions, which can be harmful to the patient.
The second system, on the other hand, relates to the assessment of perfusion quality in the field of laparoscopic surgery: following an intervention in the intestinal tract, it is crucial to know the quality of perfusion to determine whether it is necessary to intervene again on the patient or not. The proposed system takes input from the video streaming from the endoscope that analyzes the relevant intestinal tract. Subsequently, image processing allows for a statistical understanding of perfusion quality, providing the physician with objective support, especially in cases where making a decision through simple visual inspection, as traditionally done, is challenging.

All the systems presented have been meticulously designed and developed, taking into consideration the stringent requirements of the healthcare sector. For this reason, appropriate metrological characterizations of the functional components have been conducted to assess the performance of the systems in anticipation of their future utilization in everyday healthcare practices

Contents

List of Figures

List of Tables

Chapter 1

The *Fourth Industrial Revolution*

The first Chapter of this Dissertation describes the *Fourth Industrial Revolution*, also known as *4.0 Revolution* or *Digital Trasformation*. Then, after the description of the 4.0 enabling technologies, the manuscript focuses on the transition from the industrial to the healthcare application context.

1.1 A bit of history

Over the centuries the world has witnessed four industrial revolutions, the last of which is still ongoing [8].

The First Industrial Revolution, spanning from the latter part of the 18th century to the early 19th century, denoted a noteworthy change in manufacturing methods and shifts within society. This transformation was marked by the mechanization of manufacturing via the inception of steam propulsion and the evolution of novel apparatus. The utilization of steam engines facilitated the substitution of manual toil with mechanisms, consequently fostering elevated efficiency and the emergence of industrial plants. Among the fields that encountered profound alterations during this phase, the textile domain stood out, benefiting from innovations like the spinning jenny and power loom, which fundamentally reshaped textile fabrication [9].

The Second Industrial Revolution, extending from the mid-19th to the initial period of the 20th century, ushered in additional progress primarily propelled by the introduction of electricity, the expansion of railway networks, and the maturation of telegraphy and telephony. These technological breakthroughs expedited the swift expansion of sectors such as steel, chemicals, and petroleum. The adoption of assembly lines and techniques for mass production, as epitomized by Henry Ford's implementation of the progressive assembly line in the automobile realm, contributed to heightened efficacy and reduced manufacturing expenses. This epoch was equally defined by scientific revelations and innovations, encompassing the formulation of the laws of thermodynamics and the refinement of internal combustion engines [10].

The Third Industrial Revolution, often referred to as the Digital Revolution, emerged in the latter half of the 20th century with the advent of electronics, computers, and the internet. This revolution witnessed the automation of various processes, the miniaturization of electronic components, and the integration of computer systems into industrial processes. Key developments during this period include the invention of the transistor, the development of integrated circuits, and the establishment of computer networks. The widespread adoption of computers and the internet revolutionized communication, information sharing, and data processing, laying the foundation for the knowledge-based economy [11]. This transformation of production processes and the evolution of the manufacturing industry made possible the development of the Information and Communication Technology (ICT) field, which refers to a broad and dynamic field that encompasses technologies, services, and systems related to the gathering, processing, storage, transmission, and presentation of information. It includes both hardware and software components and plays a pivotal role in modern society and the global economy. The ICT sector is responsible for driving technological innovation, facilitating communication, and enabling the current digital transformation in various frameworks.

The Fourth Industrial Revolution, a term coined by Klaus Schwab and also acknowledged as Industry 4.0 or the Digital Transformation era, constitutes the ongoing phase of transformation wherein digital technologies are converging with physical frameworks, resulting in the development of the cyber-physical realm. This revolution is distinguished by the convergence of the *key enabling technologies*, such as the Internet of Things (IoT), Artificial Intelligence (AI), Big Data Analytics, Robotics, Additive Manufacturing, Cloud Computing, and Augmented Reality (AR). The interlinking of devices and systems permits the instantaneous accumulation of data, its analysis, and the process of decision formulation. Industry 4.0 endeavors to establish intelligent and adaptable production systems capable of accommodating evolving requisites, thereby facilitating tailored and effective manufacturing procedures [12].

For the sake of comprehensiveness, Fig. 1.1 shows a graphical representation of the four industrial revolutions, while in the following Section, further details regarding the key 4.0 enabling technologies will be provided.

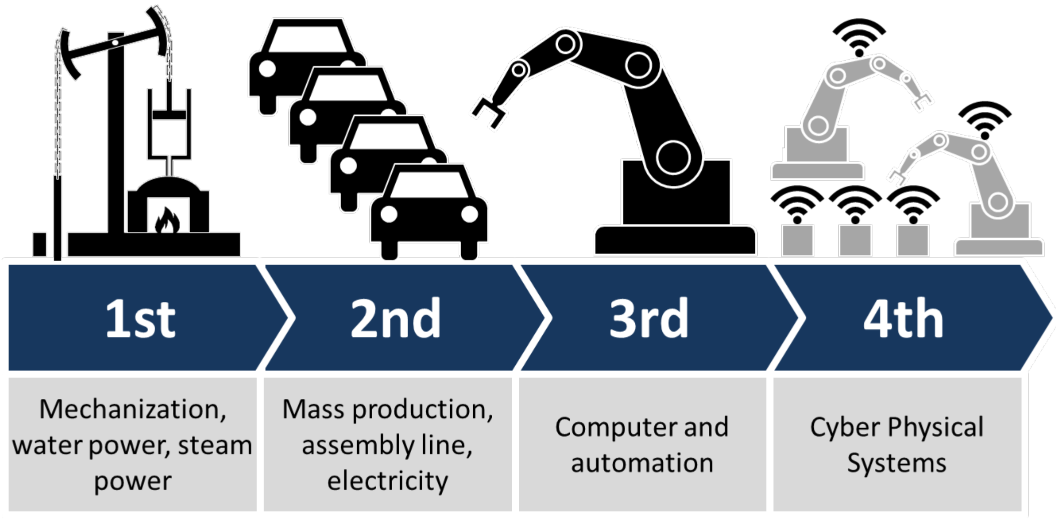

Fig. 1.1 Sketch of the four industrial revolutions. Image taken from [1].

1.2 The 4.0 enabling technologies

Industry 4.0 isn't defined by a singular technology; instead, it represents a collection of various technological elements that are effectively combined by leaders in technology, influential users, integrators of systems, and policymakers in governance [13]. More in detail, the technologies are:

- *Internet of Things (IoT)*: IoT includes devices with self-identification capabilities (localization, status diagnosis, data acquisition, processing, and execution) linked through standard communication protocols. Such technologies find use in 4.0 manufacturing scenarios and various other domains (housing and construction, automotive, environment, smart city, agriculture, etc.). Regarding Industry 4.0, IoT implementations pertain to what's often referred to as the *industrial Internet*.

- *Big Data Analytics*: it involves techniques and instruments for managing extensive data quantities in manufacturing, supply chain control, and maintenance. Data can originate from IoT systems linked to the production layer (such as sensors and related apparatus) or from interactions between IT systems for production and warehouse management. Distinct applications in this field encompass machine learning tools for prediction, projection, anticipatory maintenance, and simulation.

- *Cloud Manufacturing*: it involves incorporating cloud technologies into manufacturing, offering widespread accessibility and convenient, on-demand IT services—such as infrastructure, platforms, or applications—to bolster production procedures and supply chain control. Cloud manufacturing encompasses the virtualization of essential physical resources for factory equipment, as well as application data and processes spanning various platforms, execution, and collaborative tools, all hosted in the Cloud.

- *Robotics*: the robotics cluster involves SCARA, Articulated, Cartesian, Dual Arm, and Co-bots as distinct methods for automating production tasks. Sophisticated automation encompasses cutting-edge advancements in production systems, enhancing their capacity to engage with surroundings, self-learn, provide automatic guidance, and employ vision and pattern recognition.

- *Artificial Intelligence (AI)*: it involves the understanding and methodologies designed to imbue machines with *intelligence*, enabling them to operate effectively by anticipating conditions within their application environment. In the industrial context, AI pertains to computer science-driven technologies that, in conjunction with machine learning, are applied to create intelligent sensors, edge computing, and smart production systems."

- *Additive Manufacturing*: also referred to as 3D Printing, Additive Manufacturing serves various purposes, from prototyping (to aid in product development, static simulation, wind tunnel testing, etc.), to manufacturing (direct production of items), maintenance and repair, as well as modeling stages. The US International Standard Organization outlines seven categories of additive manufacturing processes: Binder Jetting, Directed Energy Deposition, Material Extrusion, Material Jetting, Powder Bed Fusion, Sheet Lamination, and Photo polymerization (according to ISO TC 261, 2011).

- *Augmented Reality (AR)*: this technology enhances reality by overlaying digital information and virtual elements onto the physical world. It empowers users to perceive an enriched environment where real-world surroundings are augmented with virtual objects, data, or insights. Within the realm of Industry 4.0, AR is harnessed to revolutionize manufacturing processes, supply chain management, and maintenance. By seamlessly integrating digital information into real-world scenarios, AR enhances productivity, collaboration, and decision-making, enabling businesses to achieve new levels of efficiency and innovation.

In the following Section, further details about the three technologies most adopted in this Dissertation will be provided, namely *Internet of Things*, *Articial Intelligence*, and *Augmented Reality*.

1.2.1 Internet of Things

The concept of IoT emerged during the 1980s at Carnegie Mellon, where a modified vending machine could report its inventory and signal the coldness of newly loaded drinks over the Internet. IoT gained popularity in 1999 at the MIT Auto-ID Center through Radio-frequency identification (RFID) [14, 15]. Correlated concepts were subsequently introduced by various companies including Olivetti, Xerox, IBM, as well as universities such as Carnegie Mellon and MIT. Siemens, however, took a significant step by introducing a machine-to-machine (M2M) GMS connected system back in 1995 [16, 17]. Open-source dynamics, as seen in many IT segments, propelled IoT development, evident from the adoption of the (open source-based) JXYA standard in 2003 as a universal peer-to-peer connectivity standard for electronic components. The technology's diffusion was further accelerated by the introduction of an affordable, single-board electronic controller in 2005 from the Interaction Design Institute Ivrea, resulting in the open-source electronics platform Arduino. This propelled IoT's relevance for chip manufacturers, sensors producers, gateway hardware providers, and software and machine developers for IoT platforms. IoT's foundational disciplines encompass computer science, communication and information technology, and electronics. Key technologies essential for constructing IoT devices involve semiconductor technologies, the internet, sensor technologies, and more broadly, microelectromechanical systems. In particular, IoT devices incorporate Bluetooth technologies, low-power battery technologies, laser technologies, smart camera technologies, smart meters, and energy consumption sensors. Amidst this diverse assortment of devices and solutions, at least three technological clusters emerge: devices, software platforms, and gateways along with other networking elements. Despite IoT technologies still being in an early developmental phase, they confront an unsettled competitive and technological landscape. Technical challenges include data exchange among large-scale heterogeneous network elements, adapting to uncertain information integration and interaction, and service adaptation within dynamic system environments. Structured data concerning R&D spending in IoT exist, though specifics about the Industrial IoT (IoT) subsystem are scarce. Investments in these technologies predominantly come from private companies. Notable investors include IBM, Google, Samsung, SAP, Dell, Siemens, and Intel [18]. Yet, pinpointing a definitive technology leader in both devices and platforms proves challenging due to the vast array of technologies and sectors involved. Intriguingly, the rising interest of major companies in acquiring IoT capabilities seems to be propelling a wave of industry consolidation, as evidenced by Google's acquisition of Nest and CSR, as well as Qualcomm's.

1.2.2 Artificial Intelligence

Efforts to automate human intelligence have a relatively extensive history [19], but the evolution of modern AI (a term coined in 1954 by John McCarthy as the theme of a Dartmouth conference) is intricately tied to advancements in computing technologies, alongside recent strides in machine learning and predictive methodologies. AI encompasses diverse research domains, often blurring precise boundaries. Nevertheless, its fundamental components include machine learning, deep learning, natural language processing platforms, predictive application programming interfaces (APIs), image recognition, and speech recognition. Global R&D investment in AI is rapidly escalating, stemming from internal research at major tech corporations' labs (such as Google and Baidu) as well as VC-funded start-ups, frequently backed by corporate resources. Investment estimates range between $25 to $35 billion [20]. Of these funds, machine learning garners the most substantial portion. As highlighted by Lee et al. [21], AI's impact on industrial applications has been somewhat limited thus far. However, industrial AI is rapidly advancing as a structured research discipline, concentrating on the development, validation, and deployment of dependable machine learning algorithms for industrial contexts [22]. Forecasts predict a significant surge in demand over the forthcoming years, with early industrial adopters mainly clustered in finance, banking, retail, and manufacturing sectors. Current industrial applications primarily center around autonomous robots, digital assistants, neurocomputers, machine monitoring and control systems, as well as expert systems such as healthcare decision-making and smart grid management.

1.2.3 Augmented Reality

Augmented Reality (AR) has a rich history of development [23], but its rise to prominence is closely intertwined with advancements in technology and recent breakthroughs in interactive interfaces. The origins of AR trace back to early experiments, but its modern conceptualization can be traced to crucial moments, including the introduction of wearable displays and interactive systems. The term *Augmented Reality* was coined as the technology matured and expanded its potential. Innovations in computer vision, spatial mapping, and display technologies, coupled with the rapid growth of mobile devices, transformed AR from a theoretical concept to a tangible and interactive experience. Today, AR technology finds application across diverse sectors, from gaming and entertainment to education, healthcare, and manufacturing. The development of AR software development kits (SDKs) and tools has enabled developers to create immersive and interactive experiences that blend digital and physical worlds. The advent of smart glasses and AR-enabled devices has extended the reach of this technology, making it accessible for users in various professional and personal scenarios. Augmented Reality's journey in industrial contexts has gained traction, with industries such as manufacturing, maintenance, and training exploring its potential. AR facilitates real-time data visualization, remote assistance, and interactive training modules. As AR continues to evolve, researchers and innovators are working to address challenges related to accurate tracking, seamless integration, and user-friendly interfaces, aiming to unlock AR's full potential in revolutionizing how we interact with the world around us. In terms of R&D investment, Augmented Reality is experiencing growing attention from both established technology giants and emerging start-ups. Companies like Microsoft, Apple, Google, and various tech conglomerates have invested heavily in AR development. The technology's capabilities are expanding through collaborative efforts, ecosystem growth, and continuous research into improving its applications and user experiences. In essence, Augmented Reality is on a trajectory similar to AI and IoT, with its development tightly entwined with technological advancements and a growing understanding of its potential. As it finds its way into mainstream adoption, AR holds the promise to reshape industries, enhance user experiences, and revolutionize the way we perceive and interact with reality.

1.3 From *Industry 4.0* to *Health 4.0*

The principles and driving forces of the Fourth Industrial Revolution have transcended their origins in manufacturing and found transformative applications in various sectors. Among these sectors, considerable attention should be given to healthcare. The integration of the 4.0 key enabling technology within the healthcare framework has given rise to the concept of *Health 4.0*, which represents a paradigm shift in healthcare practices. Health 4.0 leverages the power of intelligent technologies and data-driven approaches to enhance patient care, optimize operational efficiency, and revolutionize healthcare delivery [24, 5].

Digital technologies such as the Internet of Things (IoT), Big Data Analytics, Artificial Intelligence (AI), Augmented Reality (AR), and Robotics are seamlessly integrated into healthcare systems within the Health 4.0 framework [25]. This integration enables healthcare providers to transform the way care is delivered and opens up new possibilities for improving patient outcomes. At the core of Industry 4.0, the principle of connectivity finds a natural fit in healthcare, facilitating real-time data exchange and empowering clinical decision-making. By securely sharing and analyzing patient data, healthcare professionals can make more accurate diagnoses, provide timely interventions, and develop personalized treatment plans.

AI, a key component of Health 4.0, plays a pivotal role in processing and analyzing vast amounts of medical data. Through the utilization of machine learning algorithms, AI can extract valuable insights, predict disease outcomes, and enhance the accuracy of medical diagnoses. One notable application of AI in healthcare is the use of image recognition algorithms, which have proven effective in assisting radiologists in detecting abnormalities within medical scans. By aiding in early diagnosis and timely interventions, AI-powered image recognition algorithms contribute to improved patient outcomes [26].

Assistive surgery is another significant aspect of Health 4.0, which harnesses robotic systems and AI algorithms to enhance surgical precision and improve patient outcomes. Robotic surgical platforms enable surgeons to perform complex procedures with enhanced precision and dexterity. These platforms provide real-time imaging, haptic feedback, and assistance in intricate tasks, thereby augmenting the skills of the surgeon and reducing the risk of human error [27].

Moreover, the integration of augmented reality (AR) technologies in Health 4.0 has valuable applications in medical training, surgical planning, and patient education. AR visualization techniques allow surgeons to overlay virtual information onto a patient's anatomy during preoperative planning, enabling precise anatomical localization and improving surgical outcomes. Additionally, AR simulations enhance medical training by providing medical students and healthcare professionals with the opportunity to practice complex procedures in a safe and controlled environment [28, 29].

Also, in the last years, Brain-computer interfaces (BCIs) have emerged as transformative tools within the Health 4.0 framework, enabling direct communication between the human brain and external devices. BCIs offer significant potential in assisting individuals with neurological disorders, such as spinal cord injuries or stroke, by allowing them to control assistive devices through neural signals. For instance, individuals with paralysis can utilize BCIs to command robotic limbs, control wheelchairs, or even communicate through direct neural interaction, greatly improving their quality of life [30, 25, 31, 32].

The integration of these technologies has lead to the development of the *Decision support systems* (DSS), which provide healthcare professionals with evidence-based recommendations, predictive analytics, and personalized treatment plans. By analyzing patient data, clinical guidelines, and research literature, DSS can assist in accurate diagnoses, optimal treatment selection, and monitoring patient progress. These systems empower healthcare providers with timely information and enhance clinical decision-making, ultimately improving patient outcomes [7].

Therefore, in the transition to Health 4.0, the integration of AI, assistive surgery, AR, BCIs, and DSS offers significant opportunities for personalized and precise healthcare interventions. These technologies drive advancements in diagnostics, treatment planning, and patient empowerment, leading to improved healthcare delivery and overall well-being. Health 4.0 fosters a data-driven healthcare ecosystem, enabling continuous monitoring, proactive interventions, and preventive care. By leveraging the power of intelligent technologies, healthcare can transcend its traditional boundaries, ushering in an era of patient-centric care and transformative healthcare experiences. However, it is essential to address challenges such as data privacy, algorithm transparency, and ethical considerations to ensure the responsible and effective implementation of these technologies in healthcare settings [33].

In conclusion, Health 4.0 represents a groundbreaking revolution in healthcare, driven by the principles and driving forces of the Fourth Industrial Revolution. Through the integration of AI, assistive surgery, AR, BCIs, and DSS, healthcare systems can unlock new frontiers of patient care, clinical decision-making, and operational efficiency. While challenges and ethical considerations must be addressed, the potential benefits of Health 4.0 are immense, promising a future where healthcare is personalized, precise, and transformative. By embracing Health 4.0, we can shape a healthcare ecosystem that maximizes the potential of intelligent technologies and provides better outcomes and experiences for patients.

In the following Chapters of this Dissertation, different examples of assistive solutions in Healthcare will be provided. Each of these solutions was thoroughly designed and tested with a metrology-oriented approach in order to guarantee proper functionality. More in detail, Chapter 2 describes the design and development of Brain-Computer Interfaces relying on Visually Evoked Potentials and AR. Chapter 3 deals with the implementation of AR solutions to monitor patient's health in Operating Room. Chapter 4 describes two Decision Support Systems aimed at helping physicians during the decision-making process in the framework of scoliosis treatment and laparoscopic surgery, respectively. Finally, Conclusions are drawn.

Chapter 2

Brain-Computer Interfaces relying on Steady-State Visually Evoked Potentials and Augmented Reality

This Chapter presents the design and development of Brain-Computer Interfaces integrated with Augmented Reality technology. Brain-Computer Interfaces (BCIs) embody the fusion of hardware and software communication systems that enable a direct pathway of interaction linking the human brain to external devices. Among all the different BCI paradigms, Steady-State Visually Evoked Potentials (SSVEPs) have gained traction in the progress of non-invasive BCI applications, given their satisfactory signal-to-noise ratio and data transmission rate. Recently, the adoption of Augmented Reality (AR) head-mounted devices with this BCI approach has emerged as an appealing substitute for traditional computer screens. Indeed, the improvement in wearability of such systems foresees the chance of implementing BCIs in settings beyond research labs. In the subsequent segments, a comprehensive summary of the essential concepts for developing an SSVEP-based BCI is furnished. Thus, varied systems designed and implemented throughout the years are displayed and thoroughly compared to spotlight the enhancements in performance without losing sight of real-world application potential. Especially, a metrology-oriented strategy is taken up to gauge the system's effectiveness among diverse subjects. Lastly, two pertinent case studies, concerning the practical use of the proposed setup in children's rehabilitation and operating rooms are showcased.

2.1 BCI technology

This Section aims to provide readers with basic information regarding BCI technology, from relevant definitions to the typical classifications.

2.1.1 Definitions

Brain-Computer Interfaces (BCIs) represent an innovative communication system aimed at translating the activity of the central nervous system (CNS) into artificial outputs, facilitating seamless interaction between the human brain and computers [32]. This revolutionary technology enables communication pathways independent of the brain's usual output channels, such as peripheral nerves and muscles [34]. The transformative potential of BCI lies in its capacity to replace or restore natural CNS output that might have been impaired or lost, thereby opening up new frontiers in neurological rehabilitation. By leveraging various methods of interfacing, BCI serves a multitude of purposes, such as the restoration of sensorimotor functions [35], and the mapping of cognitive networks [36]. Moreover, BCI holds promise in augmenting and enhancing cognitive capabilities beyond their natural limits. Noteworthy examples include using BCI for communication through spelling systems [37], allowing individuals with motor disabilities to express themselves effectively [38]. Additionally, functional electrical stimulation of muscles is another remarkable application of BCI, promoting movement and mobility in individuals facing motor impairments [39]. These are just a few examples of application scenarios of BCIs.

Figure 2.1 illustrates the fundamental components of a generic BCI system, organized into four essential blocks: *signal acquisition*, *signal processing* (comprising *feature extraction* and *features translation* or *classification*), the *BCI application*, and the *feedback* loop to the user. Each of these blocks plays a crucial role in enabling the seamless flow of information between the brain and the computer.

1. The first step in the BCI process is signal acquisition, where neural activity is captured through non-invasive or invasive methods, depending on the application's requirements and the user's needs.

2. The acquired brain signals serve as the input to the signal processing block. Here, suitable algorithms typically analyze and extract essential features from

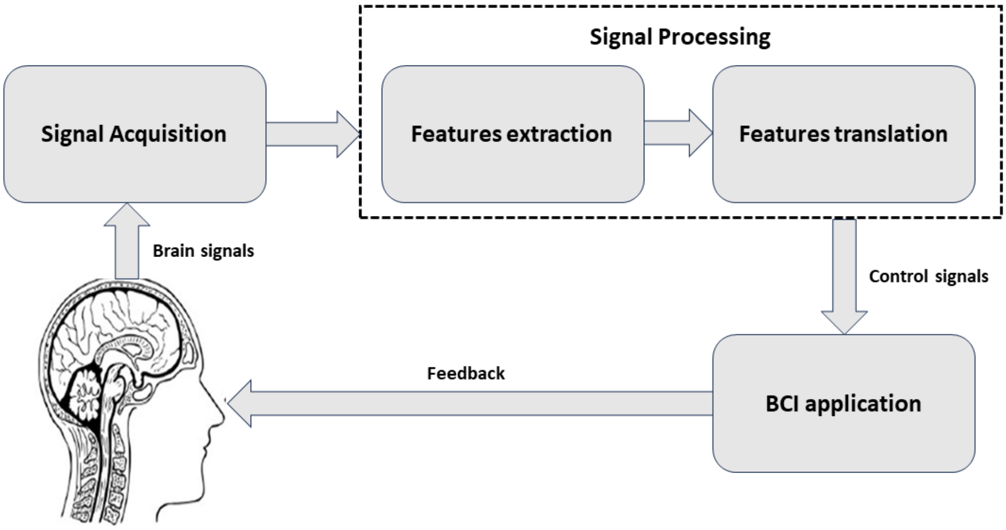

Fig. 2.1 Generic block diagram of a Brain-Computer Interface (BCI) system.

the brain data, preparing it for the classification stage. This critical stage is responsible for understanding the user's intent or action based on the recorded brain signals.

3. The next step involves the BCI application, where the interpreted signals are utilized to accomplish specific tasks or control external devices.

4. Finally, the BCI system closes the loop by providing feedback to the user. This feedback can take various forms, such as auditory, visual, or haptic cues, informing the user of their mental state or the successful completion of a task.

2.1.2 Taxonomy

BCI systems can be classified into various categories based on different taxonomies. According to [2] (and shown in Fig. 2.2), these systems can be distinguished into *Independent/dependent*, *Exogenous/Endogenous* , and *Invasive/Noninvasive*:

1. *Independent/dependent*, based on their reliance on additional types of brain activity in order to function. An independent BCI is designed to operate autonomously, without relying on the brain's normal output pathways involving peripheral nerves and muscles [40]. In this type of BCI system, the brain activity necessary for controlling the BCI is derived solely from the signals

recorded directly from the brain itself. In contrast, a dependent BCI relies on the brain's normal output pathways, which include the peripheral nervous system and muscles, to generate the necessary brain activity for the system to function effectively [2].

2. *Exogenous or endogenous*, based on the nature of the recorded signal. In exogenous BCIs, the systems utilize external stimuli to elicit the necessary brain activity for interaction with the machine, which is detected through EEG channels. These systems can achieve high information rates [41] and generally do not require extensive training. On the other hand, endogenous systems do not rely on external stimuli, necessitating users to acquire the skill of generating specific brain patterns. The training duration varies depending on the individual subject, the experimental strategy employed, and the training environment.

3. *Invasive/noninvasive*, based on the method of data extraction. Invasive systems involve the implantation of foreign materials into the subject's body, such as microelectrode arrays placed in the gray matter. Although this approach requires brain surgery, it offers better Signal-to-Noise Ratio (SNR) compared to non-invasive systems, as it avoids artifacts like eye blinking or movements and provides more spatially accurate signals. Invasive BCIs operate by monitoring single-neuron activity within the subject's brain, making them promising for repairing vision damage and enabling new capabilities for individuals with paralysis [42]. On the other hand, non-invasive BCI systems do not require any implantation, and users interact with the machine through wearable devices equipped with removable electrodes applied to the scalp [30]. However, the control signal obtained from non-invasive systems can be more challenging to interpret due to overlaps with signals from other brain areas and artifacts from muscle and eye movements. Additionally, signal resolution may be compromised due to losses caused by the bony surface of the skull and skin.

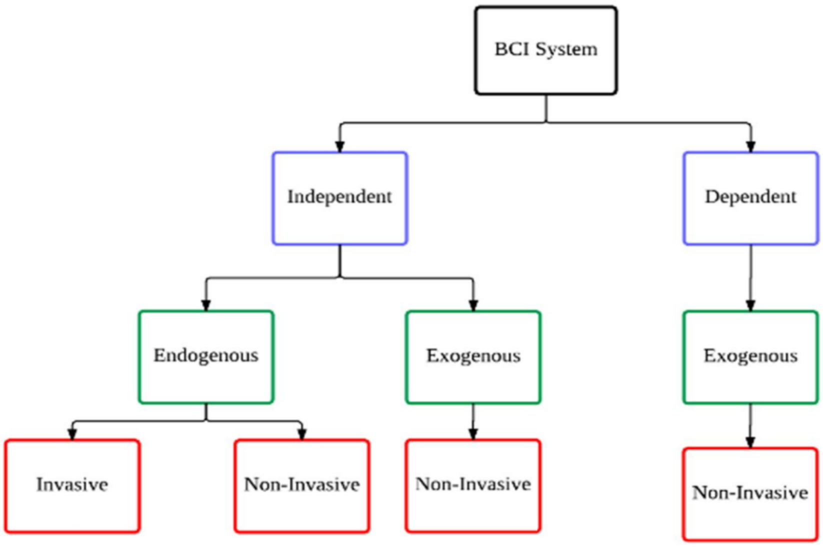

Fig. 2.2 BCI taxonomy according to [2].

Also, according to [43], BCIs can be also categorized into *Active*, *Passive*, and *Reactive*:

- *Active*: *"where the subject voluntarily produces an appropriate modulation of the brain waves for controlling an application, independently of external events"* [32]. *Active* BCIs are arguably studied in rehabilitation protocols [44], *"where the premise is that the neural activity within a specific region of the brain undergoes changes when subjects imagine moving any body part"* [32, 45–48].

- *Passive*, where the user does not directly and consciously control his electrical brainwaves. This category is generally used for monitoring the user's mental state [49] and in the field of affective computing [50].

- *Reactive*: *"where brainwaves are produced in response to external stimuli. This peculiarity allows the use of reactive BCIs both for control and monitoring purposes [32]"*.

Overall, active and reactive BCIs are employed for directed control, whereas passive BCIs facilitate the assessment and interpretation of changes in the user's state during Human-Computer Interaction. Active BCIs are commonly recommended for users with disabilities, while passive and reactive BCIs are intended for users without disabilities. The passive BCI is utilized to interpret the user's cognitive and emotional states, whereas the reactive BCI serves the same purpose as the active BCI, enabling direct control.

On the basis of these categorizations, many BCI paradigms have been developed over the years, each of them requiring the extraction of suitable features. Some of the most widely adopted paradigms are: *Slow cortical potentials (SCP)* [51], *Neuronal action potentials* [52], *Sensorimotor rhythms (SMR)* [53], *Event-related potentials (ERP)* [54], and *Sensory evoked potentials (SEP)* [55]. Specifically, SEPs are electrical potentials that can be detected by the central nervous system through electroencephalography when the sensory organs are stimulated. These potentials are considered as the reorganization of spontaneous brain oscillations in response to stimuli. SEPs manifest only in the presence of external stimuli and consistently occur at the same times and in the same modalities, earning them the term *phase-locked*. Among the SEPs, [56], Steady-State Visually Evoked Potentials (SSVEPs) have gained significant traction due to satisfactory signal-to-noise ratio (SNR) and information rate [57]. In the following Sections, more details about the SSVEP paradigm will be provided, along with the description of the proposed system.

2.2 The proposed system

This section describes the BCI system developed over the years. As aforementioned, brain signals can be captured following different strategies. Some examples are functional magnetic resonance imaging (fMRI) [58], magnetoencephalography (MEG) [59], near-infrared spectroscopy (NIRS) [60], and electroencephalography (EEG). Among these options, the BCI system taken into account in this study relies on EEG, since it is widely regarded as the optimal choice due to its non-invasiveness, user-friendliness, and cost-effectiveness [34].

2.2.1 SSVEP fundaments

The paradigm chosen to develop the EEG-based BCI is that based on the aforementioned Steady-State Visually Evoked Potentials (SSVEPs).

SSVEPs are dependent and exogenous brain potentials [61] that are evoked in the primary visual cortex when the user observes a flickering stimulus. The stimulation frequency bands of the visual stimuli typically range from 6 Hz to 30 Hz, with the highest Signal to Noise Ratio (SNR) observed in the range of 8 to 15 Hz [62]. The physiological SSVEP brain response typically occurs after a latency period ranging from 80 to 160 ms [63]. This response exhibits a sinusoidal-like waveform, consisting of a fundamental frequency matching that of the observed stimulus, along with frequently present higher harmonics [64], as illustrated in Fig. 2.3. Therefore, SSVEPs belong to the *Reactive* BCIs.

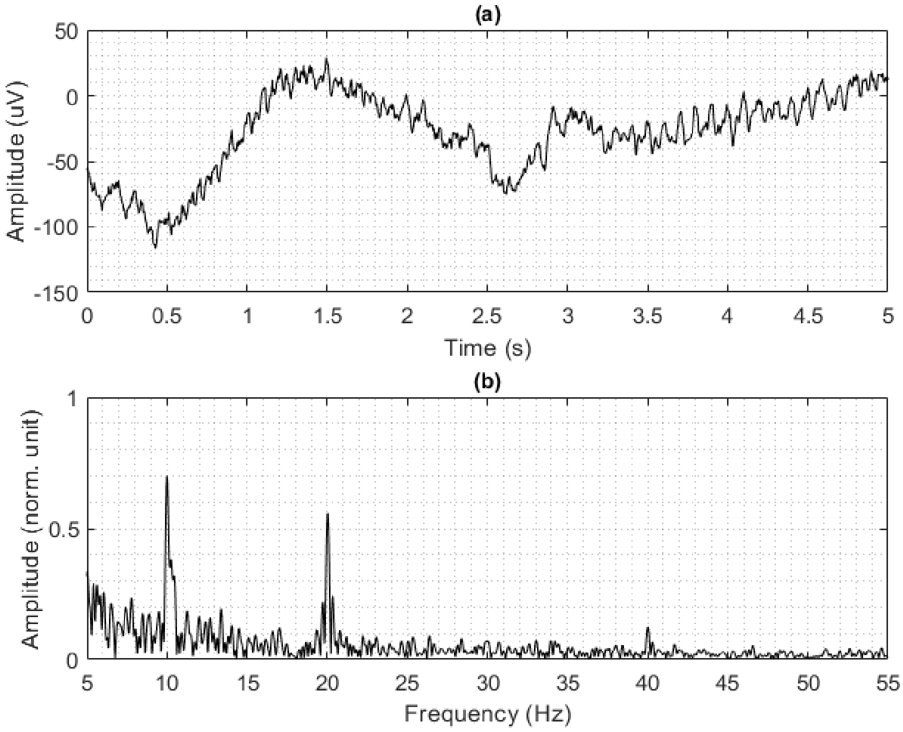

Fig. 2.3 A 10-Hz SSVEP in time domain (a) and frequency domain (b). Image taken from [3].

In practical applications, the user is presented with simultaneous stimuli at different frequencies. Each stimulus corresponds to a specific command, enabling the user to send the relevant command to the target application simply by looking at the desired flickering stimulus. Based on the generic BCI architecture shown in Fig. 2.1, a representative scheme of SSVEP-based BCIs can be represented as illustrated in Fig. 2.4. In addition to the already described *Signal Acquisition*, *Signal Processing*, and *BCI application* blocks, this architecture is composed of a *Stimuli Source* block,

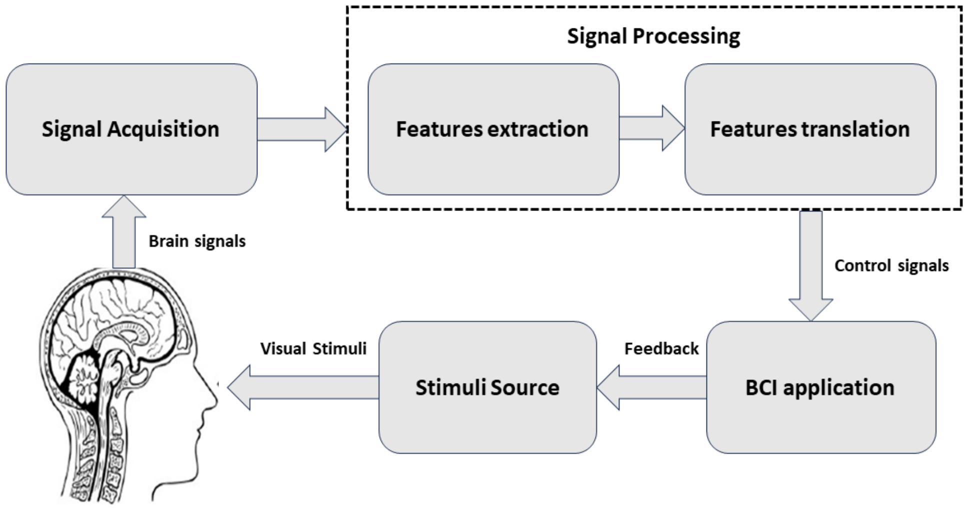

Fig. 2.4 Typical architecture of an SSVEP-based BCI

which is used to display *N* concurrent *Visual Stimuli*. Each stimulus flickers at a different frequency from the others and is associated to a specific command to send to the BCI application.

2.2.2 Design

Based on the generic architecture of SSVEP-based BCI illustrated in 2.4, this Section described the design of the AR-based SSVEP BCI taken into account in this work.

1. With regards to the *Stimuli Source*, an *AR HMD* is used to run a dedicated AR application that displays *N* concurrent *visual stimuli*. Each stimulus flickers at a different frequency from the others and is associated with a specific and known command to send.

2. The *Signal Acquisition* is performed by means of EEG: a portable *EEG headset* captures the user's brain signals and digitizes them.

3. According to [65], *"the Signal Processing block can be internal to the EEG headset, or external: in the latter case, it is typically a portable board connected to the EEG headset by cable [30], or a laptop that receives the EEG samples over wireless communication [66], or even the AR HMD itself [67]"*. The processing unit executes a dedicated classification Algorithm which is

in charge of processing the EEG sample and deducing which stimulus has been observed by the user: therefore, the recognition of N stimuli at different frequencies can be viewed as a N-class classification problem.

4. Once the classification has been made, a *Control signal* is sent to the *BCI application*, the last block of the system which provides a *Feedback* to the user depending on the selection performed. If the classification is successful, the output command will correspond to the choice desired by the user.

For the sake of comprehensiveness, Fig. 2.5 illustrates the system in detail.

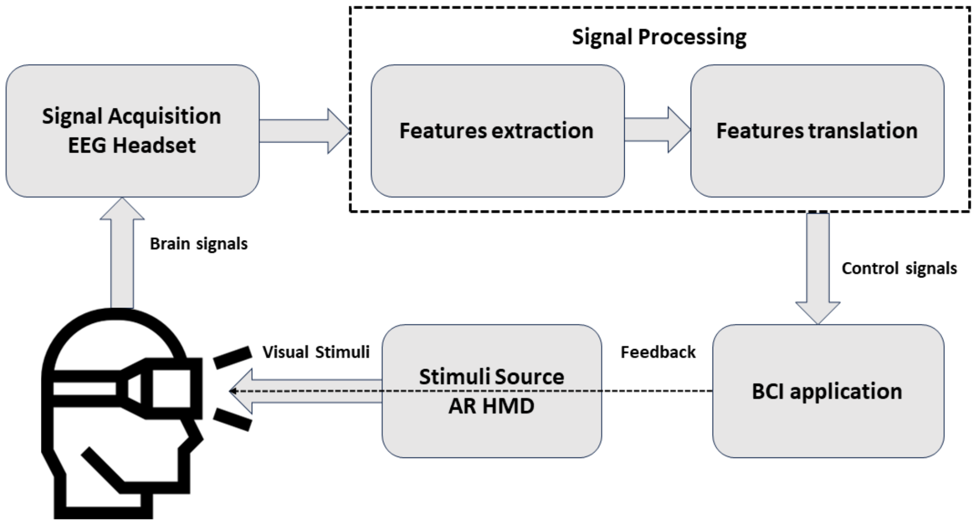

Fig. 2.5 Architecture of the AR-based SSVEP BCI taken into account.

The adoption of portable EEG Headsets for signal acquisition and, importantly, AR HMDs for stimuli rendering has been considered in recent years as a promising approach to enhance wearability, immersivity, and engagement in BCI applications' usage [68, 30, 69] compared to traditional methods. Traditionally, these stimuli are presented on a computer screen (CS), typically an LCD monitor positioned in front of the user. This setup allows visualization of up to 200 stimuli [70], making it valuable for applications like the *BCI Speller*, a system that enables severely motor-disabled patients to communicate using brain activity without muscular mobility [71, 72]. However, this configuration is bulky and restricts the portability of these systems, even though it delivers satisfactory performance. As a result, the adoption of BCI-SSVEP has been limited to laboratory environments for a long time [31]. In contrast, the innovative approach discussed here facilitates the deployment of SSVEP-based BCIs in diverse application contexts, ranging from healthcare [73–75] to industry [67, 76]. Nonetheless, the overall performance of such systems greatly depends on the specifications of the chosen HMD, which must be thoroughly analyzed [31, 76, 77]. To elaborate on this, there are several aspects to consider: first, the maximum number of flickering stimuli that can be displayed depends on the HMD's field of view (FOV), typically ranging from a minimum of two [30] up to nine [78]. Nevertheless, there is ample room for improvement to achieve a number of stimuli comparable to LCD-based visualization; secondly, HMDs' hardware is generally less powerful than desktop PCs, leading to significant unpredictability of the frame rate (fps) when displaying flickering stimuli [79]. This variation affects the values of the rendered stimulation frequencies, potentially reducing the classification performance of the SSVEPs [25]; finally, the stimuli rendered by AR HMDs are *holographic*, superimposed on the real space with an assigned level of transparency. Consequently, an increase in environmental brightness weakens the SSVEPs' intensity, resulting in lower recognition [77]. Ensuring appropriate classification performance, becomes a crucial aspect for AR-based SSVEP BCIs.

Overall, the adoption of AR HMDs offers exciting possibilities for SSVEP-based BCIs in various applications, but the specific characteristics of the chosen HMD play a critical role in determining the system's performance. These issues have been accurately addressed, as described in the following Section.

2.2.3 Realization

This Section provides a description of the hardware and software systems adopted over the years to develop the designed AR-based SSVEP BCI. By referring to the functional blocks shown in Fig. 2.5, three main aspect were considered, namely the selection of the *AR HMDs*, *EEG Headset*, and *Processing Strategy* to employ.

AR HMDs

The first AR device used (please refer to [30]) was *Epson Moverio BT-200*, a pair of AR smart glasses [80]. The perceived screen size of the glasses is 2 m at a 5 m projected distance, with a refresh rate of 60 Hz and a 23° diagonal FOV. The developed AR environment consisted of two squares, flickering at 10 Hz and 12 Hz, placed at the right and left ends of the screen, respectively, and generated with the Android library OpenGL. The stimulation was realized by means of a *black/white* alternation over time, according to the guidelines described by [62].

Successively, in [31, 4], the system was enhanced by means of the employment of *Microsoft Hololens 1*, [81] which is an Optical-See-Through (OST) AR HMD endowed with a 60 Hz Refresh Rate and a diagonal FOV of 34°. The improved diagonal FOV allowed to accommodate up to four squares flickering in the range 8-15 Hz, and placed at the four edges of the screen. The AR environment was realized by means of the software *Unity* and the *Windows Mixed Reality Toolkit (MRTK)*. Again, the stimulation was realized by means of *black/white* alternation over time.

Current developments in the realization of AR HMDs are paving the way for further enhancements. As a matter of fact, the upgraded version of Hololens 1, namely *Microsoft Hololens 2* [82], which is endowed with a diagonal FOV of 52°, is currently being adopted since it allows the accommodation of six flickering stimuli (always selected in the range 8-15 Hz). As for its previous model, the AR environment was realized by means of the software Unity and MRTK libraries. In addition, the stimulation is exploiting a *grayscale* [83] alternation between black and white colors, as it guarantees both less visual fatigue in users and an increase in the recognition of the observed stimuli with respect to traditional stimulations.

For the sake of clarity, Fig. 2.6 illustrates the AR devices along with a representation of the user's point of view. As visible, the restricted FOV of Epson Moverio does not allow the accommodation of more than two flickering stimuli. On the other hand, the adoption of Microsoft Hololens 1 and 2 allows for leveraging a wider area for rendering the stimuli.

EEG Headset

In [30, 31, 4], the device used to acquire EEG signals from users scalps was the *Olimex EEG SMT* [84]. It is a 10-bit, 256 S/s, differential input Analog-Digital Converter (ADC). Brain signals were captured using (i) two active electrodes positioned at the Frontal Midline (Fpz), connected to the negative input, and Occipital Midline (Oz) positions, connected to the positive, according to the international system 10-20 [67], and (ii) a passive electrode (acting as reference) Driven Right

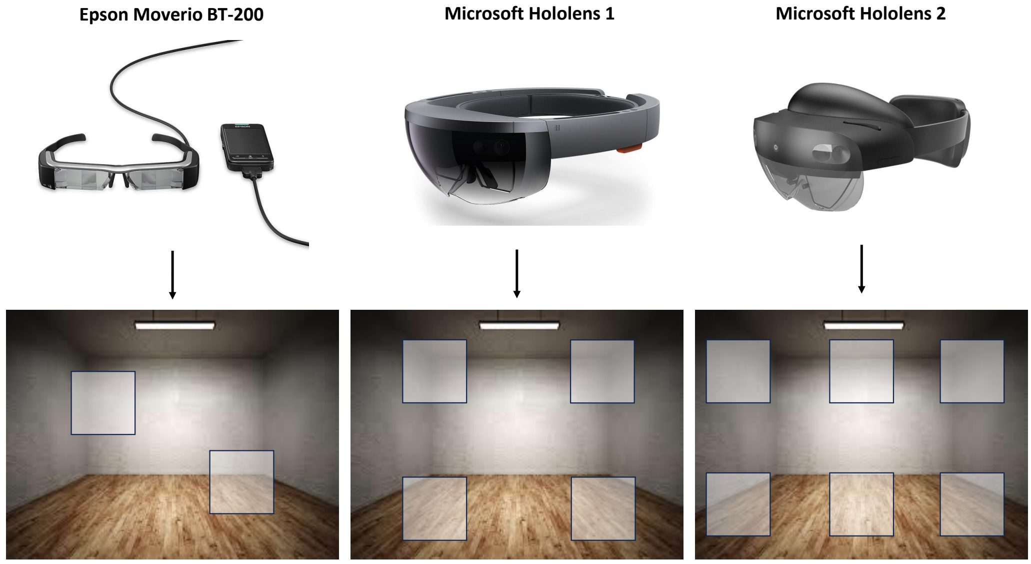

Fig. 2.6 AR devices used for SSVEP elicitation, along with an illustrative sketch of the flickering stimuli accommodation.

Leg (DRL), positioned on the earlobe. The Fpz and DRL electrodes contacts consist of gold-plated, flat surfaces, while the Oz electrode was modified by adding eight gold-plated spring connectors to improve the skin contact through the hair.
The configuration described is single-channel and based on *dry* electrodes. In a nutshell, dry electrodes have been proposed as a potential solution to the inconvenience caused by *wet* electrodes, which are considered the gold standard for clinical recordings [85]. Dry electrodes are typically designed with reusable materials, eliminating the need for conductive gels or paste. They can be easily placed on the scalp through the hair, reducing the setup time [73, 66]. However, it's important to point out that the contact impedance between dry electrodes and the users' scalp is hugely influenced by the pressure applied, unlike wet electrodes [86]. This factor may contribute to a sense of discomfort or pain experienced by users. Most importantly, the SNR achieved by the employment of wet electrodes is still significantly better than that achieved by dry alternatives.

Based on these considerations an enhancement of the system is being developed in order to increase the amount of information to acquire. This enhancement consists of the employment of a wireless, wet EEG Headset, namely *Flex EEG* by *Neuroconcise* [87], along with five acquisition channels, corresponding to the position *Oz, O1, P3, P7* and *Pz*, according to the 10-20 International System. The chosen sampling rate is 125 Sa/s, while the communication with external processing units is made by means of Bluetooth 2.0 protocol.

Fig. 2.7 EEG devices used over the years.

Processing Strategies

Regarding the processing strategies, *Power Spectral Density Analysis (PSDA)* is acknowledged as the most intuitive approach to detect and classify SSVEPs [62]. The initial step involves applying Fast Fourier Transform (FFT) to the user's EEG. Subsequently, Power Spectral Density (PSD) is evaluated around each of the N rendered frequencies. Additionally, N_h multiple harmonics can be taken into account, as expressed by:

$$P(f_n) = \frac{1}{2N_hk+1}\left[\sum_{i=1}^{N_h}\sum_{j=ik_n-k}^{ik_n+k} w(i)\, A^2(j)\right] \tag{2.1}$$

where: $P(f_n)$ is the PSD coefficient for the given frequency f_n $(n = 1,2,...,N)$, k_n is the corresponding bin in the frequency domain, k is the number of nearest bins considered, i is the harmonics index, A is the signal amplitude, and w is a weight assigned to each harmonics. The classification is typically based on the assumption that the observed stimulus is likely the one with the highest PSD [88]. The main drawback of PSDA is the need for a minimum time window T_{min} for the acquired EEG to correctly discriminate two sinusoidal tones, as an appropriate frequency resolution $\Delta f = \frac{1}{T_{min}}$ is required [89].

Canonical Correlation Analysis (CCA) serves as an alternative, time domain-based method for SSVEP classification. It is a multivariate statistical approach that correlates linear relationships between two sets of data [90]. CCA is performed between the EEG signal X and a set of sine waves Y_n corresponding to the frequencies of the N stimuli displayed, along with their multiple harmonics. The set of sine waves $Y_n(t)$ $(n = 1,2,...,N)$ can be obtained following (2.2).

$$Y_n = \begin{bmatrix} sin(2\pi\, f_n\, t) \\ cos(2\pi\, f_n\, t) \\ sin(2\pi\, 2f_n\, t) \\ cos(2\pi\, 2f_n\, t) \\ \dots \\ sin(2\pi\, N_h f_n\, t) \\ cos(2\pi\, N_h f_n\, t) \end{bmatrix} \tag{2.2}$$

For each stimulation frequency f_n, a correlation coefficient ρ_n is obtained through CCA between X and Y_n. These coefficients are utilized for the classification stage. For instance, in [90], the output of the classification was associated with the frequency having the highest correlation coefficient. In contrast, in [30, 31, 91], the maximum value among the correlation coefficients ρ_n was compared with two thresholds, and the signal was classified only if the chosen correlation coefficient exceeded the thresholds. CCA typically achieves better classification performance compared to PSDA [88]. However, bandpass filtering of the EEG signal may be required due to the impact of spontaneous EEG activities not related to SSVEP events, such as eye-blinking. Another drawback is that this method is not robust against undesired variations in the generated frequencies caused by drops in fps of the AR headset, unlike PSDA.

In order to leverage the benefits of both PSDA and CCA, a hybrid method was proposed in [4], called *Features Extraction* (FE), which consists of two steps:
First, the brain signal X is processed in both the frequency and time domains in order to extract a reduced set of features. Specifically, (i) a Fast Fourier Transform (FFT) is applied to X; then, (ii) SSVEP peaks are recognized around all the N rendered stimulus frequencies. For each nominal frequency value f_n with $(n = 1,2,...,N)$, the interval $[f_n \cdot 0.9, f_n \cdot 1.1]$ is considered to find the actual peak frequency f_p. Detecting the actual peaks leads to more accurate PSD coefficients P_n. Additionally, (iii) in the time domain, Canonical Correlation Analysis (CCA) is performed between X and a set of sinewaves Y_n, having the frequencies of the N detected peaks, further

enhancing the accuracy of the CCA coefficients ρ_n. Ultimately, only $2N$ features are extracted and normalized from a given brain signal composed of $fs \cdot T$ EEG samples and N stimulation frequencies, where f_s is the sampling frequency, and T is time in seconds.

The second step involves classification, carried out using the three ML classifiers mentioned earlier: SVM, k-Nearest Neighbor k-NN, and ANN. The conducted experimental campaigns allowed obtaining a significant increase in classification performance compared both to traditional CCA-based algorithms and PSDA, primarily due to the mitigation of fps variations. Fig. 2.8 provides an illustration of the proposed algorithm.

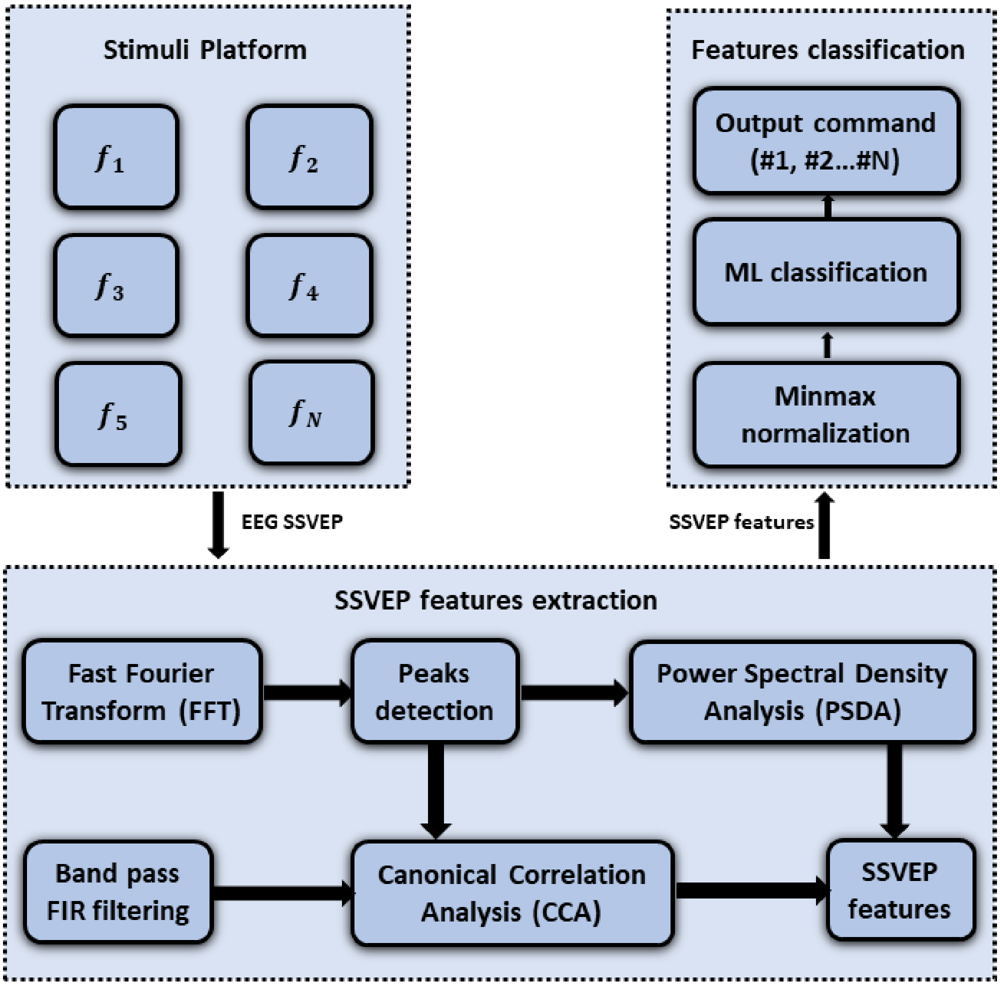

Fig. 2.8 Details of the algorithm developed in [4]

2.2.4 Performance evaluation

This section provides further details about the typical metrics used to evaluate the performance of BCI-SSVEP systems. These metrics are applied with a metrological approach to various systems developed over the years, which are described in the following paragraphs. This comparison aims to offer insights into the best implementation strategies that enable the widespread use of these systems by a broad range of users.

Metrics

The most important metrics related to an N-stimuli, SSVEP-based BCI are three, namely *Time Duration*, *Accuracy*, and, most importantly, *Information Transfer Rate (ITR)*.

1. The Time Duration is defined as the duration of brain signals to be classified and translated into a command.

2. The Accuracy is defined as the percentage of brain signals correctly classified.

3. The ITR represents a comprehensive performance indicator that quantifies the amount of information conveyed to the selected BCI application. It is defined as follows:

$$ITR = \left[log_2(N) + A\ log_2(A) + (1-A)\ log_2\left(\frac{1-A}{N-1}\right)\right]\frac{60}{T} \tag{2.3}$$

   where N is the number of flickering stimuli, A is the classification accuracy within the interval $[0,1]$, and T is the time duration (expressed in seconds) of the processed EEG signals. The ITR is expressed in *bit/min* and considers the trade-off between accuracy, number of stimuli, and the temporal duration of the acquired EEG. As a result, it emerges as a more reliable metric compared to classification accuracy alone. While classification accuracy might appear considerably high when reducing the number of stimuli and prolonging acquisition times, ITR accounts for these factors and provides a more meaningful measure of performance. Hence, it is essential to highlight that achieving a high classification accuracy alone does not guarantee the development of a high-performing BCI. Optimal performance requires not only high accuracy but also minimized acquisition times and a substantial number of stimuli to maximize the ITR and effectively convey information to the BCI application.

Since EEG signals are characterized by significant inter-individual variability, a suitable procedure to evaluate the performance of an SSVEP BCI system by means of the metrics introduced should be based, first, on the realization of a dataset containing L signals acquired for M subjects, each with a fixed time duration T and labeled with an observed frequency f_n (where $n = 1, 2, ..., N$). Therefore, given the processing strategy to apply, a Leave-One-Subject-Out Cross-Validation (LOSO CV) should be applied to evaluate the classification accuracy across the subjects.
LOSO CV is a variant of the K-fold cross-validation. Given M of subjects, LOSO CV procedure divides the entire dataset in M folds, where each fold is constituted by a specific subject. Therefore, for each combination of the parameters of the algorithm, the process will run M times, each time with a different subject in the test set, taking the remaining $(M-1)$ in the validation and training sets (if applicable). Therefore, at the end of LOSO CV, an inter-individual mean value A_m and a standard deviation σ_A of the classification accuracy are obtained as indexes of the generalization capability of the developed system as a whole. Moreover, by dividing the standard deviation for the number of subjects, the inter-individual standard uncertainty of the classification accuracy u_A is obtained. According to the *Guide to the Expression of Uncertainty in Measurements (GUM)* [92], the output probability distribution is a t-student distribution with a number of degrees of freedom ν_A = M - 1. Hence, a suitable coverage factor k can be used to provide an extended uncertainty $U_A = k\ u_A$ and, therefore, a confidence interval, and the measurement results can be expressed as $(A_m \pm U_A)$ %.
Once the measurement result of the classification accuracy is obtained, the best estimate of the ITR can be provided by means of (2.3), when the best estimate A_m is used as classification accuracy value. With regards to the uncertainty of the ITR, it can be evaluated by means of the first-order *Law of Propagation of Uncertainty*, expressed in (2.4).

$$u_{ITR} = \sqrt{\left(\frac{\partial ITR}{\partial A} \cdot u_A\right)^2} \tag{2.4}$$

The extended uncertainty $U_{ITR} = k\ u_{ITR}$ is obtained by considering a t-student distribution with a number of degrees of freedom ν_{ITR} assessed according to the Welch-Satterthwaite equation [92].

However, this traditional approach might not be suitable for these measurands, especially given that classification accuracy is defined in the interval $[0 \div 100]\%$. In this case, the assumption of probability distributions like Gaussian or t-student could lead to measurement results that are outside of the allowed range. To address this, different probability distributions, such as truncated-Gaussian, should be considered. In this context, Supplement 1 to the GUM suggests adopting the Monte Carlo Method [93]. In summary, this method involves estimating the probability density function (pdf) of the classification accuracy and then generating a vector of i elements (e.g., 10^6 samples) from that distribution. Subsequently, the desired confidence interval (e.g., 99 %) can be extracted from the resulting samples. Similarly, for the ITR, the accuracy vector can be propagated using (2.3), resulting in a vector of extractions of ITR. Once again, the desired confidence interval can be obtained from the resulting extractions. By employing the Monte Carlo Method and considering the appropriate probability distributions, the evaluation of these performance metrics becomes more robust and accurate.

Description of the Systems

Among the various systems developed over the years, three of them stand out as particularly noteworthy and merit description and comparison.

1. The first system, utilized in [30, 73], employed the Moverio BT-200 as the AR device, capable of rendering two flickering stimuli at frequencies of 10 Hz and 12 Hz. Brain signals were captured using dry electrodes and Olimex EEG SMT. The system utilized a single-channel configuration, specifically targeting the Oz location based on the 10-20 International System. To recognize SSVEPs, Canonical Correlation Analysis (CCA) was adopted as the classification approach.

2. The second system was utilized in [31, 4] and employed Microsoft Hololens 1 to render four flickering stimuli (at 8.57 Hz, 10.00 Hz, 12.00 Hz, and 15.00 Hz). Again, brain signals were captured using dry electrodes and Olimex EEG SMT, in the same single-channel configuration as system #1. Instead, to recognize SSVEPs the Feature Extraction (FE) hybrid method was adopted.

3. Currently, the system employed relies on Microsoft Hololens 2 to render six flickering stimuli (at 8 Hz, 9 Hz, 10 Hz, 11 Hz, 12 Hz, and 13 Hz) in grayscale

mode. Brain signals are captured by means of Flex EEG and wet electrodes. Five channels are exploited, namely Oz, O1, Pz, P3, and P7. FE method is used to classify SSVEPs.

For better clarity, Fig. 2.9 illustrates the three systems taken into account.

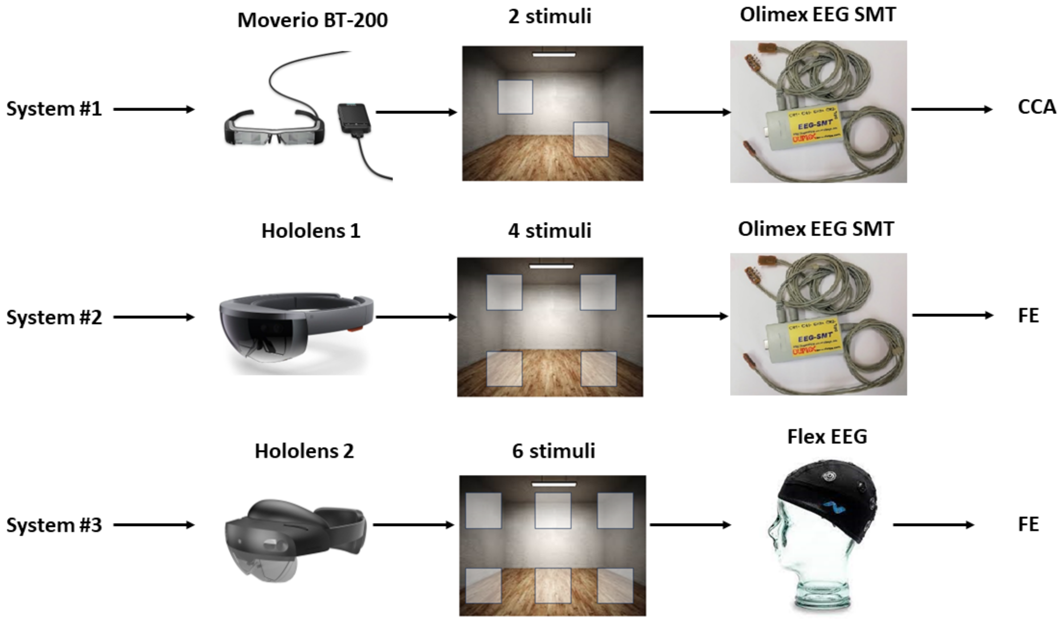

Fig. 2.9 Representation of the three considered AR-based SSVEP BCIs.

Results

This paragraph reports the experimental results obtained from the evaluation of the performance of the three aforementioned systems.

Regarding the first system, an experimental campaign was conducted involving twenty healthy and untrained subjects with normal or corrected-to-normal vision, aged between 20 and 40 years. For each subject, a total of 24 signals were acquired, with twelve signals labeled as 10 Hz and the remaining twelve signals labeled as 12 Hz. The results in terms of accuracy and ITR are presented in Table 2.1, indicating various time durations considered. It is important to note that the Monte Carlo Method, as previously described, was applied using 10^6 extractions and a 99 % confidence interval.

Time Duration (s)	Accuracy (%)	ITR (bit/min)
0.5	65.0÷76.5	7.5÷25.2
1.0	64.4÷85.1	3.1÷22.6
2.0	77.9÷91.8	6.9÷17.5

Table 2.1 Performance of the system #1. A 99 % confidence interval is considered.

To validate the second system, an experimental campaign was carried out with nine healthy and untrained subjects who met the inclusion criteria of normal or corrected-to-normal vision and age between 20 and 40 years. For each subject, a total of twenty signals were acquired, with five signals corresponding to each stimulation frequency. The results of this experimental campaign in terms of accuracy and ITR are presented in Table 2.2, showcasing various time durations considered. As before, the Monte Carlo Method was applied, utilizing 10^6 extractions and a 99 % confidence interval.

Time Duration (s)	Accuracy (%)	ITR (bit/min)
0.5	36.3÷53.5	4.9÷31.1
1.0	52.4÷81.1	13.9÷58.7
2.0	61.9÷90.9	12.4÷41.5

Table 2.2 Performance of the system #2. A 99 % confidence interval is considered.

Regarding the third system, it is currently in the validation phase. As of now, data were acquired only from four subjects, with five signals obtained for each of the six flickering stimuli. The preliminary results are presented in Table 2.3.

Time Duration (s)	Accuracy (%)	ITR (bit/min)
0.5	40.2÷59.0	26.3÷77.9
1.0	65.4÷87.0	50.4÷102.7
2.0	78.4÷99.2	38.9÷73.6

Table 2.3 Performance of the system #3. A 99 % confidence interval is considered.

Indeed, the improvements brought about by the adoption of wet electrodes and a more immersive AR device are evident and noteworthy. As can be observed, the Information Transfer Rate (ITR) significantly increases from a maximum of 25 bit/min in the first system to a remarkable maximum of about 100 bit/min in the third system. This substantial increase in ITR underscores the impact of employing wet electrodes and a more advanced AR device, which results in improved signal quality and enhanced user experience. These enhancements play a crucial role in achieving higher accuracy and faster information transfer in the BCI systems, making them more efficient and effective for practical applications. The promising results demonstrated by the third system suggest its potential for real-world implementation and open new possibilities for future developments in SSVEP-based BCIs.

2.3 Application fields

This Section described the application fields in which the developed systems have been employed over the years by our research group. More in detail, two relevant frameworks will be described, namely the data selection in the operating room, and the rehabilitation for children with attention disorder.

2.3.1 Data selection in operating room

In [25, 74], an integrated real-time monitoring system based on Augmented Reality (AR) and SSVEP Brain-Computer Interfaces (BCIs) was proposed for hands-free acquisition and visualization of remote data. The focus of the study was on monitoring patients' vital signs in the operating room (OR) setting. By employing the combined capabilities of an SSVEP BCI and AR device, an anesthetist could effectively monitor the patient's vitals in real-time, using data acquired from the electromedical equipment. Given the critical nature of healthcare-related applications and their stringent real-time requirements, the scenario chosen for this study presented an interesting and challenging testbed for the proposed system. Experimental tests were conducted at the University Hospital Federico II in Naples, Italy, using standard equipment commonly found in ORs. The system underwent preliminary functional validation, and accuracy and delay metrics were measured to assess its performance. In particular, the on-field performance of the single-channel SSVEP-based BCI showed an accuracy of 70% with a latency of approximately 4.00 s. The experimental results demonstrated the effectiveness and reliability of the proposed AR-BCI-based monitoring system. By providing real-time access to vital data through AR glasses, the system offered a hands-free and intuitive approach for healthcare professionals to monitor patients during medical procedures. This innovative application of AR and SSVEP BCIs holds significant potential for improving healthcare monitoring in critical settings and may lead to further advancements in the field of medical technology.

Fig. 2.10 and 2.11 show the user view before and after making the selection of the waveform to display in real time.

Fig. 2.10 Waveform selection menu.

Fig. 2.11 User view after performing the selection.

2.3.2 Rehabilitation for children with attention disorder

In [30, 73, 75, 94], an instrument for remote control of robot by wearable Brain-Computer Interface was proposed for rehabilitating children with attention disorders. Augmented Reality (AR) glasses generated flickering stimuli and a single-channel electroencephalographic BCI detected the elicited Steady State Visual Evoked Potentials (SSVEP). This allowed to benefit from the SSVEP robustness by leaving available the view of robot movements. Together with the lack of training, a single channel maximizes the device's wearability, fundamental for the acceptance by children, while effectively controlling the movements of a robot through a new channel enhances rehabilitation engagement and effectiveness. Through a case study at an accredited rehabilitation center (*Villa Delle Ginestre, Volla, Naples, Italy*), a preliminary evaluation of the children adherence to the therapy was conducted on 18 subjects, and a two-months therapy was conducted on 7 participants. During this period, different tasks were assigned to the children depending on their level of involvement. The experimental results, based on the Italian Battery for ADHD (BIA) showed encouraging results, where all the participants observed an improvement in the various test proposed, even with a low number of session.

Fig. 2.12 shows the user's view while wearing the AR device and looking at the robot.

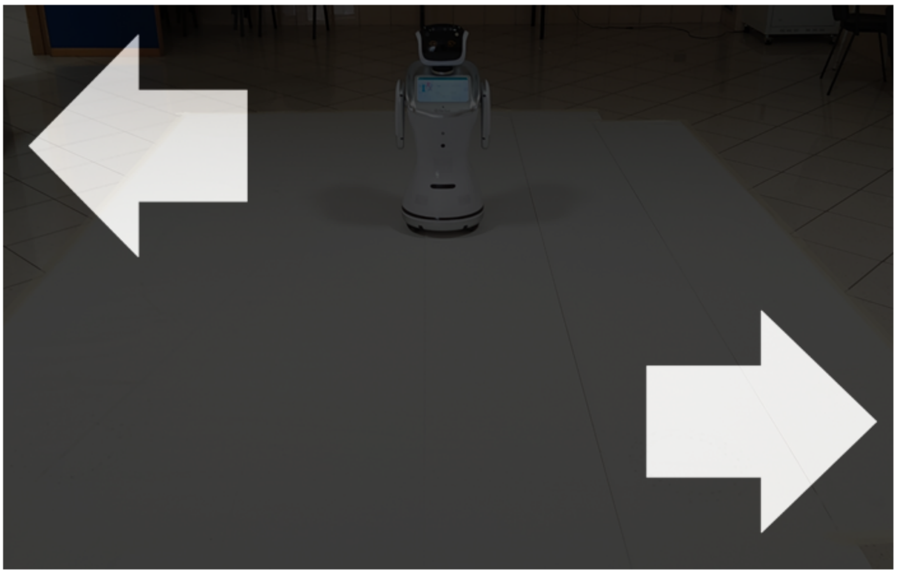

Fig. 2.12 User's view while wearing the system.

2.4 Conclusions

In this Chapter, the design and development of Brain-Computer Interfaces relying on Visually Evoked Potentials and Augmented Reality technology were described. After a comprehensive resume of the notions necessary to build an SSVEP-based BCI, different systems designed and developed over the years were shown and thoroughly compared in order to highlight the contributions in enhancing the accuracy of the systems in light of adoptions in real-life scenarios. In particular, a metrological approach was adopted in order to evaluate the system performance across different subjects. Finally, two relevant case studies, regarding the on-field employment of the proposed system (i) during surgical procedure and (ii) in the framework of children rehabilitation, are shown.
Overall, the achieved results in terms of SSVEP recognition accuracy, amount of transmitted information, and ergonomics can be considered promising for future applications of this technology in real-world settings outside of laboratory setups.

Chapter 3

Augmented Reality Platforms to Monitor Patients' Health in Operating Room

This chapter presents the development of an Augmented Reality (AR) platform designed to enable the monitoring of a patient's health in real-time during surgical procedures in the Operating Room (OR). The system, as described in [5, 25, 24], provides the surgical team with immediate access to a comprehensive set of patient information. The AR platform automatically captures the patient's vital signs coming from the OR instrumentation and displays them, in real-time, directly on an AR headset. Additionally, clinical records can be accessed on request. Furthermore, the AR-based monitoring platform allows for the display of video streaming coming from the endoscope in AR, providing an innovative aspect of the proposed platform. The system's innovation is demonstrated in its comprehensiveness of available information, modular and flexible adaptation to different data sources, ease of use, and reliable communication - all critical requirements for the healthcare field. Experimental tests were conducted at the University Hospital *Federico II* (Naples, Italy) to validate the system by means of a metrological approach, using commonly available OR instrumentation such as an endoscope, a patient monitor for intensive care, and a respiratory ventilator. Results showed over 99 % communication accuracy of data, with an average time response below the millisecond, along with satisfactory feedback from the System Usability Scale (SUS) questionnaires that were filled out by physicians after intensive use.

3.1 Rationale

As previously stated, the Fourth Industrial Revolution has yielded numerous benefits across various application domains, healthcare included. With regard to AR, it has shown relevant applications in healthcare, particularly in medical training and surgical procedures. Alamri et al. [95] and Fida et al. [96], Meola et al. [97], Badiali et al. [98], Condino et al. [99], Checcucci et al. [100], and Roberts et al. [101] have all demonstrated the potential of AR in medical training and surgical procedures. One of the most important applications of AR in surgery is represented by the overlay of medical images on patients during surgical procedures, as described in [102]. Additionally, Condino et al. [103] presented a patient-specific hybrid simulator for orthopedic open surgery, with a focus on the realization of wearable AR functionalities using Microsoft HoloLens. This device is a successful commercial Optical See-Through Head-Mounted Display (OST-HMD) that provides advantages in contrast perception and computational effort [104]. More recently, Tu et al. [104] used the upgraded version of this device, the Microsoft HoloLens 2, aiming to assist surgeons in completing distal interlocking. This approach offers benefits such as no radiation exposure, stereoscopic in-situ visualizations, and less time consumption when compared to conventional approaches.

Another significant application of AR is the real-time monitoring of patients' health during surgical procedures in the operating room (OR). By displaying patients' vital signs and relevant information from electronic clinical medical records, directly on an AR headset worn by the surgical team, AR technology facilitates effective real-time monitoring of patients' health status, even if at a distance from the medical equipment. The aim of this technology is to improve the efficiency of surgical procedures by reducing the burden of continuously looking at the OR equipment. By using AR technology, the surgical team can focus its attention on the patient and the task at hand, being prepared to promptly respond in case of any aggravating conditions [105–109]. For instance, in [105], the frequency with which anesthetists had to divert their attention from the patient to the equipment was investigated, and a significant reduction of more than a third was observed when using an AR HMD.

Despite the significant potential of AR-based real-time monitoring systems for patients undergoing surgical procedures, as reported in [5], *"only the usability of such systems has been explored, without an assessment of their performance"*. This gap in the research was highlighted in [110], where a systematic review of ten years of AR usability studies revealed that, with regards to health infrastructure, most medical-related AR papers have been published in medical journals and that there is a scarcity of qualitative data captured from users concerning their mental and/or physical status after using the system. In more recent work, [111] investigated the usability and ergonomics of Microsoft Hololens and Meta 2 AR devices for use in visceral surgery using the System Usability Scale (SUS) questionnaire [112], a method that has been successfully employed for assessing AR-based applications in Education [113] and Industry 4.0 [114]. However, while usability assessments are important, there is also a pressing need for performance assessments of real-time monitoring systems for patients undergoing surgical procedures. Ensuring the accurate and timely transmission of information to be displayed in AR is critical. For instance, in [115, 116], the key requirements for real-time, wireless data transmission were explored, including the bandwidth, the amount of interruptions per time unit, the mean duration of stops, the delay in monitoring, the energy efficiency, and the reliability. It was found that any audio or video delay higher than 300 ms should be avoided to ensure proper interactions between users and system. Moreover, techniques of fault tolerance are generally included in the network to prevent failures that can range from small outages to even large life-threatening scenarios.

Based on these considerations, the development of an integrated monitoring platform that incorporates AR to aid medical personnel during surgical procedures has been proposed. The system provides several features that can be selected by the intended user to assist surgeons, assistant surgeons, nurses, and anesthetists in real-time monitoring of the patient's health status. The Microsoft Hololens 2 AR headset has been chosen to receive data from the electromedical instruments available in the OR, such as the respiratory ventilator, patient monitor, and laparoscopic camera, and display them in real-time [117]. The platform also provides access to patient electronic clinical records and allows rendering of video streaming from the laparoscopic camera upon request. Notably, the proposed monitoring platform is innovative due to its comprehensive information, modular and flexible design, ease of use, and reliable communication, which are critical requirements for the healthcare field. Despite the high cost of the Microsoft Hololens 2 (approximately 3500 $), its unique features make it currently the most suitable device to satisfy the healthcare requirements. Furthermore, the system's performance is meticulously assessed not only in terms of data transmission and overall usability using the System Usability Scale (SUS) questionnaire but also through rigorous metrological methodologies.

The integration of metrology in the design and validation phases is particularly crucial for medical applications, where precision and accuracy are paramount [24].

3.2 Design

This section focuses on the design of the proposed AR-based monitoring platform. Special attention was given to the conceptual design of the integrated system to ensure modularity and flexibility, enabling the connection of various medical equipment and the integration of data from diverse sources. The platform's design aims to assist nurses, anesthetists, and/or surgeons in monitoring the patients' health status simply by wearing an AR headset. This approach eliminates the need to rely on separate monitoring equipment, allowing them to respond promptly in case of worsening patient conditions. Figure 3.1 illustrates the distinct components of the integrated AR monitoring platform. Essentially, a group of *Medical Instruments* is

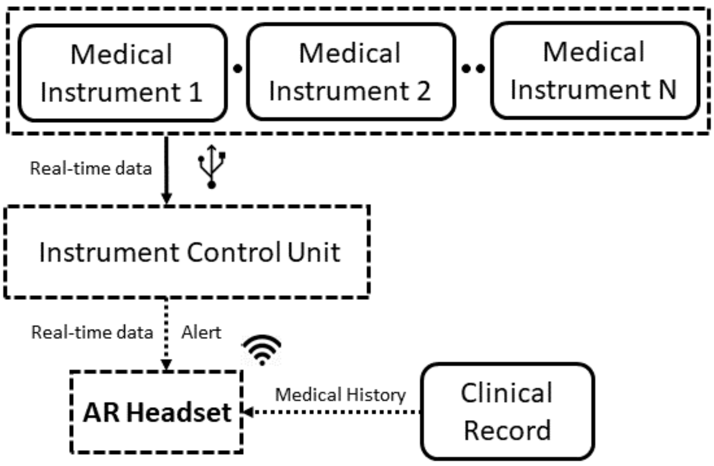

Fig. 3.1 Conceptual architecture of the proposed AR-based monitoring platform. Image taken from [5].

connected to an *Instrument Control Unit (ICU)* through cables. The ICU transmits real-time data to the *AR Headset* worn by the user. Simultaneously, the ICU also generates alerts if the acquired parameters, such as the patient's vitals, surpass standard values. Furthermore, the AR Headset receives the selected patient's Clinical Record, providing a comprehensive set of health information upon request. The design decisions were made with careful consideration of the healthcare sector's strict requirements, particularly regarding the communication latency between data generation and visualization of patient information.

3.3 Realization

This Section addresses the implementation of the designed system. In particular, a description of the selected hardware and the implemented software is provided below.

3.3.1 Hardware

In Figure 3.2, the block diagram illustrates the hardware components and communication modalities employed to implement the proposed monitoring platform. For the case study, the medical equipment typically found in an operating room is considered. This includes: (i) a pulmonary ventilator, (ii) a patient monitor, and (iii) an endoscope for laparoscopic surgery. To implement the platform, a Laptop functions as the Instrument Control Unit (ICU). It acquires real-time data from the medical equipment mentioned above. Subsequently, the Laptop transmits the acquired data to the Augmented Reality (AR) Headset. The AR Headset receives the patient's information from the electronic clinical record. This comprehensive data integration allows for a detailed understanding of the patient's health status. For a more detailed explanation, please refer to the following description.

Operating Room Equipment

The equipment utilized in this work within the operating room consists of three components: (i) a pulmonary ventilator, (ii) a patient monitor, and (iii) an endoscope (see Fig. 3.3).

- *Pulmonary ventilator*: The ventilator employed in this work is the Dräger Infinity V500. This particular ventilator is designed for intensive care and plays a crucial role in assisting patients by providing an appropriate level of oxygen (O_2) while eliminating carbon dioxide (CO_2) from their lungs. It also helps reduce the respiratory effort for patients experiencing excessive lung

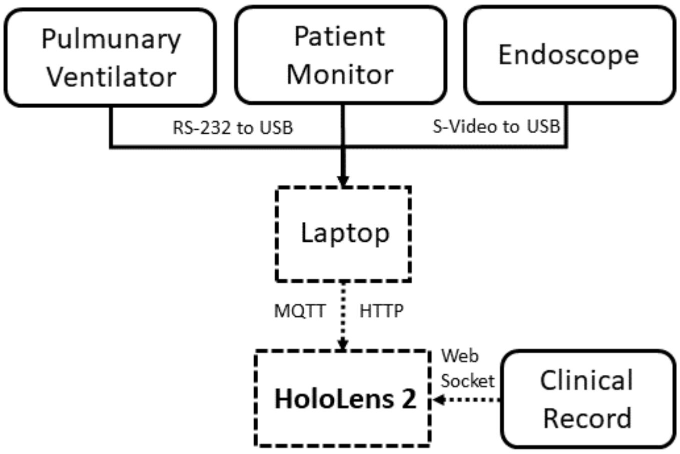

Fig. 3.2 Implementation of the proposed AR-based monitoring platform. Image taken from [5].

workload. The Dräger Infinity V500 ventilator is equipped with a LAN (Local Area Network) interface and three RS-232 interfaces. The user has the option to select between the MEDIBUS or MEDIBUSX protocol for communication. Additionally, the user can configure parameters such as Baud Rate, Parity Bits, Stop Bits, and Terminator Character according to their requirements.

- *Patient monitor*: The patient monitor chosen for this project is the Philips IntelliVue MP90. This advanced monitor enables the monitoring of over 50 different vital signs. By connecting separate "plug-and-play" modules, the monitor can track various parameters such as oxygen saturation, compound ECG, respiration rate, and heart rate, among others. Its versatility and comprehensive monitoring capabilities make it a valuable tool in healthcare settings.
- *Endoscope*: The endoscope utilized in this project is the Olympus Visera Elite II. This advanced imaging platform is designed for various surgical procedures, including general surgery, urology, gynecology, and more. The endoscope features an S-video interface, which grants access to the camera, allowing for high-quality imaging during procedures. Its capabilities make it a versatile tool in visualizing and documenting surgical interventions.

Fig. 3.3 Electromedical devices used: pulmonary ventilator (left); patient monitor (center); endoscope (right). Image taken from [5].

AR Headset

The AR headset utilized is the Microsoft HoloLens 2. This device runs on Windows 10 Holographic and offers a range of features suitable for augmented reality experiences. The HoloLens 2 is equipped with four light cameras, two infrared cameras, a depth sensor, an Inertial Measurement Unit (IMU), and an 8 MP camera. Users can interact with the device using various methods, including hand gestures, eye tracking, head tracking, and voice commands. These interaction modes enhance the user experience and enable seamless navigation within the augmented reality environment. Compared to its predecessor, the HoloLens 2 boasts several significant improvements. One notable enhancement is the increased diagonal field of view (FOV), now reaching up to 52 degrees. Additionally, the display resolution has been improved to 2048 x 1080 pixels. Although the HoloLens 2 comes with a relatively higher cost, its advanced hardware and intuitive interaction modes make it an optimal solution for meeting the stringent requirements of the healthcare sector, particularly in terms of communication latency and usability.

Laptop

The operating room equipment used did not impose strict requirements for communication protocols with the Instrument Control Unit. Therefore, a laptop with the following specifications was selected: Intel i7-10750H processor, 16 GB RAM, Windows 10 operating system, and three USB 3.1 ports. To establish a connection with the pulmonary ventilator, an RS-232 to USB adapter is employed. For the patient monitor, two adapters are used. First, a Medicollector adapter, which is a specialized LAN to RS-232 adapter, is utilized. Additionally, a second RS-232 to USB adapter is employed for the connection. The endoscope is interfaced with the laptop using an S-Video to USB adapter. These adapters and connections enable the laptop to communicate with the respective operating room equipment effectively.

3.3.2 Software

The AR software for this work was developed using Unity 3D in conjunction with the Windows Mixed Reality Toolkit (MRTK). To enhance user experience, a navigation menu was implemented, granting real-time access to the electronic clinical record and to a complete set of data from the medical instruments. Three types of interaction were incorporated to select desired data: hand gestures, vocal commands, and gaze pointing. Upon launching the application, the operator in the operating room is prompted to select a patient from the available options. The list of patients is regularly updated by a WebSocket server, which transmits the updated information to the HoloLens upon request. The AR content is then presented to the user through the navigation menu.

Navigation Menu

The navigation menu was carefully designed to ensure that each window within it maintains a consistent distance from the user, approximately 1 meter away, as depicted in Figure 3.4. This approach helps prevent discomfort or motion sickness effects during the use of the AR application. The menu comprises two main sections:

- Electronic Medical Record: Initially positioned on the left side of the menu, requiring a 90° rotation of the head to the left to access it.
- Data and video streaming from the medical equipment: Initially positioned on the right side of the menu, requiring a 90° rotation of the head to the right to access it.

As a result, the user's central view remains clear and unobstructed. However, the user has the flexibility to move and rotate the AR content using vocal commands, allowing them to adjust the content to face them directly when needed.

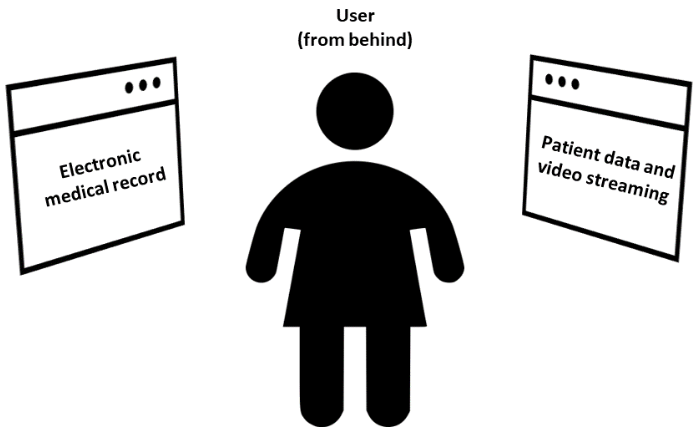

Fig. 3.4 Concept of the implemented navigation menu. Image taken from [5].

The section dedicated to displaying data from the electronic clinical record of the selected patient is divided into four categories: (i) Anamnesis, (ii) Diagnostic Tests, (iii) Blood Tests, and (iv) Clinical Diary. These data are transmitted to the HoloLens using the WebSocket protocol. A WebSocket server hosts a database of web pages specific to each patient. Accessing these web pages is possible through HTTP links and a web browser. However, by default, Unity 3D does not provide a built-in browser service for displaying web pages in an AR environment. To overcome this limitation, the PowerUI asset was installed, allowing the integration of web page display functionality within the AR application. The user has the flexibility to select the desired category for monitoring by utilizing hand gestures or the gaze pointer as input methods. This enables them to interactively navigate and access the specific data category of interest.

Communication

With regards to the real-time communication with the equipment, HoloLens receives via *Wi-Fi* the data coming from the Laptop. The Laptop, in turn, is in charge of gathering the data from the instruments connected via cable. Specifically, the Laptop receives via *UART* (i) the data from the pulmonary ventilator, implementing the *MEDIBUS* protocol, and (ii) the video streaming coming from the endoscope.

Instead, the communication between Laptop and monitor was realized by means of TCP/IP protocol by using a *Medicollector* adapter. Finally, the data are sent to the HoloLens via both *MQTT* (vitals) and *HTTP* (video streaming), which shows it in real time. In this way, the OR operator is able to evaluate in real time if the surgical procedure in progress is being adequately performed. Further details about the interfacing are provided below:

The real-time interfacing between the medical equipment and the HoloLens is facilitated through a series of communication protocols. The HoloLens receives the data wirelessly via Wi-Fi from the Laptop, which serves as an intermediary for collecting data from the instruments connected via cable. Specifically, the Laptop utilizes the UART interface to receive data from two sources. Firstly, it receives data from the pulmonary ventilator using the MEDIBUS protocol. This allows the Laptop to gather vital information related to the ventilator's operation. Secondly, the Laptop receives video streaming data from the endoscope, enabling real-time visualization of the surgical procedure. To establish communication between the Laptop and the patient monitor, the TCP/IP protocol is employed. This communication is facilitated by the Medicollector adapter, enabling the Laptop to gather important data from the patient monitor.

The collected data from both the pulmonary ventilator and the patient monitor is then transmitted to the HoloLens for real-time display. The vital sign data is transmitted via the MQTT protocol, while the video streaming is transmitted via the HTTP protocol. This seamless transmission of data allows the HoloLens to provide immediate visual feedback, enabling the operating room operator to evaluate the ongoing surgical procedure in real-time and ensure its proper execution. These interfacing details highlight the robust communication infrastructure established between the medical equipment, the Laptop, and the HoloLens, facilitating efficient monitoring and assessment of the surgical procedure.

Further details about the interfacing are provided below:

- *Ventilator data acquisition*: A MATLAB-based code implements the MEDIBUS protocol for acquiring data from the Dräger medical device. This software protocol facilitates data exchange between the medical device and external devices via an RS-232 interface. Once the protocol is initialized, the code prompts for and decodes the required vitals to be acquired. Subsequently, it transmits the data to the HoloLens using the MQTT protocol.

- *Patient monitor data acquisition*: The code responsible for acquiring data from the patient monitor is integrated into the MATLAB script used for communicating with the ventilator. This code retrieves waveforms from the monitor through the Medicollector adapter using TCP/IP. After acquiring the waveforms, the code sends them to the HoloLens via MQTT protocol. The user can select the waveform to display using hand gestures or a gaze pointer.

- *Endoscope data acquisition*: A Python 2.7 script was developed to acquire real-time video streaming from the endoscope utilizing the Imutils.video library. The acquired data is then transmitted to the HoloLens using the HTTP protocol.

The decision to use the HTTP protocol for transmitting video streaming from the endoscope to the HoloLens was based on the native video support offered by HoloLens through the Media Foundation engine. This made it convenient to employ HTTP as a protocol for adaptive multimedia content streaming. Therefore, the Unity 3D side utilizes the UnityWebRequest class to compose and handle HTTP requests. On the other hand, MQTT was chosen for transmitting the patients' vitals as it is a widely used TCP-based messaging protocol for device-to-device communication. MQTT is lightweight, scalable, and efficient for low-performance devices such as low-power HMDs, and it eliminates the need for polling, unlike RESTful over HTTP. The data exchanged is formatted in JavaScript Object Notation (JSON), a text-based data exchange format. On the Unity side, the M2Mqtt library from the M2MqttUnity asset is utilized to implement an MQTT client on the HoloLens.

3.4 System Operation

Figure 3.5 depicts the block diagram illustrating the user's operation with the AR platform. After wearing the HoloLens 2 and launching the application, the user is required to select a patient to monitor. This selection can be done using either the gaze pointer or hand gestures. The AR content appears accordingly, with three available windows:

1. The *Clinical Record* window for the selected patient, positioned initially on the left side of the navigation menu (a 90° head rotation to the left).

2. The *Vital Signs* window.

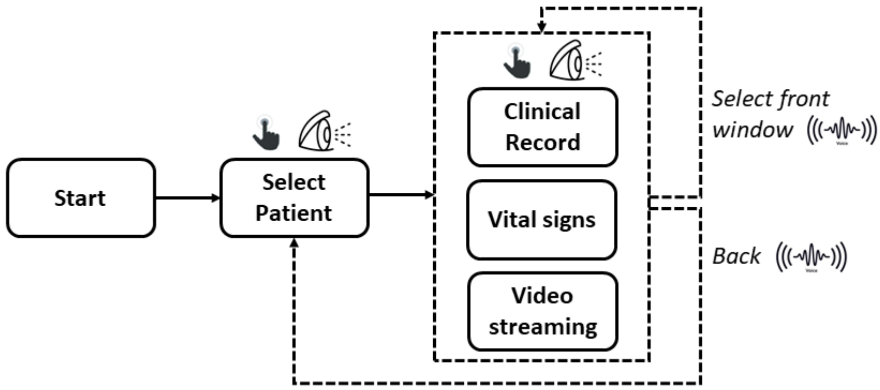

Fig. 3.5 Block diagram of the user's operation during the fruition of the AR platform. Image taken from [5].

3. The *Video Streaming* window, positioned on the right side (a 90° head rotation to the right).

Upon application launch, the frontal view is clear, and the user can turn their head sideways to view the desired AR holographic content. They can select the desired information using the gaze pointer, hand gestures, or even vocal commands to choose which window to display frontally. Finally, if the user decides to stop monitoring, they can return to the patient selection by using vocal commands.

For illustrative purposes, Figure 3.6 presents a snapshot of the *Clinical Record* menu, displaying the information seen by the user, and f the user's view when selecting the *Vital Signs* category to monitor the patient's vital signs. The displayed waveforms include Heart Rate, Respiration Rate, ECG, and O2 Saturation, obtained from the monitor. Additionally, parameters from the ventilator such as Minimum, Mean, and Peak Airway Pressure, Minute Volume, and Compliance are also monitored.

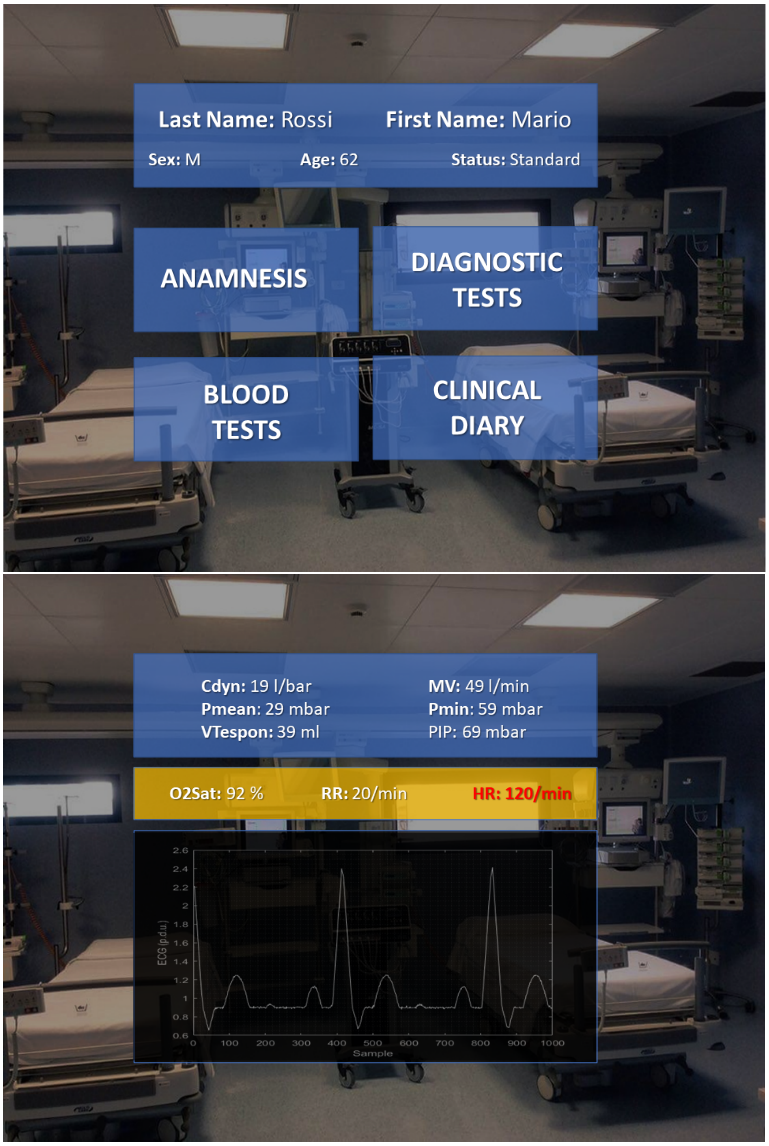

Fig. 3.6 Snapshot of the electronic clinical record window (top) and of the real-time monitored vital signs (bottom). Images taken from [5].

3.5 Performance evaluation

After the validation of the AR platform's proper functionality, experiments were conducted to evaluate two aspects: (i) real-time communication with medical equipment and (ii) the usability of the application on the AR headset. Two experimental sessions were conducted, each comprising five measurement runs. To simulate the patient's lungs, a non-self-inflating bag was connected to the pulmonary ventilator. Additionally, the patient monitor was used to monitor the vital signs of a healthy volunteer.

3.5.1 Real-time communication

In order to assess the communication with the medical equipment, two key metrics were considered: communication accuracy and time response.

The communication accuracy represents the percentage of packets that were correctly decoded by the Instrument Control Unit. It was calculated for each run using the following formula:

$$A = \frac{L - E}{L} \times 100 \tag{3.1}$$

where L is the total number of packets sent within a run and E is the number of errors occurred. The mean accuracy value μ_A and standard deviation σ_A were calculated for each session. Additionally, the 3-sigma uncertainty u_A was evaluated using the total number of runs N with the following formula:

$$u_A = \frac{k \cdot \sigma_A}{\sqrt{N}} \tag{3.2}$$

where $k = 3$ corresponds to a 99.7 % confidence level assuming a normal distribution.

On the other hand, the time response measures the time interval required by the Instrument Control Unit to transmit data to the AR headset. For each run, the mean value μ_{Ti} and standard deviation σ_{Ti} of the time response for all the packets sent were evaluated. At the end of the session, the weighted mean $\overline{\mu}T$ was calculated, taking into account the different number of packets L_i sent in each of the N runs, as expressed in Equation 3.3.

$$\overline{\mu}T = \frac{\sum i = 1^N \mu Ti \cdot L_i}{\sum_{i=1}^{N} L_i} \tag{3.3}$$

Regarding uncertainty, the 3-sigma uncertainty u_T was calculated using the law of propagation of uncertainties, as shown in Equation 3.4.

$$u_T = k \cdot \sqrt{\sum_{i=1}^{N} \left(\frac{\partial \overline{\mu} T}{\partial \mu T i} \cdot u_{Ti} \right)^2} \tag{3.4}$$

where u_{Ti} is the standard uncertainty of the time response for each run, and $k = 3$ corresponds to a 99.7 % confidence level assuming a normal distribution of the data.

Table 3.1 presents the details of the two experimental sessions. The time response measurements were below the millisecond range, while the communication accuracy exceeded 99 %. These values align with the specifications required in the healthcare field.

Table 3.1 Details of the two experimental sessions. Table taken from [5].

First experimental session				**Second experimental session**			
L	μ_T (s)	σ_T (s)	**A** (%)	**L**	μ_T (s)	σ_T (s)	**A** (%)
117	$9{\cdot}10^{-4}$	$3{\cdot}10^{-4}$	99.2	111	$9{\cdot}10^{-4}$	$4{\cdot}10^{-4}$	99.4
122	$9{\cdot}10^{-4}$	$2{\cdot}10^{-4}$	99.7	102	$8{\cdot}10^{-4}$	$2{\cdot}10^{-4}$	100.0
118	$8{\cdot}10^{-4}$	$2{\cdot}10^{-4}$	98.9	113	$17{\cdot}10^{-4}$	$6{\cdot}10^{-4}$	98.7
118	$9{\cdot}10^{-4}$	$3{\cdot}10^{-4}$	98.9	35	$7{\cdot}10^{-4}$	$2{\cdot}10^{-4}$	99.1
41	$8{\cdot}10^{-4}$	$3{\cdot}10^{-4}$	99.0	117	$9{\cdot}10^{-4}$	$3{\cdot}10^{-4}$	99.2
Total	$\overline{\mu}_T$	u_T	$\mu_A \pm u_A$	**Total**	$\overline{\mu}_T$	u_T	$\mu_A \pm u_A$
514	$9{\cdot}10^{-4}$	$3{\cdot}10^{-5}$	99.1 ± 0.4	478	$11{\cdot}10^{-4}$	$6{\cdot}10^{-5}$	99.3 ± 0.6

3.5.2 System Usability

The usability of the AR platform was evaluated by collecting feedback from all the operating room (OR) operators who extensively used the application during the experimental trials. A modified version of the System Usability Scale (SUS) questionnaire was employed to assess the usability of the platform. The obtained results were rescaled to a range of 0-100. Table 3.2 provides an overview of the modified SUS questionnaire used in the evaluation. The AR platform received positive feedback regarding its ergonomics, accommodating users wearing glasses or having long hair. Users reported no motion sickness effects while using the application, which is a crucial aspect for a comfortable and immersive experience. Most importantly, the platform was perceived as easy to use by the operators. One notable feature that was highly appreciated by the operators was the multiple options for data selection, including vocal commands, gestures, and gaze pointers. This feedback also confirms the suitability of the Microsoft HoloLens 2 headset for the AR platform. Overall, the feedback from the operators indicated that the AR platform demonstrated satisfactory usability, making it a promising tool for medical applications in the operating room.

Table 3.2 Adopted SUS questionnaire. Table taken from [5].

N.	Question	Score				
1	I think that I would like to use this system frequently	1	2	3	4	5
2	I found the system unnecessarily complex	1	2	3	4	5
3	I thought the system was easy to use	1	2	3	4	5
4	I think that I would need the support of a technical person to be able to use this system	1	2	3	4	5
5	I think the various functions in this system were well-integrated	1	2	3	4	5
6	I thought there was too much inconsistency in this system	1	2	3	4	5
7	I would imagine that most people would learn to use this system very quickly	1	2	3	4	5
8	I found the system very cumbersome to the user	1	2	3	4	5
9	I felt very confident using the system	1	2	3	4	5
10	I needed to learn a lot of things before I could get going with this system	1	2	3	4	5
11	I found the multiple choice of data selection easy to use	1	2	3	4	5
12	I felt motion sickness effects after an intensive use of the system	1	2	3	4	5

3.6 Conclusions

The integrated AR platform proposed for real-time patient monitoring during surgical procedures offers practical benefits for members of the surgical team in the operating room (OR). The platform is designed to be worn by nurses, anesthetists, or surgeons, providing them with a comprehensive set of real-time information through an AR headset. This information includes the patient's electronic clinical record, vital signs obtained from a pulmonary ventilator and a monitor for intensive care, as well as video streaming from a laparoscopic camera. By making this data readily available and easily accessible, the platform facilitates efficient and timely monitoring for OR operators. The development of the AR platform focused on meeting the stringent requirements of the healthcare sector, particularly in terms of communication accuracy and time response. Experimental results confirmed that the platform achieved high communication accuracy, exceeding 97 %, while maintaining a fast time response in the millisecond range. These results demonstrate the platform's ability to meet the demanding requirements of the healthcare field. Usability tests, conducted through the administration of SUS questionnaires, further validated the suitability of the AR monitoring platform for prolonged use. Feedback from the OR operators highlighted the platform's ease of use, ergonomic design, and absence of motion sickness effects. The multiple options for data selection, including vocal commands, gestures, and gaze pointers, were particularly appreciated by the operators. In conclusion, the proposed AR integrated platform has demonstrated its value as a reliable and supportive tool for OR operators in monitoring patients' health during delicate surgical procedures. By providing real-time access to critical information, the platform enhances the efficiency and effectiveness of patient care in the OR.

Chapter 4

Decision Support Systems for Health 4.0

A Decision Support System (DSS) is an integration of hardware and software solutions that helps healthcare professionals make informed decisions about patient care by analyzing patient data coming from measurement instrumentation and providing recommendations based on that data [118]. In the context of the digital transition in healthcare, DSSs are an essential component facilitating the shift towards data-driven approaches. With the increasing amount of digital data available in healthcare, such as electronic health records, medical imaging, and genomic data, DSSs are becoming more critical for healthcare professionals to manage and make sense of this vast information landscape [119]. To enhance the utility of DSSs, it is imperative to consider the dynamic interplay between humans and machines, emphasizing the concept of human-machine interaction. Human-machine interaction in the context of DSSs involves the seamless collaboration between healthcare professionals and computational systems. A particular collaborative approach, often referred to as *man in the loop* [120], acknowledges the human as an integral part of the decision-making process. In this paradigm, the DSS serves as a supportive tool, augmenting the capabilities of healthcare professionals. The human input becomes pivotal in refining the recommendations provided by the system, ensuring a more personalized and nuanced decision-making process. As DSSs continue to evolve, the emphasis on effective human-machine interaction becomes paramount. This collaborative model not only leverages the analytical power of algorithms and computational tools but also incorporates the expertise and contextual understanding of healthcare professionals. This symbiotic relationship between humans and machines enhances the interpretability of the generated insights and fosters a more comprehensive approach to patient care. In the following Sections, two major DSSs are described in detail. The first is aimed at evaluating the goodness of the effectiveness of scoliosis corsets, while the second is focused on the assessment of the perfusion quality in laparoscopic surgery.

4.1 Evaluation of the therapeutic effect of scoliosis corsets

In this section, an innovative system is proposed for the real-time assessment of scoliosis braces using low-cost infrared thermography instrumentation [65]. Traditionally, the evaluation of brace effectiveness heavily relies on qualitative and empirical assessments conducted by orthopedists during routine follow-up examinations. However, this evaluation is solely based on the expertise of the orthopedists involved. Currently, the only reliable methods available to validate the orthopedists' decisions involve assessing the progression of scoliosis over time, often requiring the use of ionizing radiations. Therefore, the proposed system aims to fulfill the requirements of real-time monitoring and objective evaluation in a non-harmful manner. This is achieved by exploiting the thermoelastic effect and correlating temperature changes on the patients' backs with the mechanical pressure applied by the braces. An experimental campaign was carried out at an accredited orthopedic center under normal operating conditions, involving twenty-one patients in the juvenile and adolescent age groups. The system's performance was then evaluated using appropriate validation techniques. The experimental results demonstrate a classification accuracy slightly below 70 %, which shows promise for further advancements aimed at considering the use of such systems in orthopedic centers.

4.1.1 Rationale

According to [65], *"Scoliosis is defined as a complex deformity of the backbone and the torso that occurs in three dimensions [121, 122] and consists of a lateral curvature with a vertebral rotation [123]. The standard screening test for scoliosis is the forward bending test [123], during which the patient is asked to bend forward with straight knees, while the examiner observes the back for any signs of asymmetry. If the results of the test, along with the patient's medical history, raise suspicion of scoliosis, radiography becomes crucial for further evaluation [124]. Once radiography is acquired, scoliosis is identified by means of the measurement of the Cobb angle, which quantifies the degree of spinal curvature by measuring the angle between the two most inclined vertebrae at the top and at the bottom of the curve [125, 126]. In particular, scoliosis is diagnosed when this angle exceeds 10° [127]".*

The related causes can be classified as neuromuscular [128], syndrome-related [123], congenital [129], and idiopathic [130]. This latter represents the majority of scoliosis cases since it is identified as a multi-factor spinal deformity with unknown etiology. Additionally to the relevant cosmetic deformity, idiopathic scoliosis poses risks in terms of cardiac and pulmonary impairments [131]. Scoliosis classification varies based on the patient's age. It is categorized as infantile, juvenile, and adolescent scoliosis, corresponding to patients aged 0-3 years, 4-10 years, and older than 10 years, respectively [123]. Other classification systems consider the number of curves and the type of deformity [132].

With regards to the treatments, they encompass various approaches including observation, physiotherapy, bracing, and, in extreme cases, surgery [133]. Surgery is typically reserved for cases where the Cobb angle exceeds 50° [134], while scoliosis braces are widely utilized as a treatment option for patients with incomplete bone growth and Cobb angles ranging between 25° and 50° [124, 134]. In this specific scenario, patients are fitted with a rigid or semi-rigid corset-like device. The selection of the brace model depends on factors such as the patient's bone maturity, measured Cobb angle, and specific characteristics of the spinal deformity [124]. Common brace models include the *Milwaukee*, *Lyonnaise*, *Cheneau*, *Sforzesco*, among others [124].

The customized corset is designed to conform to the patient's specific torso and, aiming to straighten and correct the spinal curvature caused by scoliosis, applies external pressure to the affected areas of the backbone. This pressure is exerted unilaterally, targeting the curvature on one side of the backbone. Throughout the treatment process, regular follow-up examinations are essential to assess brace compliance and make necessary adjustments to the corset in response to changes in the patient's body [135], ensuring appropriate pressure application. However, there is currently no consensus in the literature regarding the implementation of these brace corrections [134], and there is a lack of agreement on the mechanical principles guiding brace design and manufacturing [130, 136]. Consequently, the determination of whether the pressure exerted by the brace is considered "adequate" or "inadequate" largely depends on the expertise of the orthopedist [137, 122]. As a result, the most reliable measure to validate the orthopedist's decision is the assessment of curve progression, typically achieved by comparing the Cobb angle measured from radiographic imaging obtained over a specific time frame [138].

As deduced, this approach necessitates a specific time interval between two measurements of the Cobb angle. Moreover, the utilization of radiographic imaging poses potential limitations due to the associated risks of repeated ionizing radiation exposure over time. If alternative radiation-free methods, such as Moiré topography [139] or 3D scanning [140], are employed to assess the curve progression by means of asymmetry indexes, the time horizon between two acquisitions could be considerably shortened. Nevertheless, according to [65], *"evaluation remains not feasible, as the gradual reduction of spinal curvature can be achieved only with the prolonged wearing of the brace by the patient. Moreover, another crucial aspect is that failure to wear the corset correctly by the patients could result in a deterioration of scoliosis, even if the corset has been properly designed. Therefore, a comparison between two measurements over time may not accurately reflect the effectiveness of the corset if it is not consistently worn as prescribed. Consequently, patients still currently lack an objective means of monitoring the effectiveness of their corsets in real-time, which would enable prompt adjustments to be made"* [65, 139, 140].

A first attempt to enable real-time evaluation was introduced in a previous study [132]. This approach involved monitoring the mechanical pressure exerted by the brace by means of the usage of pressure sensors positioned between the brace itself and the patient's backbone. However, accurately measuring the existing pressure between these two surfaces, while still consistently moving the sensor, proved to be challenging, as it required ensuring reliability, repeatability, and cost-effectiveness in view of widespread implementation in healthcare facilities.

Based on these considerations, the current study presents an innovative, non-invasive, and cost-effective approach to evaluate the effectiveness of scoliosis braces in real-time. The proposed system leverages low-cost infrared thermography (IRT) instrumentation to capture the skin temperature of the patients' backbones. By processing the acquired temperature data, the system can determine whether the mechanical pressure applied by the corset is considered "adequate" or "inadequate" based on the orthopedic prescription and brace design. This system represents a fully-fledged decision-support system, which is a prominent manifestation of the "4.0" digital transition in healthcare [141]. Its primary goal is to provide orthopedists with a reliable and objective assessment, enabling them to promptly identify the need for adjustments to the corset and enhance the scoliosis treatment process.

4.1.2 Background

IRT, or infrared thermography, is a non-invasive technology that operates by detecting and capturing emitted radiation energy within the wavelength range of 2 to 15 μm [142]. This detection is achieved through an array of detectors in charge of converting the energy into a thermal image [143]. The amount of energy emitted by an object is influenced by various factors, including wavelength, surface temperature, and emissivity. Emissivity refers to the ratio between the amount of infrared energy emitted by an object and that emitted by an ideal black body considering the same wavelength and temperature [144]. Different objects possess different emissivity values, meaning they can emit the same amount of thermal energy even if they have different temperatures. Additionally, when using infrared detectors in order to measure the infrared energy emitted by a certain object, the measured value is not solely influenced by the energy emitted by the object itself. It is also affected by the energy absorbed, reflected, and emitted by the surrounding environment [143]. Furthermore, the measured value is dependent on the distance between the object's surface and the camera. To ensure measurement repeatability, it is crucial to acquire thermal images of objects from a consistent distance and in a consistent environment [145].

IRT technology has seen widespread adoption in various fields, including electrical engineering [146], mechanical engineering [147], agriculture [148], veterinary medicine [149], and healthcare [150]. In the healthcare sector, IRT has made significant advancements, benefiting from improved detector sensitivity, cost reductions [151, 145], and integration within the context of the "4.0" digital transition. This transition leverages technologies like Augmented Reality [32], Internet of Things [152], Cloud Computing [153], and Artificial Intelligence [154, 3]. In fact, these advancements have led to the development of infrared cameras that can be attached to smartphones, providing improved portability, connectivity, and also ease of use, still without compromising performance compared to traditional devices [155]. This has paved the way for the emergence of decision-support systems that provide healthcare professionals with fast, reliable, and objective results in various scenarios. These systems are used for evaluating inflammatory processes [156], detecting infections [157], monitoring diabetes-related conditions [158], and assessing eye diseases [159]. In the field of rehabilitation and orthopedics, such systems are employed for ergonomic evaluations [6], injury prevention and assessments [160, 161], scoliosis diagnosis [162, 163], and brace manufacturing [164]. As an example, Fig. 4.1 illustrates two acquired thermal images of a subject.

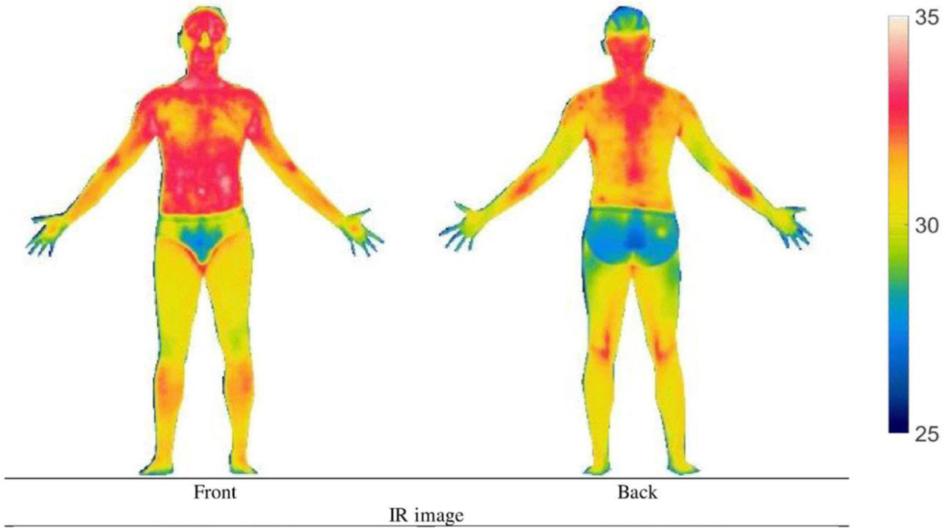

Fig. 4.1 IR images of an individual's whole body. Image taken from [6].

All the aforementioned scenarios necessitate a deep understanding of the relationship between the human body and the corresponding emitted thermal energy. In essence, human skin exhibits a constant emissivity in the 3-15 μm range, with a value of approximately 0.97 ± 0.05, which is close to that of a black body [145]. The thermal energy emitted by the human body can be primarily attributed to factors such as blood perfusion, metabolism, and external sources [150, 165], including electromagnetic fields or mechanical loading [150]. In the case of evaluating the effectiveness of scoliosis corsets, the relationship between mechanical loading and emitted thermal energy enables the utilization of IRT for assessing the stress imposed on the body. This analysis is known as Thermoelastic Stress Analysis (TSA), which relies on the thermoelastic effect. The thermoelastic effect establishes a linear correlation between changes in body temperature (and thus emitted thermal energy) and stress states on the body's surface, assuming local adiabatic conditions [150].

Considering all these factors, it becomes evident that within the framework of evaluating the effectiveness of scoliosis corsets, TSA could serve as a robust foundation. By employing suitable acquisition and processing techniques for thermal images of patients' backbones, TSA can be leveraged to determine whether the pressure applied by the scoliosis corset is adequate.

4.1.3 Design

Drawing upon the considerations expounded in Section 4.1.1 and 4.1.2, this study introduces a system designed to evaluate the efficacy of a scoliosis corset, serving as a decision support tool for orthopedic specialists. The proposed system endeavors to furnish an objective assessment, discerning whether the corset functions adequately or not, by capitalizing on the interrelation between fluctuations in skin temperature and applied mechanical pressure (as elucidated in Section 4.1.2), thereby streamlining clinical decision-making. The system operates as depicted in Fig. 4.2, comprising three pivotal modules, namely the *preparation of regions of interest (ROIs)*, *processing of ROIs*, and the *decision* module.

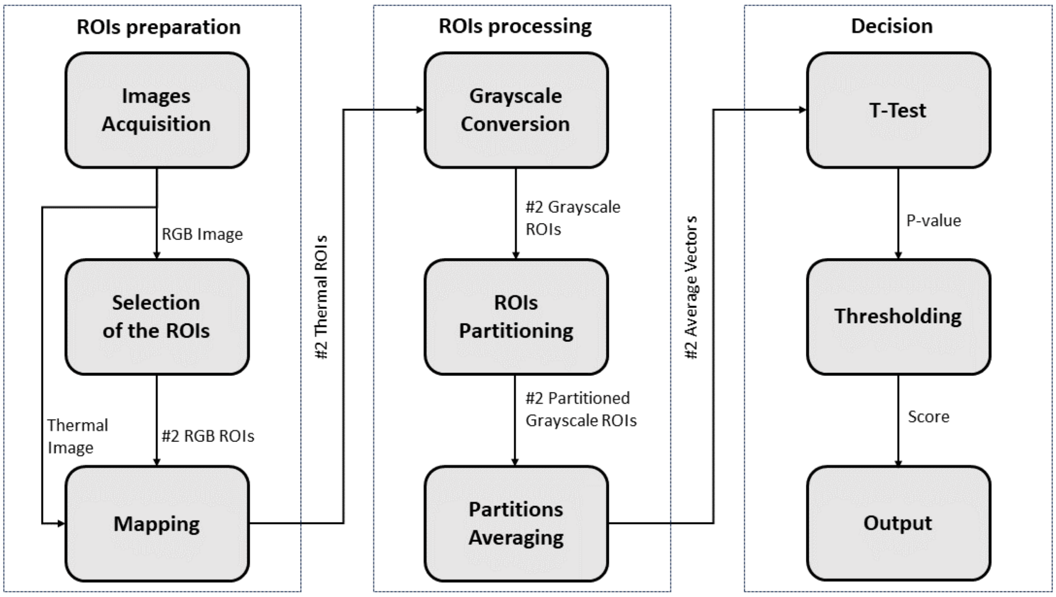

Fig. 4.2 Conceptual description of the proposed system

1. The module responsible for preparing the regions of interest (ROIs) is divided into three blocks. The initial block, denoted as "Images Acquisition," captures both thermal and corresponding RGB images of the patients' dorsum. It is important to note that the patient's back remains uncovered during this stage. To ensure the visibility of the bracing effect, orthopedic specialists recommend a time limit of no more than one minute between the removal of the scoliosis corset by the patient and the commencement of image capture. Several factors, such as the duration of brace usage, the intensity of applied pressure, and

individual metabolism, can influence the duration of the corset's pressure effect on skin temperature variation after removal. This effect may gradually diminish within a few minutes or persist for an extended period, ranging from several minutes to tens of minutes (Gulyaev et al., 1995; Hart et al., 2004).

The second block, termed "Selection of the ROIs," involves the manual selection of two symmetrical Regions of Interest (ROIs) from the RGB image by the orthopedic specialist. The first ROI corresponds to the area where the brace exerts pressure, while the second ROI is chosen symmetrically with respect to the backbone. The selection process takes into account the patient's clinical history, including access to radiography, knowledge of the diagnosis, type of corset worn, and related prescription. This information enables the identification of the specific region of the back where the corset should exert its effect. To avoid confirmation bias, the selection of the ROIs is performed on the RGB image rather than the thermal image. Subsequently, the third block, referred to as "Mapping," maps the selected regions from the RGB image onto the thermal image.

2. The module for processing the ROIs is also divided into three blocks. The first block, named "Grayscale Conversion," converts the thermal ROIs from the RGB color space to grayscale. This conversion assigns the maximum temperature value to the white color and the minimum temperature value to the black color. Consequently, each ROI undergoes a transformation from three-dimensional (red, green, and blue channels) to one-dimensional (grayscale).

   Next, the "ROIs Partitioning" block divides each grayscale ROI by performing horizontal and vertical slicing. As a result, each ROI is segmented into subregions with dimensions of $N \times M$, where N represents the number of horizontal slices and M represents the number of vertical slices.

   The final block, referred to as "Partitions Averaging," computes the average value for each of the subregions within the partitioned grayscale ROIs. This process generates two vectors, each with dimensions of $[N \times M, 1]$, representing the averaged values of the subregions for each ROI.

3. The two vectors obtained from the ROIs processing module are compared using the "Decision" module. Specifically, the Student's T-Test is performed between the two vectors to evaluate whether there is a statistically significant difference in the means of the two groups represented by the vectors. Clearly,

a preliminary investigation about the normality of the data was conducted by means of a χ^2 test. The output of the T-Test is the p-value, indicating the probability of obtaining test results as extreme as the observed result, assuming that the null hypothesis is true. In this context, the null hypothesis implies no significant difference between the two vectors, suggesting inadequate scoliosis brace pressure. A lower p-value indicates a lower probability of erroneously rejecting the null hypothesis. Therefore, the resulting p-value is compared with a predefined threshold, determined through a learning process, to associate it with an output that indicates whether the scoliosis brace is functioning adequately or not.

Specifically, if the obtained p-value is below the threshold and the average temperature of ROI #1 (region where brace pressure is expected) is higher than that of ROI #2 (region where brace pressure is not expected), the pressure of the scoliosis corset is deemed adequate. Conversely, if the p-value exceeds the threshold, it is considered inadequate.

A graphical representation of the proposed system is depicted in Fig. 4.3. The figure highlights the three modules (*ROIs preparation*, *ROIs processing*, and *Decision*), along with the internal blocks related to: the selection of the ROIs (a), the mapping onto the thermal image (b), the partitioning and grayscale conversion (c), the averaging of the partitions (d) that generates two vectors v of length $L = N \times M$, the T-Test (e), and finally, the thresholding and output assessment (f), where the output is 0 if the corset pressure is inadequate and 1 otherwise.

4.1.4 Experimental Validation

In this section, the on-field case study conducted at *Ortopedia Ruggiero* in Cardito (Naples, Italy) is described, along with the obtained experimental results pertaining to the evaluation of the proposed system's performance.

The study adhered to the guidelines specified in the Declaration of Helsinki. As the data for this study were collected during routine clinical practice, formal approval from the institutional review committee was not required. However, informed consent for the surgical procedure and the utilization of patient data by third parties was obtained from the parents or legal guardians of each participant.

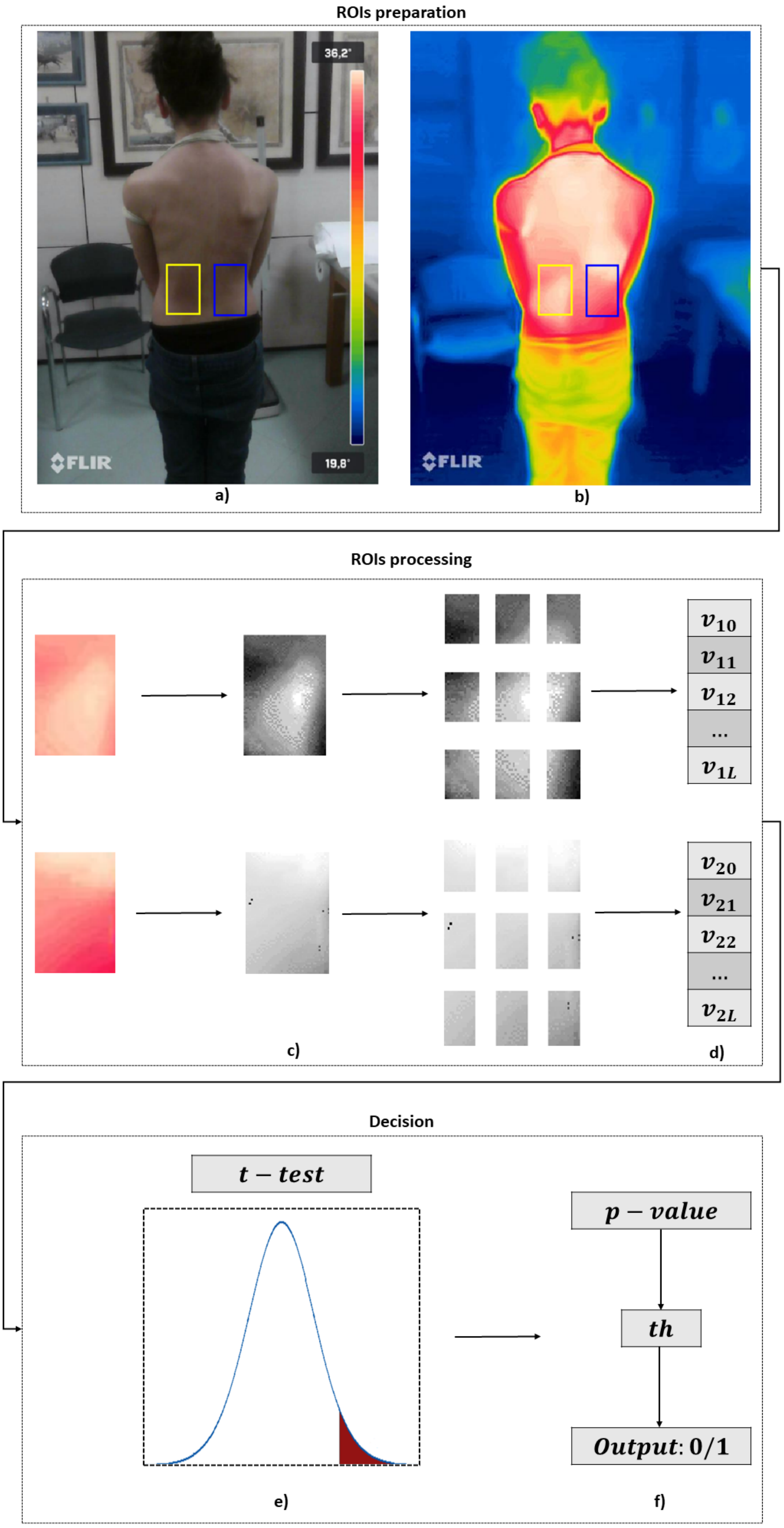

Fig. 4.3 Graphical representation of the proposed system: a) Selection of the ROIs; b) Mapping; c) ROIs Partitioning and Grayscale Conversion; d) Partitions Averaging; e) T-Test; f) Thresholding and Output.

Setup

The experimental campaign comprised a cohort of twenty-one patients, consisting of both juvenile and adolescent individuals, with fourteen of them being females. All patients were diagnosed with idiopathic scoliosis and were undergoing bracing treatment as prescribed by the specialist, making them ineligible for surgery. The prescribed braces varied depending on the individual's condition. Specifically, nine patients had dorsal or lumbar scoliosis, while the remaining twelve had dorso-lumbar scoliosis with a double curve of the spine.

Importantly, none of the patients had any chronic or acute health conditions known to cause temperature fluctuations on the skin surface. Nineteen patients participated in the experimentation once, while two patients were involved in the study on two separate occasions.

To provide an illustrative example, Figure 4.4 displays different models of braces worn by the subjects participating in the experimental campaign.

Fig. 4.4 Different braces models worn by subjects involved in the experimental campaign.

Before the infrared (IR) acquisition, patients were instructed to avoid consuming stimulant beverages, engaging in physical activity, applying body creams, and wearing jewelry. The experimental campaign was conducted in a conditioned room with non-direct airflow, maintaining a temperature between 19°C and 23°C to simulate real operating conditions.

Upon arrival at the facility, patients' radiographs and orthopedist prescriptions were collected. Subsequently, they were guided to a designated room to rest and acclimate for approximately fifteen minutes. During this time, the orthopedist performed a standard examination, including assessing the compliance of the brace through manual procedures. To ensure measurement repeatability and reproducibility, each patient was positioned at a consistent distance from the camera. A marked spot on the floor, located 1 meter away from the IR camera, served as the reference point. Careful attention was given to avoiding any obstacles between the IR camera and the patient's back. After the acclimatization period, *"patients were instructed to undress and remove the brace, allowing for thermal images of their back to be captured. This step ensured that any interference caused by the brace material was eliminated, enabling clear visualization of the thermal effects resulting from the brace's applied pressure. The thermal images were acquired within one minute of brace removal, enabling the observation of the temperature increase caused by the brace's pressure." [65] "The thermal images were captured using the FLIR ONE Pro thermal imaging camera [166], an affordable camera that attaches to smartphones. The cost of this camera is approximately $450 USD. In terms of metrological performance, the camera provides an accuracy of 3°C when operated within a temperature range of 15 to 35°C and when measuring object temperatures ranging from 0 to 120°C. The thermal sensitivity of the camera is 100 mK. The thermal sensor operates within a spectral range of 8 to 14 µm, covering the range of interest from 8 to 12 µm. The acquired data are stored directly on the smartphone as an image with dimensions of 1440x1080 pixels, while the thermal resolution of the camera is 160x120 pixels" [65].* For a comprehensive understanding, Figure 4.5 presents a schematic representation of the acquisition system.

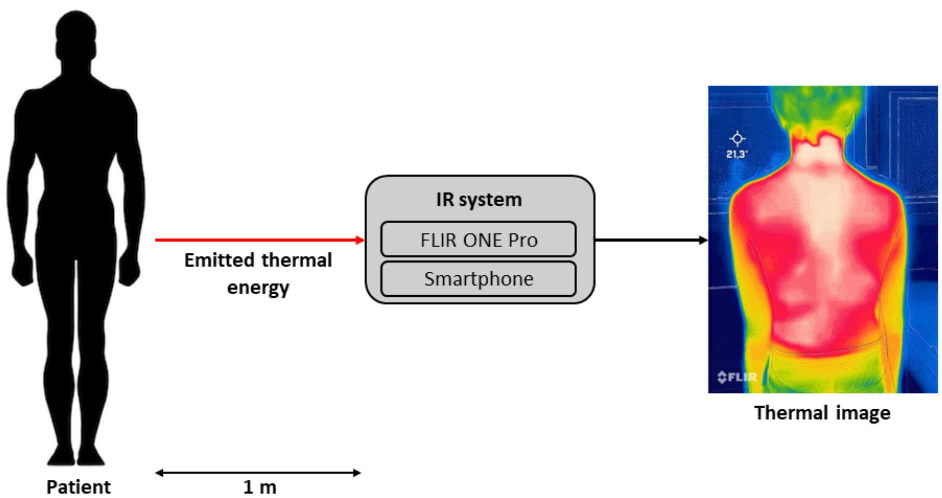

Fig. 4.5 Sketch of the acquisition system.

By the conclusion of the experimental campaign, a total of 21 pairs of RGB/thermal images were acquired (one for each patient). For each RGB image, the medical team followed the procedure outlined in Section 4.1.3 to select the pairs of Regions of Interest (ROIs). As patients were affected by single or double curvature of the backbone, in some cases two pairs of ROIs were considered for a patient. Overall, 36 pairs of ROIs were selected. Subsequently, a label Y_i was assigned to each pair of ROIs to indicate the pressure applied by the brace, classified as either *adequate/1* or *inadequate/0*. To minimize subjective evaluations from a single operator and mitigate the potential for bias, the labeling process adhered to a majority rule, where multiple members of the medical team contributed to the decision-making process. This approach aimed to ensure objectivity and consistency in the assignment of labels.

Results

The obtained 36 pairs of ROIs were processed following the steps outlined in the "ROIs processing" module depicted in Figure 4.2. Consequently, the dataset for analysis consisted of 36 scores X_i, each associated with a corresponding label Y_i.

To assess the performance of the proposed system in terms of classification accuracy (defined as the percentage of instances correctly classified) and its generalization capability (preventing overfitting), a leave-one-out cross-validation (LOOCV) strategy was employed. LOOCV is a widely used method for evaluating the performance and generalization ability of a classifier within a dataset. It is a form of k-fold cross-validation where k is equal to the number of instances in the dataset.

In LOOCV, the dataset is divided into k subsets or folds, with each fold containing only one instance. The model is then trained on $k-1$ folds and evaluated on the remaining fold. This process is repeated k times, ensuring that each instance serves as the test set once. LOOCV provides an effective approach for assessing the performance and generalization of the system while mitigating the potential bias introduced by a specific test set.

In this study, the training process involved performing a grid search over 1000 different values of the threshold parameter th, ranging from 0.005 to 0.500. For each iteration of the LOOCV process, the threshold value th_{max} that maximized the classification accuracy on the training folds ($k-1$ folds) was applied to the test fold k. This allowed for an evaluation of the model's performance on unseen data.

However, given the relevant imbalance of classes in the dataset, with only 10 instances labeled as *inadequate/0* pressure and 26 ones labeled as *adequate/1* pressure, a balancing procedure was conducted prior to applying LOOCV. Ten random subsets were created from the original dataset, so that it was ensured that each subset contained 20 instances with a balanced distribution of half labeled as 0 and the remaining half labeled as 1.

Subsequently, LOOCV was applied to each of the ten subsets, resulting in ten different values of averaged classification accuracy and associated standard uncertainty (evaluated as type-A uncertainty [92]). By considering these multiple subsets, the overall mean value and uncertainty provide a robust indication of the system's performance on unseen data. Figure 4.6 illustrates the conducted evaluation of the system's performance.

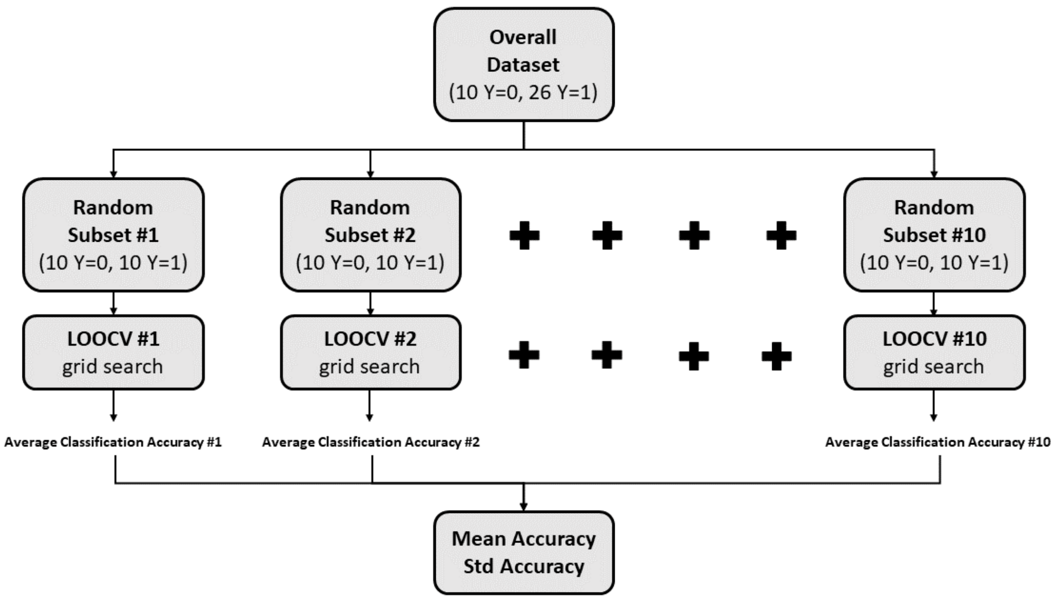

Fig. 4.6 Description of the evaluation of the system performance.

Tab. 4.1 displays the averaged accuracy (A) values and their corresponding standard uncertainties (u) for each subset, expressed as percentages.

Metric	Set #1	Set #2	Set #3	Set #4	Set #5	Set #6	Set #7	Set #8	Set #9	Set #10	Mean
A (%)	70.0	55.0	65.0	75.0	65.0	70.0	60.0	65.0	65.0	65.0	**65.5**
u (%)	10.5	11.4	10.9	9.9	10.9	10.5	11.2	10.9	10.9	10.9	**3.4**

Table 4.1 Accuracy (A) and corresponding standard uncertainty (u) obtained for each subset and averaged.

After evaluating the system's performance, a grid search for the threshold parameter th is repeated on the entire dataset to extract as much information as possible from the data [167]. This process aims to find the best threshold value (th_{best}) to be used in real-time scenarios for clinical evaluations. The overall mean accuracy (A_m) is determined to be 65.5 %, with an associated standard uncertainty (u_m) of 3.4 %, evaluated using the first-order law of propagation of uncertainty [92]. Assuming a normal distribution and a confidence interval of 95 %, a coverage factor (k) of 2 is applied to obtain the expanded uncertainty ($U_m = k \cdot u_m$), expressing the measurement results as (65.5 ± 6.8) %.

4.2 Evaluation of the blood perfusion quality in laparoscopic surgery

In this Section, the innovative algorithm proposed for laparoscopic colorectal surgery in [7] and aimed at automatically assessing the perfusion quality of the blood in intestinal sectors is described. Typically, the homogeneity of luminosity in indocyanine green-based fluorescence imaging is evaluated solely through a qualitative and empirical assessment that significantly depends on the surgeon's subjective judgment. Consequently, this leads to evaluations that are highly experience-dependent. In order to overcome this bottleneck, the algorithm described in this study evaluates the degree and consistency of indocyanine green administration during laparoscopic surgery. The algorithm utilizes a Feed-Forward Neural Network, which receives a feature vector as input. This feature vector is based on the histogram of the green band of the input image. The algorithm is used for two primary purposes: (i) to obtain information related to the perfusion during surgery, and (ii) to assist the surgeon in objectively evaluating the outcome of the procedure. Specifically, the algorithm produces an output that classifies the perfusion as either adequate or inadequate. The validation of the algorithm was performed on a set of videos captured during surgical procedures conducted at the University Hospital *Federico II* (Naples, Italy). The results obtained showcase a classification accuracy of 99.9 %, and a repeatability of 1.9 %. Ultimately, the effectiveness of the proposed algorithm's real-time functionality was assessed by analyzing video streaming captured directly from an endoscope located in the operating room.

4.2.1 Rationale

Indocyanine green (ICG) is a molecule that was developed at Kodak's Research and Development laboratories in the 1950s [168]. It was originally intended for use in infrared photography, and has since found various other applications. This molecule was the first substance discovered to be able to emit fluorescence in the spectrum of the near-infrared (NIR). Specifically, it gets fluorescent when it is illuminated with infrared light. Such substance has been found to have negligible toxicity and is quickly eliminated by the body without any significant side effects, except in rare cases of allergic reactions which can be easily prevented [169]. In 1959, the use of indocyanine green (ICG) was approved by the Food and Drug Administration (FDA) for clinical applications [170]. Since then, it has been extensively utilized as a diagnostic tool for various pathologies affecting the heart, eyes, liver, and lungs. This substance is typically administered by injection into the patient's vein prior to surgery or near the tumor mass to be removed the day before surgery. Once in the body, the molecule binds to plasma proteins present in the blood, thereby imparting its fluorescent properties to the blood, liver, and biliary circulation [171].

More recently, the use of ICG has become widespread in the field of surgery due to the development of fluorescence detectors, which are optical systems designed for the excitation and detection of emitted fluorescence. One important area of research involving ICG is its use in estimating perfusion quality during laparoscopic surgery [172–177]. This is a critical step in assessing whether the intestine is adequately perfused, which serves as an indication of the overall outcome of the procedure [178–180]. In fact, a deficiency in perfusion at the site of an anastomosis increases the risk of anastomotic dehiscence, which refers to the failure of sutures to heal properly and can lead to the development of fistulas and compromised tissue perfusion [181]. Therefore, assessing the quality of perfusion using ICG allows the surgeon to intervene promptly during the ongoing surgical procedure.

The most commonly used technique for verifying the perfusion of an intestinal segment is to inject ICG into the patient's body. This makes the blood fluorescent with a green tinge when illuminated with infrared light. The evaluation of the intensity and uniformity of this fluorescence allows the surgeon to determine whether the tissue is adequately perfused. This technique has been successfully used by Boni [181] to provide information related to perfusion during colorectal surgery and assist the surgeon in adopting the best strategy during colorectal anastomosis, which is often necessary in colorectal interventions where two conical stumps need to be stitched. In addition, ICG has been used for other applications such as dynamic discrimination of primary colorectal cancer using systemic indocyanine green with NIR endoscopy [182], intraoperative ureter identification, and lymph node dissection [183]. At present, the brightness of ICG fluorescence is evaluated solely on a qualitative and subjective basis by the surgeon, relying on personal experience. However, there is currently no established technique or system available to quantify fluorescence brightness objectively and support surgical assessments. Despite several efforts to design systems capable of assisting surgeons in the assessment of perfusion quality, including those described in [184–187], none have been successful in quantifying the fluorescence brightness of ICG in a reliable and objective manner. These approaches are primarily founded on the rate of indocyanine diffusion within the tissues. The perfusion of the colorectal segment is evaluated by analyzing the gradient related to the intensity of ICG fluorescence brightness captured by a camera. The resulting output is a heat map that highlights the areas of the intestine characterized by a more rapid increase of ICG fluorescence brightness after injection. Additionally, these methods attempt to correlate the heat map with the post-surgery outcome. Nevertheless, it should be noted that the techniques presented in [184–187] lack the ability to automatically and objectively evaluate the quality of perfusion in the analyzed region. These methods only generate a graphical output, leaving the subjective interpretation of the results to the surgeon.

In order to address this challenge, an increasingly popular field of technology is being adopted, namely Artificial Intelligence (AI) [188, 189], specifically Machine Learning (ML). The combination of powerful computing capabilities and the development of effective algorithms by researchers [190–192] has contributed to the widespread adoption of ML in a wide range of applications, including healthcare [193]. Currently, there are many examples of ML-based approaches being used in the medical field [194–196], providing evidence that this technology can assist medical professionals in minimizing patient risks and preventing complications.

In the healthcare field, there exist many examples of ML-based approaches, such as the development of a symptom-to-disease digital health assistant in [194] which achieved a high accuracy of over 90 % in differentiating over 20,000 diseases. Another study in [195] proposed an AI-based diabetic retinopathy screening model in endocrinology outpatient settings, with a sensitivity and specificity of 92 % and 93 %, respectively. In [196], AI was used for tuberculosis detection in chest radiographs, with a sensitivity of 95 %. Additionally, an original ML-based maxillofacial fracture detection system was proposed in [197] to detect traumatic fractures in patients. According to Steele [198], ML models applied to electronic health records can outperform conventional models for predicting patient risks. In addition, Cahill et al. [199] proposed a decision support system based on AI for intra-operative tissue classification in colorectal cancer. Park et al. [200] explored the feasibility of using AI-based real-time analysis of microperfusion to predict the risk of anastomotic complications in patients undergoing laparoscopic colorectal cancer surgery. Igaki et al. [201] conducted the first study using an image-guided navigation system with total mesorectal excision. Sanchez et al. [202] conducted a systematic literature review on the use of AI in finding colorectal polyps in colonoscopy. Finally, Kitaguchi et al. [203] used AI to identify laparoscopic surgical videos, aiming to automate time-consuming manual processes such as video analysis, indexing, and video-based skill assessment.

Therefore, in the study published in [7], a ML-based system that aims to objectively assess the adequacy of intestinal perfusion after an injection of ICG is proposed. The system is designed to provide surgeons with an automated tool that can assist in assessing the outcome of laparoscopic colorectal surgery. Specifically, the algorithm is capable of classifying the perfusion as either "adequate" or "inadequate", providing surgeons with a reliable, objective assessment of the procedure. The system works on a video extracted from a laparoscopic camera and a Region of Interest (ROI) selected by the surgeon, which contains the area to be assessed. The system uses a set of pre-processing steps to prepare the input for a Feed-Forward Neural Network, which is used to evaluate the quality of perfusion. The neural network hyper-parameters are precisely tuned to achieve a high prediction accuracy, making the proposed architecture suitable for standard routine adoption during surgery. The feasibility of the system is demonstrated through a proof-of-concept case study, which involves perfusion analysis applied to abdominal laparoscopic surgery at University Hospital Federico II in Naples, Italy. The system's optimal performance in real time proves its effectiveness as a decision support tool for both less-experienced surgeons and those at the beginning of the learning curve.

4.2.2 Design

The issue tackled in this study can be expressed formally as a binary classification problem that deals with identifying frames from a video stream that correspond to an ROI with either *adequate* or *inadequate* perfusion. To address this issue, the objective was to develop an automated system capable of quantitatively assessing the amount of ICG present in the ROI. This was achieved by computing the histogram of the green band of the acquired frames and producing an output that corresponds to either adequate or inadequate perfusion.

The present study was conducted in compliance with the principles outlined in the Declaration of Helsinki. As the investigation did not involve any pharmacological experimentation, medical devices, or patient data, but solely relied on the computer-based analysis of video material collected during routine clinical practice, the Ethics Committee's approval was deemed unnecessary. Prior to the surgical procedure, each patient provided written informed consent, which included approval for third-party use of their data.

System Architecture

The overall architecture of the proposed system is shown in Fig. 4.7.

Fig. 4.7 Functional blocks of the proposed algorithm. Three main blocks are outlined: the first block implements a fast-tracking algorithm to track the selected Region of Interest (ROI). The second block performs feature extraction on the available frames as a pre-processing step. Finally, a Machine Learning (ML)-based classifier is utilized in the third block to provide the output in terms of the quality of perfusion. Image taken from [7].

The proposed system takes two inputs: (i) frames captured from the video streaming and (ii) an ROI identified as a rectangular box selected by the user. The ROI indicates the portion of the frame that requires analysis and is selected using the mouse or the trackpad on the computer, facilitated by the OR operator, at the beginning of the algorithm.

The architecture of the system, from left to right, comprises the following three functional blocks:

- The first functional block of the proposed system employs a Fast tracking algorithm to track the selected ROI during video execution. The *Minimum Output Sum of Squared Error* (MOSSE) tracker [204] was utilized for this purpose. The MOSSE algorithm uses adaptive correlation to track objects, resulting in better robustness against variations in lighting, pose, scale, and non-rigid transformations. The MOSSE tracker also implements an auto pause and resume functionality, which comes into effect if the object to track disappears (for instance, if the surgeon covers it) and then reappears. Additionally, the MOSSE tracker can work at high frame rates, exceeding 450 fps.

- After extracting the frames containing the ROI from the video source, the second functional block performs Features extraction. The frames are in the RGB format, where each colored image is obtained by combining three images, one for each color channel: red, green, and blue. Each pixel has an 8-bit resolution, representing the intensity of the pixel. Subsequently, the ROI of each frame is partitioned into 20 vertical equal slices, and for each slice, the histogram of the green band and its area are computed using Eq 4.1:

$$A_i = \sum_{l=k}^{255} count_i(l) \cdot (b(l+1) - b(l)) \qquad 1 \leq i \leq 20 \tag{4.1}$$

  where A_i represents the generic element of the features vector corresponding to the slice i, $b(l)$ is the bin value at level l, $count_i(l)$ is the number of occurrences of the green intensity at level l for slice i, and k is a parameter that excludes pixels with low values of green. In this study, a value of $k = 25$ was selected, as it yielded the best classification performance. Subsequently, a features vector comprising 20 elements is generated. This vector serves as the input to the final functional block.

- The final block of the proposed algorithm utilizes a Feed Forward Neural Network to perform binary classification of the feature vector, determining whether it corresponds to an adequate (1) or inadequate (0) perfusion of the colorectal portion. The binary cross-entropy was selected as the loss function and the optimizer used was Adam, as described in [205, 206].

Model Evaluation and Selection

The following neural networks (NN) were evaluated as classifiers in an experimental study.

- The first type of NN tested was a one-hidden-layer NN, which utilized a classic feedforward neural network (FFNN) with a single neuron in the output layer having a sigmoidal activation function. The hidden layer was first tested with 20 neurons and a rectified linear unit (ReLU) activation function and then with 80 neurons and a hyperbolic tangent (Tanh) activation function. Furthermore, this network was tested with three additional activation functions:

Tanh, Sigmoid, and ReLU. For each activation function, the number of neurons varied between 10 and 100, with an increment of 10.

- The second type of NN tested was a two-hidden-layer FFNN composed of different combinations of ReLU, Sigmoid, and Tanh activation functions with 50, 70, and 90 neurons. The output layer used the softmax activation function with two neurons.

The tuned hyperparameters in the study were the activation functions and the number of neurons in each hidden layer. Additionally, a Support Vector Machine (SVM) method with linear and Gaussian kernels was used as a baseline classifier. All ML models were validated on the entire dataset using 10-fold cross-validation (CV) to assess and select the best model in a statistically significant manner without overfitting [207]. In K-fold CV, the data set is divided into K folds, and the network is trained K times for each combination of hyperparameters. According to [7], *"each time the network is trained, one of the K folds of the data set is used as a test set, and all the remaining K-1 folds are used as training sets. The selection of the best model was conducted based on the mean of the obtained accuracies over the K test folds, defined as the percentage of correct classification"*.

After the selection, the chosen model was retrained on the entire dataset to extract as much information as possible from the data [167] for use in a real-time surgical scenario. The proposed algorithm was developed in Python 2.7 on Windows 10, utilizing the open-source frameworks and libraries TensorFlow, Keras, and OpenCV. The training of the proposed NNs was conducted using a batch size of 5 for 100 epochs.

4.2.3 Performance evaluation

This section discusses two validation phases of the proposed algorithm. The first phase is the laboratory experimental validation, which involved the use of a dataset provided by surgeons to train and validate the ML classifiers used by the algorithm. The second phase is an online validation in the operating room, which was conducted using the best ML model obtained after the training.

Laboratory Experimental Validation

The surgeon provided a total of 11 videos in .M4V format for the laboratory experimental validation. The medical staff collected and labelled these videos during routine clinical practice. To protect the privacy of patients, an anonymisation procedure was applied which removed any metadata from the original files. The videos captured the portions of the intestine where the anastomosis was being performed, and were acquired directly from the endoscope during surgery. The ICG technology was used, and when the ICG was injected, the portion that is well perfused became fluorescent. Figure 4.8 shows an example of frames extracted from the dataset, illustrating the intraoperative use of ICG technology.

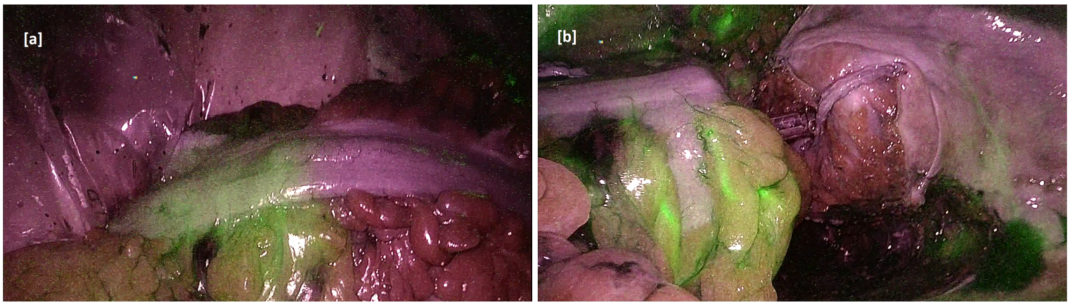

Fig. 4.8 Use of ICG technology during surgery to assess the vascular perfusion of the intestinal segment and to guide the anastomosis procedure. Fig. 4.8-a shows the fluorescence angiography, which allows visualization of the well-perfused portion of the intestine. Once this segment is identified, the anastomosis is performed using the residual colon, as shown in Fig. 4.8-b. Image taken from [7].

In this context, it is noteworthy that 4.8-a showcases fluorescence angiography, which effectively demonstrates the vascular perfusion of the intestinal segment that delimits the section point. On the other hand, 4.8-b depicts the surgical procedure for anastomosis using the residual colon. The fluorescence angiography was carried out using a laparoscopic system, namely the Olympus OTV-S300, which features a light source (Olympus CLV-S200 IR) capable of utilizing visible as well as near-infrared light. The performance of the developed NNs was validated using 11 videos from the dataset. Different frames were extracted from each video, and frames containing ROIs with clear evidence of ICG were selected as well as more challenging ones to train the model properly in assessing the quality of perfusion. From each ROI, 20 feature vectors were obtained, resulting in a dataset size of 470 frames. The overall process of feature extraction is illustrated in Fig.4.9.

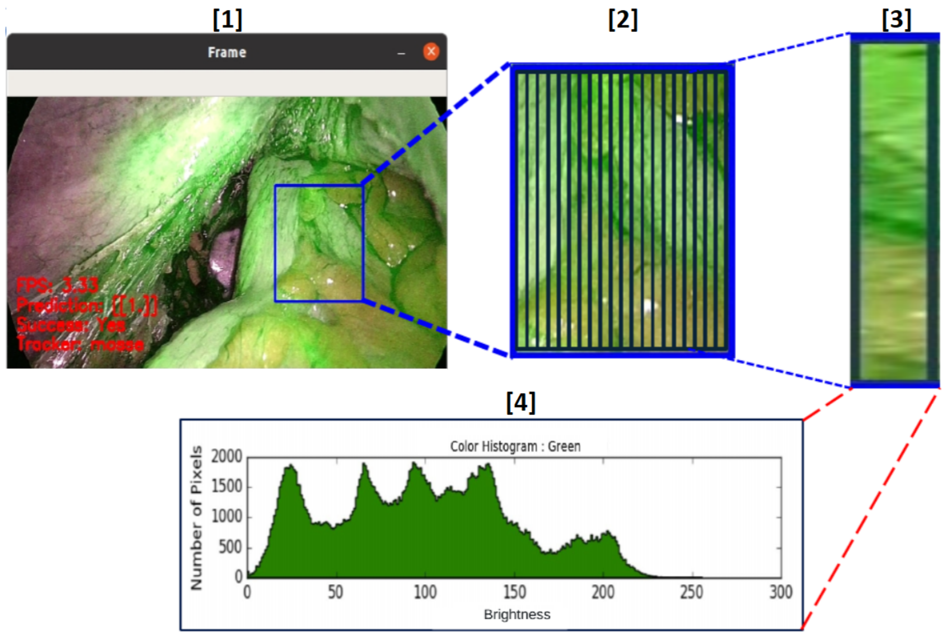

Fig. 4.9 Details of the features extraction: in Step 1 of the feature extraction process, the ROI is selected from the frame. In Step 2, the ROI is divided into 20 equal slices. In Step 3, for each slice, the histogram of the green band of the RGB color space is evaluated. Finally, in Step 4, the amount of green in each histogram is evaluated, and this information is used to construct the feature vector that is sent to the machine learning (ML) classifier. Specifically, the amount of green in each histogram is normalized and represented as a value between 0 and 1, and all 20 values are concatenated into a single feature vector. Image taken from [7].

Step 1 involves displaying the frame of interest. Following this, as previously described, the user selects the ROI which is subsequently divided into 20 slices in Step 2. For each slice obtained in Step 3, the histogram of the green channel is computed to show the frequency distribution of the green levels. Step 4 involves evaluating the area under each histogram as an element of the feature vector. These extracted features are then fed into the classifiers discussed earlier. Table 4.2 provides a summary of the chosen hyperparameters for each classifier and their corresponding accuracy in terms of means and $1-\sigma$ repeatability.

Network	**Kernel**	**Neurons L1**	**Neurons L2**	**Activation function**	**Accuracy (%)**
SVM	Linear	-	-	-	54.5 ± 15.6
SVM	Gaussian	-	-	-	45.4 ± 23.8
FFNN	-	**20**	-	**ReLU**	$\mathbf{99.9 \pm 1.9}$
FFNN	-	80	-	Tanh	54.1 ± 28.6
FFNN	-	100	-	Sigmoid	86.0 ± 7.6
FFNN	-	90	90	ReLU	85.2 ± 15.0
FFNN	-	50	50	Tanh	69.9 ± 22.9
FFNN	-	90	70	Sigmoid	68.5 ± 24.2

Table 4.2 Performance as a function of the chosen set of hyperparameters for all the tested networks. Table taken from [7].

According to what reported in [7], *"the experimental results indicate that the one-hidden layer neural network (NN) with 20 neurons and Rectified Linear Unit (ReLU) as the activation function achieves the best performance, with an average accuracy of* 99.9% *and a* $1-\sigma$ *repeatability of* 1.9%. *This model outperforms the Sigmoidal and Tanh activation functions, even with more neurons in the hidden layer"*. The performance of Support Vector Machine (SVM) and two-hidden layer NN is found to be worse than that of the one-hidden layer network. The best accuracy achieved with SVM is 54.5%, while the two-hidden layer NN reaches the best accuracy of 85.2%. Since the one-hidden layer NN achieved the best results, additional tests were conducted to fine-tune the number of neurons. Table 4.3 and Fig.4.10 summarize the performance details for the one-hidden layer networks as both the number of neurons and the activation function are varied. The best model is highlighted in bold.

Neurons	Tanh accuracy (%)	Sigmoid accuracy (%)	ReLU accuracy (%)
10	47.9 ± 23.7	74.2 ± 10.6	93.7 ± 14.8
20	42.1 ± 25.3	75.6 ± 14.7	$\mathbf{99.9 \pm 1.9}$
30	51.1 ± 28.1	79.5 ± 11.5	98.0 ± 3.0
40	45.6 ± 39.5	79.4 ± 8.5	97.4 ± 5.2
50	53.2 ± 36.1	84.6 ± 9.2	97.4 ± 3.2
60	52.1 ± 35.9	85.8 ± 5.5	98.6 ± 2.8
70	49.1 ± 33.2	81.1 ± 10.7	99.3 ± 2.0
80	54.1 ± 28.6	83.7 ± 9.8	99.4 ± 1.9
90	50.9 ± 34.2	82.6 ± 6.4	98.7 ± 2.7
100	53.9 ± 30.2	86.0 ± 7.6	99.7 ± 2.6

Table 4.3 Performance of FFNN with one hidden layer and Tanh, Sigmoid, and ReLU as activation functions with different neurons. Table taken from [7].

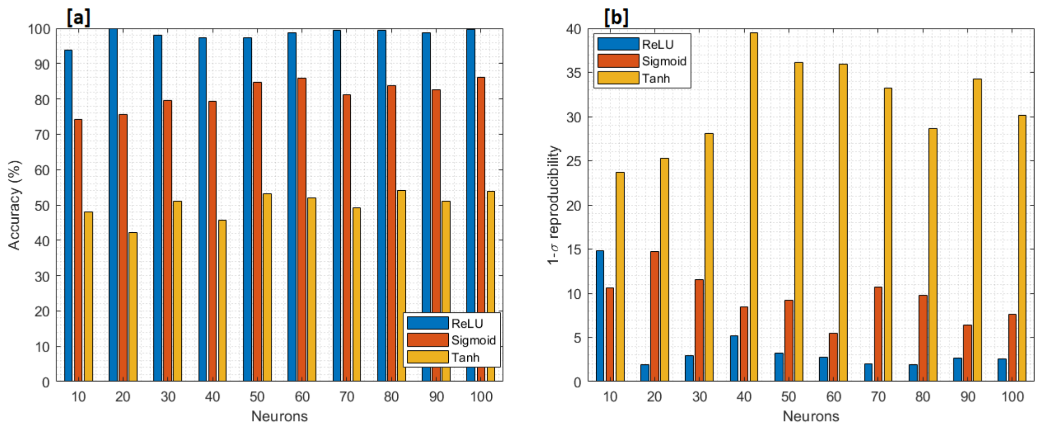

Fig. 4.10 Comparison of (a) accuracy, and (b) 1-σ repeatability for the three activation functions used with different neurons: Tanh (orange), Sigmoid (red), Rectifier Linear Unit (blue). Image taken form [7].

The experimental results demonstrate that the best performance is consistently achieved using ReLU as the activation function, and the optimal number of neurons is 20. To validate the statistical significance of the differences between the mean accuracies obtained with the three different activation functions (Tanh, Sigmoid, and ReLU), One-Way ANOVA and Fischer tests were performed with a chosen null hypothesis (H_0) that assumed the groups belonged to the same population at a significance level of $\alpha = 1.0\%$. The results indicated that the null hypothesis should be rejected with a P-value of 0.0%. Subsequently, a paired t-test was conducted with a significance level of $\alpha = 1.0\%$ to determine which group was different from the others (upon verification of normality of data by means of a χ^2 test). In all three tests, the null hypothesis of identical groups was rejected. The statistical analysis was performed using the online tool "Statistic Kingdom" [208]. Table 4.3 summarizes the detailed performance of the one-hidden layer networks with varying numbers of neurons and activation functions, with the best-performing model highlighted in bold. Further details are reported in Table 4.4.

Test	H_0	α (%)	**P-value (%)**	**Decision**
Fischer test Tanh-Sigmoid-ReLU	Same distribution	1.0	0.0	Reject
t-test Tanh-Sigmoid	Same distribution	1.0	$1.8 \cdot 10^{-9}$	Reject
t-test Tanh-ReLU	Same distribution	1.0	$3.5 \cdot 10^{-9}$	Reject
t-test ReLU-Sigmoid	Same distribution	1.0	$1.0 \cdot 10^{-5}$	Reject

Table 4.4 Details about statistical analysis of the three groups. Table taken from [7].

The statistical validation tests confirmed that the accuracy results obtained using ReLU activation function and 20 neurons are statistically significant, as they showed a significant difference when compared to the other models with different activation functions. Therefore, this specific model was chosen for the classification stage of the proposed system and implemented in the prototype version.

For illustrative purposes, the outcomes of the proposed algorithm when applied to frames of the dataset depicting good and bad perfusion are presented in Fig. 4.11.

For each frame in the dataset, the corresponding ROI is highlighted. Specifically, Fig. 4.11-a and Fig. 4.11-d have ROIs classified as having good perfusion (i.e., a high amount of green) and a prediction output of 1. Conversely, Fig. 4.11-b and Fig. 4.11-c have prediction outputs equal to 0, as the ROIs were considered to have poor perfusion due to a low amount of green or an uneven distribution of green in the selected ROI. In all cases, the accuracy of the classification was confirmed by the surgeons.

Operating Room Experimental Validation

After the offline validation, the proposed algorithm was further tested using the Olympus Visera Elite II endoscope at the University Hospital *Federico II* in Naples,

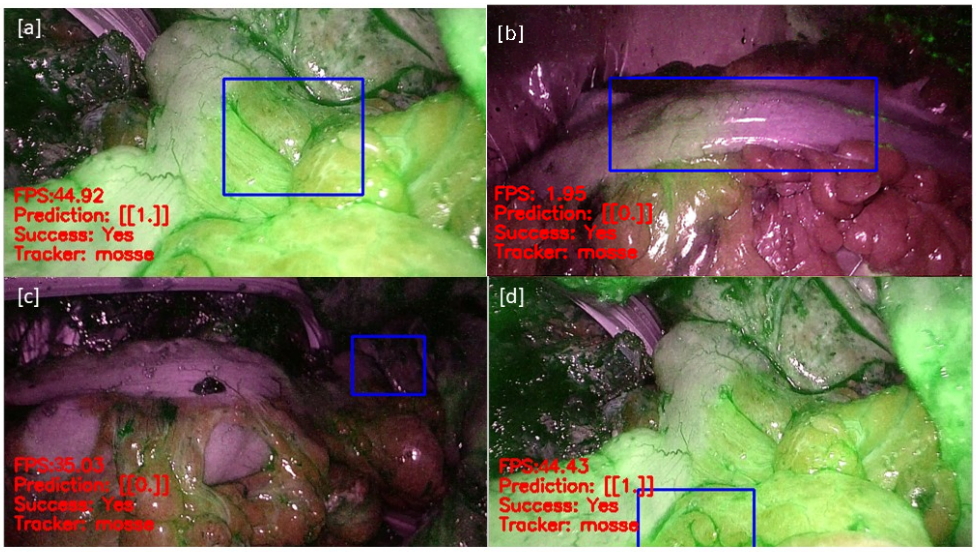

Fig. 4.11 Four frames from the dataset are presented in Fig. 5, with their respective ROIs. Figures 4.11-a and 4.11-d have ROIs indicating adequate perfusion, with a high amount of green and a corresponding prediction value of 1. On the other hand, 4.11-b and 4.11-c have prediction values of 0, indicating inadequately perfused ROIs, with low amounts of green and/or non-uniform ICG diffusion. Image taken from [7].

Italy, to verify the possibility of interfacing the system with medical equipment and to assess real-time interfacing with the endoscope. The Olympus Visera Elite II is a general surgery imaging platform that links the OR to other devices and facilities around the hospital, and an S-video to USB adapter was used to connect the endoscope to a PC running Windows 10 and Python 2.7. The endoscope captured video was transmitted in real-time to an elaboration unit located outside the OR, and surgeons who were not part of the operation were asked to select the ROIs, although this workflow could also be conducted by the main surgical team inside the OR.

The system was able to process at least 30 frames per second from the video source, which was considered acceptable for the surgeons to select the ROI and use the system. Furthermore, the output provided by the algorithm could effectively assist surgeons in making decisions even in low brightness situations. In Fig. 4.12, the output of the system working under three different levels of green brightness is presented. This also demonstrates that the proposed system is capable of accurately classifying the frame regardless of the level of green brightness.

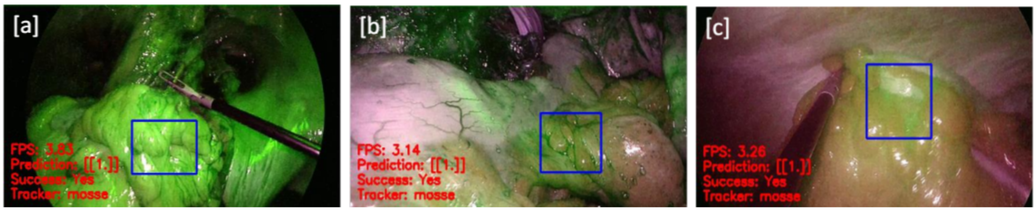

Fig. 4.12 For the online validation, frames with different brightness levels were acquired directly from the endoscope. Fig. 4.12-a shows a frame with high brightness, Fig. 4.12-b with medium brightness, and Fig. 4.12-c with low brightness. Despite the different brightness levels, the proposed algorithm was able to provide real-time predictions, demonstrating its robustness and effectiveness in various scenarios, including low brightness scenarios. Image taken from [7].

4.3 Conclusions

This Chapter introduced the development of two decision-support system in the framework of *Health 4.0*.

The first system leverages low-cost infrared thermography instrumentation to evaluate the effectiveness of scoliosis braces in real time. Such a system exploits the thermoelastic effect, establishing a correlation between changes in brace pressure and temperature variations on the patient's backbone. An experimental campaign was conducted at an accredited orthopedic center involving 21 juvenile and adolescent patients. The campaign simulated real operational conditions and acquired 36 thermal images, each of which was labeled by the medical team. A dedicated algorithm incorporating artificial intelligence techniques was implemented, and rigorous validation strategies were employed to ensure generalization to unseen data. The experimental results demonstrated a classification accuracy slightly below 70 %, which is promising given the use of low-cost instrumentation and the intentionally non-ideal experimental conditions. Future endeavors will focus on improving performance through the utilization of advanced instrumentation and algorithms, aiming to enhance the reliability of this decision-support system for orthopedic centers.

Another system described in this Chapter is a decision-support system designed to assist surgeons during laparoscopic colorectal surgery. Such a system automatically evaluates the quality of perfusion as either "adequate" or "inadequate" following an injection of indocyanine green dye. Multiple classifier models were tested on a dataset comprising videos of various anastomoses performed at the Federico II Hospital. Among the models, the one-hidden-layer neural network with 20 neurons and a Rectified Linear Unit (ReLU) activation function exhibited the best performance. It achieved a prediction accuracy of 99.9 % with a 1-σ repeatability of 1.9 %. These results were statistically validated through ANOVA, Fischer, and paired-t tests, leading to the selection of this model for system implementation. Successful validation was also achieved in terms of interfacing with the actual equipment used at the University Hospital Federico II in Naples, Italy. The proposed system serves as a valuable decision-support tool for surgeons, particularly in situations of uncertainty where the adequacy of blood perfusion is uncertain due to the presence of unclear indocyanine green dye. Future work will address the current research limitations by introducing more levels between adequate and inadequate perfusion, thereby enhancing the resolution of assessments and prediction accuracy. Additionally, efforts will focus on automatically selecting Regions of Interest (ROIs) and expanding the dataset to include cases where blood perfusion is impaired by underlying pathologies such as atherosclerosis. These scenarios pose challenges for both the classifier and the surgeon in accurately assessing the adequacy of perfusion.

Chapter 5

Conclusions

This doctoral work focuses on the development of assistive solutions in Healthcare by leveraging some of the emerging *4.0* enabling technologies, then contributing to the digital transformation of Healthcare.

In particular, Chapter 2 details the development of Brain-Computer Interfaces (BCIs) utilizing the Steady-State Visually Evoked (SSVEP) paradigm and Augmented Reality (AR) technology. Following an extensive overview of the concepts essential for constructing an SSVEP-based BCI, the chapter presents various systems designed and developed over the years, systematically comparing them to underscore their contributions in enhancing system accuracy for real-world scenarios. Notably, a metrological approach was employed to assess system performance across diverse subjects. Finally, the chapter presents two pertinent case studies, illustrating the practical application of the proposed system (i) during surgical procedures and (ii) within the context of children's rehabilitation. Overall, the obtained results in terms of SSVEP recognition accuracy, information transmission efficiency, and ergonomic qualities show promise for future applications of this technology in real-world settings beyond laboratory environments.

Chapter 3 delves into the implementation of an Augmented Reality (AR) platform for health monitoring in the Operating Room (OR). This platform was designed to be worn by nurses, anesthetists, or surgeons, offering them a comprehensive stream of real-time information through an AR headset. This information encompasses the patient's electronic clinical record, vital signs collected from a pulmonary ventilator and an intensive care monitor, as well as video streaming from a laparoscopic camera.

By instantly providing this data and making it easily accessible, the platform streamlines efficient and prompt monitoring for OR personnel. The development of the AR platform concentrated on meeting the rigorous criteria of the healthcare domain, especially concerning communication accuracy and response time. Experimental outcomes corroborated that the platform achieved exceptional communication accuracy, surpassing 97 %, while concurrently maintaining rapid response times in the millisecond range. These results showcase the platform's capability to satisfy the exacting needs of the healthcare sector. Usability tests, conducted through the administration of System Usability Scale (SUS) questionnaires, further validated the AR monitoring platform's suitability for extended use. Feedback from OR staff underscored the platform's user-friendly nature, ergonomic design, and the absence of motion sickness effects. The array of data selection options, including vocal commands, gestures, and gaze pointers, received particular commendation from operators. In conclusion, the proposed integrated AR platform has demonstrated its worth as a dependable and supportive tool for OR personnel during the vigilant monitoring of patients' health in complex surgical procedures. By offering real-time access to crucial information, the platform enhances the efficiency and effectiveness of patient care within the OR.

Finally, Chapter 4 introduces the development of two decision-support systems. The first system utilizes low-cost infrared thermography instrumentation to assess the real-time effectiveness of scoliosis braces. This system capitalizes on the thermoelastic effect, establishing a correlation between changes in brace pressure and temperature fluctuations on the patient's spine. An experimental campaign was conducted at an accredited orthopedic center, involving 21 juvenile and adolescent patients. The campaign simulated real operational conditions, capturing 36 thermal images, each labeled by the medical team. An algorithm incorporating artificial intelligence techniques was specifically designed, with rigorous validation strategies to ensure applicability to unseen data. The experimental outcomes demonstrated a classification accuracy of just below 70 %, promising considering the use of affordable instrumentation and intentionally non-optimal experimental conditions.
Another system described in this chapter is a decision-support system tailored to aid surgeons during laparoscopic colorectal surgery. This system automatically evaluates the quality of perfusion as either *adequate* or *inadequate* following an indocyanine green dye injection. Multiple classifier models were evaluated on a dataset comprising videos of various anastomoses performed at the Federico II Hospital. Among

the models, the one-hidden-layer neural network with 20 neurons and a Rectified Linear Unit (ReLU) activation function exhibited better performance. It achieved a prediction accuracy of 99.9 % with a 1-σ repeatability of 1.9 %. These results underwent statistical validation via ANOVA, Fischer, and paired-t tests, leading to the selection of this model for system implementation. Successful validation was also accomplished in terms of interfacing with the actual equipment used at the University Hospital Federico II in Naples, Italy. The proposed system serves as a valuable decision-support tool for surgeons, particularly in instances of uncertainty where the adequacy of blood perfusion is uncertain due to the unclear presence of indocyanine green dye.

For each of the described systems, a metrological approach was adopted to characterize their performance and ensure a defined confidence interval. This was carried out following the guidelines of the Guide to the Expression of Uncertainty in Measurement and its Supplement One, based on the Monte Carlo Method. In this manner, all developed systems are contributing to an enhancement in the services provided by the healthcare system, thus fully embracing the 4.0 digital transformation.

References

[1] Industrial Revolutions. https://upload.wikimedia.org/wikipedia/commons/c/c8/Industry_4.0.png. Accessed: 2023-02-27.

[2] Angela T Chan, Juan C Quiroz, Sergiu Dascalu, and Frederick C Harris. An overview of brain computer interfaces. In *Proc. 30th Int. Conf. on Computers and Their Applications*, 2015.

[3] Andrea Apicella, Pasquale Arpaia, Egidio De Benedetto, Nicola Donato, Luigi Duraccio, Salvatore Giugliano, and Roberto Prevete. Employment of domain adaptation techniques in ssvep-based brain-computer interfaces. *IEEE Access*, 2023.

[4] Andrea Apicella, Pasquale Arpaia, Egidio De Benedetto, Nicola Donato, Luigi Duraccio, Salvatore Giugliano, and Roberto Prevete. Enhancement of ssveps classification in bci-based wearable instrumentation through machine learning techniques. *IEEE Sensors Journal*, 22(9):9087–9094, 2022.

[5] Pasquale Arpaia, Egidio De Benedetto, Lucio De Paolis, Giovanni D'Errico, Nicola Donato, and Luigi Duraccio. Performance and usability evaluation of an extended reality platform to monitor patient's health during surgical procedures. *Sensors*, 22(10):3908, 2022.

[6] Ameersing Luximon, Huang Chao, Ravindra S Goonetilleke, and Yan Luximon. Theory and applications of infrared and thermal image analysis in ergonomics research. *Frontiers in Computer Science*, 4:990290, 2022.

[7] Pasquale Arpaia, Umberto Bracale, Francesco Corcione, Egidio De Benedetto, Alessandro Di Bernardo, Vincenzo Di Capua, Luigi Duraccio, Roberto Peltrini, and Roberto Prevete. Assessment of blood perfusion quality in laparoscopic colorectal surgery by means of machine learning. *Scientific Reports*, 12(1):14682, 2022.

[8] Ashwani Sharma and Bikram Jit Singh. Evolution of industrial revolutions: A review. *International Journal of Innovative Technology and Exploring Engineering*, 9(11):66–73, 2020.

[9] Phyllis M Deane. *The first industrial revolution*. Cambridge University Press, 1979.

[10] Joel Mokyr and Robert H Strotz. The second industrial revolution, 1870-1914. *Storia dell'economia Mondiale*, 21945(1), 1998.

[11] Jeremy Greenwood. *The third industrial revolution: Technology, productivity, and income inequality*. Number 435. American Enterprise Institute, 1997.

[12] Min Xu, Jeanne M David, Suk Hi Kim, et al. The fourth industrial revolution: Opportunities and challenges. *International journal of financial research*, 9(2):90–95, 2018.

[13] Arianna Martinelli, Andrea Mina, and Massimo Moggi. The enabling technologies of industry 4.0: examining the seeds of the fourth industrial revolution. *Industrial and Corporate Change*, 30(1):161–188, 2021.

[14] Yingfeng Zhang, Ting Qu, Oscar K Ho, and George Q Huang. Agent-based smart gateway for rfid-enabled real-time wireless manufacturing. *International Journal of Production Research*, 49(5):1337–1352, 2011.

[15] Sunil Chopra and ManMohan S Sodhi. Looking for the bang from the rfid buck. *Supply Chain Management Review*, pages 34–41, 2007.

[16] Samia Benrachi-Maassam. Lessons learned from early m2m deployments. *M2M Communications: A Systems Approach*, pages 37–53, 2012.

[17] Dong-hyu Kim, Heejin Lee, and Jooyoung Kwak. Standards as a driving force that influences emerging technological trajectories in the converging world of the internet and things: An investigation of the m2m/iot patent network. *Research Policy*, 46(7):1234–1254, 2017.

[18] IoT Market Analysis: Sizing the Opportunity. http://iot-analytics.com/wp/wp-content/uploads/2015/03/2015-March-Whitepaper-IoT-Market-analysis-Sizing-the-opportunity.pdf. Accessed: 2023-02-27.

[19] Nils J Nilsson, Yves Hilpisch, Mariya Yao, Adelyn Zhou, Marlene Jia, Bart Baesen, Veronique Van Vlasselaer, and Wouter Verbeke. The quest for ai-a history of ideas and achievements. *Erişim adresi: http://ai. standford. edu/˜ nilsson/(Özgün eser 2009 tarihlidir)*, 2010.

[20] Jacques Bughin, Jeongmin Seong, James Manyika, Michael Chui, and Raoul Joshi. Notes from the ai frontier: Modeling the impact of ai on the world economy. *McKinsey Global Institute*, 4, 2018.

[21] Jay Lee, Hossein Davari, Jaskaran Singh, and Vibhor Pandhare. Industrial artificial intelligence for industry 4.0-based manufacturing systems. *Manufacturing letters*, 18:20–23, 2018.

[22] Jacques Bughin, Eric Hazan, Sree Ramaswamy, Michael Chui, Tera Allas, Peter Dahlstrom, Nicolaus Henke, and Monica Trench. Artificial intelligence: the next digital frontier? 2017.

[23] Joachim Scholz and Andrew N Smith. Augmented reality: Designing immersive experiences that maximize consumer engagement. *Business Horizons*, 59(2):149–161, 2016.

[24] Pasquale Arpaia, Egidio De Benedetto, Concetta Anna Dodaro, Luigi Duraccio, and Giuseppe Servillo. Metrology-based design of a wearable augmented reality system for monitoring patient's vitals in real time. *IEEE Sensors Journal*, 21(9):11176–11183, 2021.

[25] Pasquale Arpaia, Egidio De Benedetto, and Luigi Duraccio. Design, implementation, and metrological characterization of a wearable, integrated ar-bci hands-free system for health 4.0 monitoring. *Measurement*, 177:109280, 2021.

[26] Amit Kishor and Chinmay Chakraborty. Artificial intelligence and internet of things based healthcare 4.0 monitoring system. *Wireless personal communications*, 127(2):1615–1631, 2022.

[27] Ada TL Ng and PC Tam. Current status of robot-assisted surgery. *Hong Kong medical journal*, 2014.

[28] Lucio Tommaso De Paolis and Giovanni Aloisio. Augmented reality in minimally invasive surgery. *Advances in biomedical sensing, measurements, instrumentation and systems*, pages 305–320, 2010.

[29] Lucio Tommaso De Paolis and Valerio De Luca. Augmented visualization with depth perception cues to improve the surgeon's performance in minimally invasive surgery. *Medical & biological engineering & computing*, 57(5):995–1013, 2019.

[30] Pasquale Arpaia, Luigi Duraccio, Nicola Moccaldi, and Silvia Rossi. Wearable brain-computer interface instrumentation for robot-based rehabilitation by augmented reality. *IEEE Transactions on Instrumentation and Measurement*, 69(9), 2020.

[31] Pasquale Arpaia, Egidio De Benedetto, Lucio De Paolis, Giovanni D'Errico, Nicola Donato, and Luigi Duraccio. Performance enhancement of wearable instrumentation for ar-based ssvep bci. *Measurement*, 196:111188, 2022.

[32] Leopoldo Angrisani, Pasquale Arpaia, Egidio De Benedetto, Luigi Duraccio, Fabrizio Lo Regio, and Annarita Tedesco. Wearable brain-computer interfaces based on steady-state visually evoked potentials and augmented reality: a review. *IEEE Sensors Journal*, pages 1–1, 2023.

[33] Jigna J Hathaliya and Sudeep Tanwar. An exhaustive survey on security and privacy issues in healthcare 4.0. *Computer Communications*, 153:311–335, 2020.

[34] Jonathan R Wolpaw, Niels Birbaumer, William J Heetderks, Dennis J McFarland, P Hunter Peckham, Gerwin Schalk, Emanuel Donchin, Louis A Quatrano, Charles J Robinson, Theresa M Vaughan, et al. Brain-computer interface technology: a review of the first international meeting. *IEEE transactions on rehabilitation engineering*, 8(2):164–173, 2000.

[35] Han Yuan and Bin He. Brain–computer interfaces using sensorimotor rhythms: current state and future perspectives. *IEEE Transactions on Biomedical Engineering*, 61(5):1425–1435, 2014.

[36] Matthew D Golub, Steven M Chase, Aaron P Batista, and M Yu Byron. Brain–computer interfaces for dissecting cognitive processes underlying sensorimotor control. *Current opinion in neurobiology*, 37:53–58, 2016.

[37] Han-Jeong Hwang, Jeong-Hwan Lim, Young-Jin Jung, Han Choi, Sang Woo Lee, and Chang-Hwan Im. Development of an ssvep-based bci spelling system adopting a qwerty-style led keyboard. *Journal of neuroscience methods*, 208(1):59–65, 2012.

[38] Robert Leeb, Luca Tonin, Martin Rohm, Lorenzo Desideri, Tom Carlson, and Jose del R Millan. Towards independence: a bci telepresence robot for people with severe motor disabilities. *Proceedings of the IEEE*, 103(6):969–982, 2015.

[39] Gert Pfurtscheller, Gernot R Müller-Putz, Jörg Pfurtscheller, and Rüdiger Rupp. Eeg-based asynchronous bci controls functional electrical stimulation in a tetraplegic patient. *EURASIP Journal on Advances in Signal Processing*, 2005:1–4, 2005.

[40] Jonathan R Wolpaw, Niels Birbaumer, Dennis J McFarland, Gert Pfurtscheller, and Theresa M Vaughan. Brain–computer interfaces for communication and control. *Clinical neurophysiology*, 113(6):767–791, 2002.

[41] Bernhard Graimann, Brendan Allison, and Axel Gräser. New applications for non-invasive brain-computer interfaces and the need for engaging training environments. In *Proceedings of the International Conference on Advances in Computer Entertainment*, pages 25–28, 2007.

[42] Dean J Krusienski, Moritz Grosse-Wentrup, Ferran Galán, Damien Coyle, Kai J Miller, Elliott Forney, and Charles W Anderson. Critical issues in state-of-the-art brain–computer interface signal processing. *Journal of neural engineering*, 8(2):025002, 2011.

[43] Thorsten O Zander, Christian Kothe, Sabine Jatzev, and Matti Gaertner. Enhancing human-computer interaction with input from active and passive brain-computer interfaces. *Brain-Computer Interfaces: Applying our Minds to Human-Computer Interaction*, pages 181–199, 2010.

[44] Pasquale Arpaia, Antonio Esposito, Angela Natalizio, and Marco Parvis. How to successfully classify eeg in motor imagery bci: a metrological analysis of the state of the art. *Journal of Neural Engineering*, 19(3):031002, 2022.

[45] Yu Pei, Tingyu Sheng, Zhiguo Luo, Liang Xie, Weiguo Li, Ye Yan, and Erwei Yin. A tensor-based frequency features combination method for brain–computer interfaces. In *Cognitive Systems and Information Processing: 6th International Conference, ICCSIP 2021, Suzhou, China, November 20–21, 2021, Revised Selected Papers 6*, pages 511–526. Springer, 2022.

[46] Yu Pei, Zhiguo Luo, Hongyu Zhao, Dengke Xu, Weiguo Li, Ye Yan, Huijiong Yan, Liang Xie, Minpeng Xu, and Erwei Yin. A tensor-based frequency features combination method for brain–computer interfaces. *IEEE Transactions on Neural Systems and Rehabilitation Engineering*, 30:465–475, 2021.

[47] Yu Pei, Zhiguo Luo, Ye Yan, Huijiong Yan, Jing Jiang, Weiguo Li, Liang Xie, and Erwei Yin. Data augmentation: using channel-level recombination to improve classification performance for motor imagery eeg. *Frontiers in Human Neuroscience*, 15:645952, 2021.

[48] Jing Jiang, Chunhui Wang, Jinghan Wu, Wei Qin, Minpeng Xu, and Erwei Yin. Temporal combination pattern optimization based on feature selection method for motor imagery bcis. *Frontiers in Human Neuroscience*, 14:231, 2020.

[49] Andrea Apicella, Pasquale Arpaia, Mirco Frosolone, Giovanni Improta, Nicola Moccaldi, and Andrea Pollastro. Eeg-based measurement system for monitoring student engagement in learning 4.0. *Scientific Reports*, 12(1):5857, 2022.

[50] Javier Marín-Morales, Carmen Llinares, Jaime Guixeres, and Mariano Alcañiz. Emotion recognition in immersive virtual reality: From statistics to affective computing. *Sensors*, 20(18):5163, 2020.

[51] Bettina C Schwab, Daisuke Kase, Andrew Zimnik, Robert Rosenbaum, Marcello G Codianni, Jonathan E Rubin, and Robert S Turner. Neural activity during a simple reaching task in macaques is counter to gating and rebound in basal ganglia–thalamic communication. *PLoS biology*, 18(10):e3000829, 2020.

[52] Isaac Chen and Forshing Lui. Neuroanatomy, neuron action potential. 2019.

[53] Bin He, Bryan Baxter, Bradley J Edelman, Christopher C Cline, and W Ye Wenjing. Noninvasive brain-computer interfaces based on sensorimotor rhythms. *Proceedings of the IEEE*, 103(6):907–925, 2015.

[54] Johannes Höhne and Michael Tangermann. How stimulation speed affects event-related potentials and bci performance. In *2012 annual international conference of the IEEE engineering in medicine and biology society*, pages 1802–1805. IEEE, 2012.

[55] François-Benoît Vialatte, Monique Maurice, Justin Dauwels, and Andrzej Cichocki. Steady-state visually evoked potentials: focus on essential paradigms and future perspectives. *Progress in neurobiology*, 90(4):418–438, 2010.

[56] Reza Abiri, Soheil Borhani, Eric W Sellers, Yang Jiang, and Xiaopeng Zhao. A comprehensive review of eeg-based brain–computer interface paradigms. *Journal of neural engineering*, 16(1):011001, 2019.

[57] Ming Cheng, Xiaorong Gao, Shangkai Gao, and Dingfeng Xu. Design and implementation of a brain-computer interface with high transfer rates. *IEEE transactions on biomedical engineering*, 49(10):1181–1186, 2002.

[58] Yuanqing Li, Fangyi Wang, Yongbin Chen, Andrzej Cichocki, and Terrence Sejnowski. The effects of audiovisual inputs on solving the cocktail party problem in the human brain: An fmri study. *Cerebral Cortex*, 28(10):3623–3637, 2018.

[59] Jürgen Mellinger, Gerwin Schalk, Christoph Braun, Hubert Preissl, Wolfgang Rosenstiel, Niels Birbaumer, and Andrea Kübler. An meg-based brain–computer interface (bci). *Neuroimage*, 36(3):581–593, 2007.

[60] Jaeyoung Shin, Jinuk Kwon, Jongkwan Choi, and Chang-Hwan Im. Performance enhancement of a brain-computer interface using high-density multi-distance nirs. *Scientific reports*, 7(1):1–10, 2017.

[61] Luis Carretié. Exogenous (automatic) attention to emotional stimuli: a review. *Cognitive, Affective, & Behavioral Neuroscience*, 14(4):1228–1258, 2014.

[62] Yijun Wang, Ruiping Wang, Xiaorong Gao, Bo Hong, and Shangkai Gao. A practical vep-based brain-computer interface. *IEEE Transactions on neural systems and rehabilitation engineering*, 14(2):234–240, 2006.

[63] Chuan Jia, Xiaorong Gao, Bo Hong, and Shangkai Gao. Frequency and phase mixed coding in SSVEP-based brain–computer interface. *IEEE Transactions on Biomedical Engineering*, 58(1):200–206, 2010.

[64] Gernot R Müller-Putz, Reinhold Scherer, Christian Brauneis, and Gert Pfurtscheller. Steady-state visual evoked potential (SSVEP)-based communication: impact of harmonic frequency components. *Journal of neural engineering*, 2(4):123, 2005.

[65] Leopoldo Angrisani, Egidio De Benedetto, Luigi Duraccio, Fabrizio Lo Regio, Roberto Ruggiero, and Annarita Tedesco. Infrared thermography for real-time assessment of the effectiveness of scoliosis braces. *Sensors*, 23(19):8037, 2023.

[66] Hao-Teng Hsu, Kuo-Kai Shyu, Chuan-Chih Hsu, Lung-Hao Lee, and Po-Lei Lee. Phase-approaching stimulation sequence for ssvep-based bci: a practical use in vr/ar hmd. *IEEE Transactions on Neural Systems and Rehabilitation Engineering*, 29:2754–2764, 2021.

[67] Leopoldo Angrisani, Pasquale Arpaia, Antonio Esposito, and Nicola Moccaldi. A wearable brain-computer interface instrument for augmented reality-based inspection in industry 4.0. *IEEE Transactions on Instrumentation and Measurement*, 2019.

[68] Hakim Si-Mohammed, Jimmy Petit, Camille Jeunet, Ferran Argelaguet, Fabien Spindler, Andéol Evain, Nicolas Roussel, Géry Casiez, and Anatole Lécuyer. Towards bci-based interfaces for augmented reality: feasibility, design and evaluation. *IEEE transactions on visualization and computer graphics*, 26(3):1608–1621, 2018.

[69] A. Tedesco, D. Dallet, and P. Arpaia. Augmented reality (AR) and brain-computer interface (BCI): Two enabling technologies for empowering the fruition of sensor data in the 4.0 era. In *Proceedings of the AISEM 2020 Regional Workshop*, volume 753, pages 85–91, 2021.

[70] Jin Han, Minpeng Xu, Xiaolin Xiao, Weibo Yi, Tzyy-Ping Jung, and Dong Ming. A high-speed hybrid brain-computer interface with more than 200 targets. *Journal of Neural Engineering*, 2023.

[71] M Teresa Medina-Juliá, Álvaro Fernández-Rodríguez, Francisco Velasco-Álvarez, and Ricardo Ron-Angevin. P300-based brain-computer interface speller: usability evaluation of three speller sizes by severely motor-disabled patients. *Frontiers in Human Neuroscience*, 14:583358, 2020.

[72] Yijun Wang, Xiaogang Chen, Xiaorong Gao, and Shangkai Gao. A benchmark dataset for SSVEP-based brain–computer interfaces. *IEEE Trans. Neural Syst. Rehabil. Eng.*, 25(10):1746–1752, 2016.

[73] Pasquale Arpaia, Carmela Bravaccio, Giuseppina Corrado, Luigi Duraccio, Nicola Moccaldi, and Silvia Rossi. Robotic autism rehabilitation by wearable brain-computer interface and augmented reality. In *2020 IEEE International Symposium on Medical Measurements and Applications (MeMeA)*, pages 1–6. IEEE, 2020.

[74] Pasquale Arpaia, Egidio De Benedetto, Nicola Donato, Luigi Duraccio, and Nicola Moccaldi. A wearable ssvep bci for ar-based, real-time monitoring applications. In *2021 IEEE International Symposium on Medical Measurements and Applications (MeMeA)*, pages 1–6. IEEE, 2021.

[75] Pasquale Arpaia, Sabatina Criscuolo, Egidio De Benedetto, Nicola Donato, and Luigi Duraccio. A wearable ar-based bci for robot control in adhd treatment: Preliminary evaluation of adherence to therapy. In *2021 15th International Conference on Advanced Technologies, Systems and Services in Telecommunications (TELSIKS)*, pages 321–324. IEEE, 2021.

[76] Yufeng Ke, Pengxiao Liu, Xingwei An, Xizi Song, and Dong Ming. An online SSVEP-BCI system in an optical see-through augmented reality environment. *Journal of neural engineering*, 17(1):016066, 2020.

[77] Rui Zhang and Dezhong Yao. Ambient brightness issues in ar-bci applications: Phenomenon and solutions. 2022.

[78] Xincan Zhao, Yulin Du, and Rui Zhang. A cnn-based multi-target fast classification method for ar-ssvep. *Computers in biology and medicine*, 141:105042, 2022.

[79] Rui Zhang, Zongxin Xu, Lipeng Zhang, Lijun Cao, Yuxia Hu, Beihan Lu, Li Shi, Dezhong Yao, and Xincan Zhao. The effect of stimulus number on the recognition accuracy and information transfer rate of ssvep–bci in augmented reality. *Journal of Neural Engineering*, 19(3):036010, 2022.

[80] Epson Moverio BT-200 Technical Specifications. https://www.epson.com.au/products/projectoraccessories/Moverio_BT-200_Specs.asp. Accessed: 2023-02-27.

[81] Microsoft Hololens 1 Technical Specifications. https://learn.microsoft.com/it-it/hololens/hololens1-hardware. Accessed: 2023-02-27.

[82] Microsoft Hololens 2 Technical Specifications. https://www.microsoft.com/en-us/hololens/hardware. Accessed: 2023-02-27.

[83] Xiaogang Chen, Yijun Wang, Shangkai Gao, Tzyy-Ping Jung, and Xiaorong Gao. Filter bank canonical correlation analysis for implementing a high-speed ssvep-based brain–computer interface. *Journal of neural engineering*, 12(4):046008, 2015.

[84] Olimex EEG-SMT Website. https://www.olimex.com/Products/EEG/OpenEEG/EEG-SMT/open-source-hardware. Accessed: 2023-07-30.

[85] Hongtao Wang, Fan Yan, Tao Xu, Haojun Yin, Peng Chen, Hongwei Yue, Chuangquan Chen, Hongfei Zhang, Linfeng Xu, Yuebang He, et al. Brain-controlled wheelchair review: From wet electrode to dry electrode, from single modal to hybrid modal, from synchronous to asynchronous. *IEEE Access*, 9:55920–55938, 2021.

[86] Miguel Angel Lopez-Gordo, Daniel Sanchez-Morillo, and F Pelayo Valle. Dry eeg electrodes. *Sensors*, 14(7):12847–12870, 2014.

[87] NeuroCONCISE FlexEEG Technical Specifications. https://www.neuroconcise.co.uk/technology/. Accessed: 2023-05-06.

[88] Gido Hakvoort, Boris Reuderink, and Michel Obbink. Comparison of psda and cca detection methods in a SSVEP-based BCI-system. *Centre for Telematics & Information Technology University of Twente*, 2011.

[89] Xiaogang Chen, Yijun Wang, Masaki Nakanishi, Xiaorong Gao, Tzyy-Ping Jung, and Shangkai Gao. High-speed spelling with a noninvasive brain–computer interface. *Proceedings of the national academy of sciences*, 112(44):E6058–E6067, 2015.

[90] Zhonglin Lin, Changshui Zhang, Wei Wu, and Xiaorong Gao. Frequency recognition based on canonical correlation analysis for ssvep-based BCIs. *IEEE transactions on biomedical engineering*, 53(12):2610–2614, 2006.

[91] Pasquale Arpaia, Egidio De Benedetto, Lucio De Paolis, Giovanni D'Errico, Nicola Donato, and Luigi Duraccio. Highly wearable ssvep-based bci: Performance comparison of augmented reality solutions for the flickering stimuli rendering. *Measurement: Sensors*, 18:100305, 2021.

[92] IEC BIPM, ILAC IFCC, IUPAC ISO, and OIML IUPAP. Guide to the expression of uncertainty in measurement jcgm 100: 2008. *JCGM*, 101:2008, 2008.

[93] JCGM 101:2008 Evaluation of Measurement Data - Guide to the Expression of Uncertainty in Measurement, 2008. Online, accessed: 2023-06-08.

[94] Pasquale Arpaia, Sabatina Criscuolo, Egidio De Benedetto, Nicola Donato, and Luigi Duraccio. Evaluation of the effectiveness of a wearable, ar-based bci for robot control in adhd treatment. In *2022 IEEE International Conference on Metrology for Extended Reality, Artificial Intelligence and Neural Engineering (MetroXRAINE)*, pages 630–634. IEEE, 2022.

[95] A. Alamri, J. Cha, and A. El Saddik. Ar-rehab: An augmented reality framework for poststroke-patient rehabilitation. *IEEE Transactions on Instrumentation and Measurement*, 59(10):2554–2563, 2010.

[96] Benish Fida, Fabrizio Cutolo, Gregorio di Franco, Mauro Ferrari, and Vincenzo Ferrari. Augmented reality in open surgery. *Updates in surgery*, 70(3):389–400, 2018.

[97] Antonio Meola, Fabrizio Cutolo, Marina Carbone, Federico Cagnazzo, Mauro Ferrari, and Vincenzo Ferrari. Augmented reality in neurosurgery: a systematic review. *Neurosurgical review*, 40(4):537–548, 2017.

[98] Giovanni Badiali, Vincenzo Ferrari, Fabrizio Cutolo, Cinzia Freschi, Davide Caramella, Alberto Bianchi, and Claudio Marchetti. Augmented reality as an aid in maxillofacial surgery: validation of a wearable system allowing maxillary repositioning. *Journal of cranio-Maxillofacial surgery*, 42(8):1970–1976, 2014.

[99] S. Condino, N. Montemurro, N. Cattari, R. D'Amato, U. Thomale, V. Ferrari, and F. Cutolo. Evaluation of a wearable ar platform for guiding complex craniotomies in neurosurgery. *Annals of Biomedical Engineering*, 2021.

[100] Enrico Checcucci, Daniele Amparore, Angela Pecoraro, Dario Peretti, Roberta Aimar, F Piramide, G Volpi, P Piazzolla, D Manfrin, M Manfredi, et al. 3d mixed reality holograms for preoperative surgical planning of nephron-sparing surgery: evaluation of surgeons' perception. *Minerva Urology and Nephrology*, 73(3):367–375, 2019.

[101] Sidney Roberts, Aditya Desai, Enrico Checcucci, Stefano Puliatti, Mark Taratkin, Karl-Friedrich Kowalewski, I Rivero, D Veneziano, R Autorino, F Porpiglia, et al. " augmented reality" applications in urology: a systematic review. *Minerva Urology and Nephrology*, 2022.

[102] C. He, Y. Liu, and Y. Wang. Sensor-fusion based augmented-reality surgical navigation system. In *2016 IEEE International Instrumentation and Measurement Technology Conference Proceedings*, pages 1–5, May 2016.

[103] Sara Condino, Giuseppe Turini, Paolo D Parchi, Rosanna M Viglialoro, Nicola Piolanti, Marco Gesi, Mauro Ferrari, and Vincenzo Ferrari. How to build a patient-specific hybrid simulator for orthopaedic open surgery: benefits and limits of mixed-reality using the microsoft hololens. *Journal of healthcare engineering*, 2018, 2018.

[104] Puxun Tu, Yao Gao, Abel J Lungu, Dongyuan Li, Huixiang Wang, and Xiaojun Chen. Augmented reality based navigation for distal interlocking of intramedullary nails utilizing microsoft hololens 2. *Computers in Biology and Medicine*, 133:104402, 2021.

[105] D.F. Ormerod, B. Ross, and A. Naluai-Cecchini. Use of an augmented reality display of patient monitoring data to enhance anesthesiologists' response to abnormal clinical events. *Studies in Health Technology and Informatics*, 94:248–250, 2003.

[106] Penelope M Sanderson, Marcus O Watson, Walter John Russell, Simon Jenkins, David Liu, Norris Green, Kristen Llewelyn, Phil Cole, Vivian Shek, and Stas S Krupenia. Advanced auditory displays and head-mounted displays: advantages and disadvantages for monitoring by the distracted anesthesiologist. *Anesthesia & Analgesia*, 106(6):1787–1797, 2008.

[107] Costin Cepisca, Felix Constantin Adochiei, Sabina Potlog, Cosmin Karl Banica, and George Calin Seritan. Platform for bio-monitoring of vital parameters in critical infrastructures operation. In *2015 7th International Conference on Electronics, Computers and Artificial Intelligence (ECAI)*, pages E–7. IEEE, 2015.

[108] Daniel McDuff, Christophe Hurter, and Mar Gonzalez-Franco. Pulse and vital sign measurement in mixed reality using a hololens. In *Proceedings of the 23rd ACM Symposium on Virtual Reality Software and Technology*, pages 1–9, 2017.

[109] Johnny Yau Cheung Chang, Lok Yee Tsui, Keith Siu Kay Yeung, Stefanie Wai Ying Yip, and Gilberto Ka Kit Leung. Surgical vision: Google glass and surgery. *Surgical innovation*, 23(4):422–426, 2016.

[110] Arindam Dey, Mark Billinghurst, Robert W Lindeman, and J Edward Swan. A systematic review of 10 years of augmented reality usability studies: 2005 to 2014. *Frontiers in Robotics and AI*, 5:37, 2018.

[111] Simon Moosburner, Christopher Remde, Peter Tang, Moritz Queisner, Nils Haep, Johann Pratschke, and Igor M Sauer. Real world usability analysis of two augmented reality headsets in visceral surgery. *Artificial organs*, 43(7):694–698, 2019.

[112] John Brooke. Sus: a "quick and dirty'usability. *Usability evaluation in industry*, 189(3), 1996.

[113] Bradley Herbert, Barrett Ens, Amali Weerasinghe, Mark Billinghurst, and Grant Wigley. Design considerations for combining augmented reality with intelligent tutors. *Computers & Graphics*, 77:166–182, 2018.

[114] Emanuele Marino, Loris Barbieri, Biagio Colacino, Anna Kum Fleri, and Fabio Bruno. An augmented reality inspection tool to support workers in industry 4.0 environments. *Computers in Industry*, 127:103412, 2021.

[115] Alvaro Alesanco and José García. Clinical assessment of wireless ECG transmission in real-time cardiac telemonitoring. *IEEE Transactions on Information Technology in Biomedicine*, 14(5):1144–1152, 2010.

[116] Thaha Muhammed, Rashid Mehmood, Aiiad Albeshri, and Iyad Katib. Ubehealth: a personalized ubiquitous cloud and edge-enabled networked healthcare system for smart cities. *IEEE Access*, 6:32258–32285, 2018.

[117] P. Arpaia, M. Cicatiello, E. De Benedetto, C. Anna Dodaro, L. Duraccio, G. Servillo, and M. Vargas. A health 4.0 integrated system for monitoring and predicting patient's health during surgical procedures. In *2020 IEEE International Instrumentation and Measurement Technology Conference (I2MTC)*, pages 1–6, 2020.

[118] Reed T Sutton, David Pincock, Daniel C Baumgart, Daniel C Sadowski, Richard N Fedorak, and Karen I Kroeker. An overview of clinical decision support systems: benefits, risks, and strategies for success. *NPJ digital medicine*, 3(1):17, 2020.

[119] Lorenzo Moja, Koren H Kwag, Theodore Lytras, Lorenzo Bertizzolo, Linn Brandt, Valentina Pecoraro, Giulio Rigon, Alberto Vaona, Francesca Ruggiero, Massimo Mangia, et al. Effectiveness of computerized decision support systems linked to electronic health records: a systematic review and meta-analysis. *American journal of public health*, 104(12):e12–e22, 2014.

[120] Muhammad Awais, Hemant Ghayvat, Anitha Krishnan Pandarathodiyil, Wan Maria Nabillah Ghani, Anand Ramanathan, Sharnil Pandya, Nicolas Walter, Mohamad Naufal Saad, Rosnah Binti Zain, and Ibrahima Faye. Healthcare professional in the loop (hpil): classification of standard and oral cancer-causing anomalous regions of oral cavity using textural analysis technique in autofluorescence imaging. *Sensors*, 20(20):5780, 2020.

[121] Per Trobisch, Olaf Suess, and Frank Schwab. Idiopathic scoliosis. *Deutsches Ärzteblatt International*, 107(49):875, 2010.

[122] Stefano Negrini, Angelo Gabriele Aulisa, Pavel Cerny, Jean Claude de Mauroy, Jeb McAviney, Andrew Mills, Sabrina Donzelli, Theodoros B Grivas, M Timothy Hresko, Tomasz Kotwicki, et al. The classification of scoliosis braces developed by sosort with srs, ispo, and posna and approved by esprm. *European Spine Journal*, 31(4):980–989, 2022.

[123] Joseph A Janicki and Benjamin Alman. Scoliosis: Review of diagnosis and treatment. *Paediatrics & child health*, 12(9):771–776, 2007.

[124] F Zaina, JC De Mauroy, T Grivas, MT Hresko, T Kotwizki, T Maruyama, N Price, M Rigo, L Stikeleather, J Wynne, et al. Bracing for scoliosis in 2014: state of the art. *European journal of physical and rehabilitation medicine*, 50(1):93–110, 2014.

[125] DL Carman, RH Browne, and JG Birch. Measurement of scoliosis and kyphosis radiographs. intraobserver and interobserver variation. *JBJS*, 72(3):328–333, 1990.

[126] Ming-Huwi Horng, Chan-Pang Kuok, Min-Jun Fu, Chii-Jen Lin, Yung-Nien Sun, et al. Cobb angle measurement of spine from x-ray images using convolutional neural network. *Computational and mathematical methods in medicine*, 2019, 2019.

[127] Stuart L Weinstein, Lori A Dolan, Jack CY Cheng, Aina Danielsson, and Jose A Morcuende. Adolescent idiopathic scoliosis. *The lancet*, 371(9623):1527–1537, 2008.

[128] Brian D Wishart and Emily Kivlehan. Neuromuscular scoliosis: when, who, why and outcomes. *Physical Medicine and Rehabilitation Clinics*, 32(3):547–556, 2021.

[129] Daniel Hedequist and John Emans. Congenital scoliosis. *JAAOS-Journal of the American Academy of Orthopaedic Surgeons*, 12(4):266–275, 2004.

[130] Manuel D Rigo, Mónica Villagrasa, and Dino Gallo. A specific scoliosis classification correlating with brace treatment: description and reliability. *Scoliosis*, 5(1):1–11, 2010.

[131] Theofanis Tsiligiannis and Theodoros Grivas. Pulmonary function in children with idiopathic scoliosis. *Scoliosis*, 7(1):7, 2012.

[132] Cristina Bignardi. Usefulness of measuring the pressure exerted by orthopedic braces. *International Journal of Engineering Research and Technology*, 12(12):2903–2909, 2019.

[133] Stefano Negrini, Sabrina Donzelli, Angelo Gabriele Aulisa, Dariusz Czaprowski, Sanja Schreiber, Jean Claude de Mauroy, Helmut Diers, Theodoros B Grivas, Patrick Knott, Tomasz Kotwicki, et al. 2016 sosort guidelines: orthopaedic and rehabilitation treatment of idiopathic scoliosis during growth. *Scoliosis and spinal disorders*, 13(1):1–48, 2018.

[134] B Stephens Richards, Robert M Bernstein, Charles R D'Amato, and George H Thompson. Standardization of criteria for adolescent idiopathic scoliosis brace studies: Srs committee on bracing and nonoperative management. *Spine*, 30(18):2068–2075, 2005.

[135] Stefano Negrini, Francesca Di Felice, Francesco Negrini, Giulia Rebagliati, Fabio Zaina, and Sabrina Donzelli. Predicting final results of brace treatment of adolescents with idiopathic scoliosis: First out-of-brace radiograph is better than in-brace radiograph—sosort 2020 award winner. *European Spine Journal*, 31(12):3519–3526, 2022.

[136] Stanislao Grazioso, Mario Selvaggio, Giuseppe Di Gironimo, and Roberto Ruggiero. Inbody: Instant photogrammetric 3d body scanner. In *Proceedings of the 7th International Conference on 3D Body Scanning Technologies, Lugano, Switzerland, 30 Nov–1 Dec*, pages 296–301, 2016.

[137] Stefano Negrini, Theodoros B Grivas, Tomasz Kotwicki, Manuel Rigo, Fabio Zaina, international Society on Scoliosis Orthopaedic, and Rehabilitation Treatment (SOSORT) stefano. negrini@ isico. it. Guidelines on" standards of management of idiopathic scoliosis with corrective braces in everyday clinics and in clinical research": Sosort consensus 2008. *Scoliosis*, 4:1–14, 2009.

[138] Patrick Knott, Eden Pappo, Michelle Cameron, Jean Claude deMauroy, Charles Rivard, Tomasz Kotwicki, Fabio Zaina, James Wynne, Luke Stikeleather, Josette Bettany-Saltikov, et al. Sosort 2012 consensus paper: reducing x-ray exposure in pediatric patients with scoliosis. *Scoliosis*, 9(1):4, 2014.

[139] JS Daruwalla and P Balasubramaniam. Moiré topography in scoliosis. its accuracy in detecting the site and size of the curve. *The Journal of Bone and Joint Surgery. British volume*, 67(2):211–213, 1985.

[140] Hideki Sudo, Terufumi Kokabu, Yuichiro Abe, Akira Iwata, Katsuhisa Yamada, Yoichi M Ito, Norimasa Iwasaki, and Satoshi Kanai. Automated noninvasive detection of idiopathic scoliosis in children and adolescents: A principle validation study. *Scientific reports*, 8(1):1–10, 2018.

[141] Pasquale Arpaia, Umberto Bracale, Francesco Corcione, Egidio De Benedetto, Alessandro Di Bernardo, Vincenzo Di Capua, Luigi Duraccio, Roberto Peltrini, and Roberto Prevete. Assessment of blood perfusion quality in laparoscopic colorectal surgery by means of machine learning. *Scientific Reports*, 12(1):14682, 2022.

[142] Gilbert Gaussorgues and Seweryn Chomet. *Infrared thermography*, volume 5. Springer Science & Business Media, 1993.

[143] Carosena Meola and Giovanni M Carlomagno. Recent advances in the use of infrared thermography. *Measurement science and technology*, 15(9):R27, 2004.

[144] Vladan Bernard, Erik Staffa, Vojtěch Mornstein, and Aleš Bourek. Infrared camera assessment of skin surface temperature–effect of emissivity. *Physica Medica*, 29(6):583–591, 2013.

[145] Bryan F Jones and Peter Plassmann. Digital infrared thermal imaging of human skin. *IEEE engineering in medicine and biology magazine*, 21(6):41–48, 2002.

[146] Roque Alfredo Osornio-Rios, Jose Alfonso Antonino-Daviu, and Rene de Jesus Romero-Troncoso. Recent industrial applications of infrared thermography: A review. *IEEE transactions on industrial informatics*, 15(2):615–625, 2018.

[147] André Chrysochoos. Infrared thermography applied to the analysis of material behavior: a brief overview. *Quantitative InfraRed Thermography Journal*, 9(2):193–208, 2012.

[148] Roselyne Ishimwe, K Abutaleb, Faruk Ahmed, et al. Applications of thermal imaging in agriculture—a review. *Advances in remote Sensing*, 3(03):128, 2014.

[149] Steven I Rekant, Mark A Lyons, Juan M Pacheco, Jonathan Arzt, and Luis L Rodriguez. Veterinary applications of infrared thermography. *American journal of veterinary research*, 77(1):98–107, 2016.

[150] Andrew McBride, Swantje Bargmann, Damien Pond, and Georges Limbert. Thermoelastic modelling of the skin at finite deformations. *Journal of thermal biology*, 62:201–209, 2016.

[151] Oliver Faust, U Rajendra Acharya, EYK Ng, Tan Jen Hong, and Wenwei Yu. Application of infrared thermography in computer aided diagnosis. *Infrared Physics & Technology*, 66:160–175, 2014.

[152] Lampropoulos Georgios, Siakas Kerstin, and Anastasiadis Theofylaktos. Internet of things in the context of industry 4.0: An overview. 2019.

[153] Shogo Hayashi, Koichi Kawanishi, Isao Ujike, and Pang-Jo Chun. Development of cloud computing system for concrete structure inspection by deep learning based infrared thermography method. In *ISARC. Proceedings of the International Symposium on Automation and Robotics in Construction*, volume 37, pages 927–934. IAARC Publications, 2020.

[154] B Jesenšek Papež, Miroslav Palfy, and Zmago Turk. Infrared thermography based on artificial intelligence for carpal tunnel syndrome diagnosis. *Journal of International Medical Research*, 36(6):1363–1370, 2008.

[155] JW Germi, KG Mensah-Brown, HI Chen, and JM Schuster. Use of smartphone-integrated infrared thermography to monitor sympathetic dysfunction as a surgical complication. *Interdisciplinary Neurosurgery*, 28:101475, 2022.

[156] CL Romanò, N Logoluso, F Dell'Oro, A Elia, and L Drago. Telethermographic findings after uncomplicated and septic total knee replacement. *The Knee*, 19(3):193–197, 2012.

[157] Sebastian Scheidt, Julian Rüwald, Frank Alexander Schildberg, Anne Katrin Mahlein, Axel Seuser, Dieter Christian Wirtz, and Cornelius Jacobs. A systematic review on the value of infrared thermography in the early detection of periprosthetic joint infections. *Zeitschrift für Orthopädie und Unfallchirurgie*, 158(04):397–405, 2020.

[158] Subramnaiam Bagavathiappan, John Philip, Tammana Jayakumar, Baldev Raj, Pallela Narayana Someshwar Rao, Muthukrishnan Varalakshmi, and Viswanathan Mohan. Correlation between plantar foot temperature and diabetic neuropathy: a case study by using an infrared thermal imaging technique. *Journal of diabetes science and technology*, 4(6):1386–1392, 2010.

[159] Jen-Hong Tan, EYK Ng, U Rajendra Acharya, and Caroline Chee. Infrared thermography on ocular surface temperature: a review. *Infrared physics & technology*, 52(4):97–108, 2009.

[160] Joaquín Martín Marzano-Felisatti, Anna Martinez-Amaya, and José Ignacio Priego-Quesada. Preliminary analysis of skin temperature asymmetries in elite young tennis players. *Applied Sciences*, 13(1):628, 2023.

[161] Pedro Gómez-Carmona, Ismael Fernández-Cuevas, Manuel Sillero-Quintana, Javier Arnaiz-Lastras, and Archit Navandar. Infrared thermography protocol on reducing the incidence of soccer injuries. *Journal of sport rehabilitation*, 29(8):1222–1227, 2020.

[162] Anna Lubkowska and Ewa Gajewska. Temperature distribution of selected body surfaces in scoliosis based on static infrared thermography. *International Journal of Environmental Research and Public Health*, 17(23):8913, 2020.

[163] Garcia Kwok, Joanne Yip, Kit-Lun Yick, Mei-Chun Cheung, Chi-Yung Tse, Sun-Pui Ng, and Ameersing Luximon. Postural screening for adolescent idiopathic scoliosis with infrared thermography. *Scientific reports*, 7(1):1–8, 2017.

[164] Davide Felice Redaelli, Valentina Abbate, Fabio Alexander Storm, Alfredo Ronca, Andrea Sorrentino, Cristina De Capitani, Emilia Biffi, Luigi Ambrosio, Giorgio Colombo, and Paolo Fraschini. 3d printing orthopedic scoliosis braces: a test comparing fdm with thermoforming. *The International Journal of Advanced Manufacturing Technology*, 111(5-6):1707–1720, 2020.

[165] Wensheng Shen, Jun Zhang, and Fuqian Yang. Modeling and numerical simulation of bioheat transfer and biomechanics in soft tissue. *Mathematical and Computer Modelling*, 41(11-12):1251–1265, 2005.

[166] FLIR ONE Pro - iOS. https://www.flir.it/products/flir-one-pro/?vertical=condition+monitoring&segment=solutions. Accessed: 2023-07-08.

[167] Sebastian Raschka. Model evaluation, model selection, and algorithm selection in machine learning. *arXiv preprint arXiv:1811.12808*, 2018.

[168] E M Donnachie, D W Seccombe, N I Urquhart, C H Scudamore, C R Shackleton, A D Foreward, and S Erb. Indocyanine green interference in the Kodak Ektachem determination of total bilirubin. *Clinical Chemistry*, 35(5):899–900, 05 1989.

[169] Richard Benya, Joseph Quintana, and Bruce Brundage. Adverse reactions to indocyanine green: a case report and a review of the literature. *Catheterization and cardiovascular diagnosis*, 17(4):231–233, 1989.

[170] Gilbert R Cherrick, Samuel W Stein, Carroll M Leevy, Charles S Davidson, et al. Indocyanine green: observations on its physical properties, plasma decay, and hepatic extraction. *The Journal of clinical investigation*, 39(4):592–600, 1960.

[171] P Faybik and H Hetz. Plasma disappearance rate of indocyanine green in liver dysfunction. In *Transplantation proceedings*, volume 38, pages 801–802. Elsevier, 2006.

[172] Paola De Nardi, Ugo Elmore, Giulia Maggi, Riccardo Maggiore, Luigi Boni, Elisa Cassinotti, Uberto Fumagalli, Marco Gardani, Stefano De Pascale, Paolo Parise, et al. Intraoperative angiography with indocyanine green to assess anastomosis perfusion in patients undergoing laparoscopic colorectal resection: results of a multicenter randomized controlled trial. *Surgical endoscopy*, 34(1):53–60, 2020.

[173] Jun Watanabe, Atsushi Ishibe, Yusuke Suwa, Hirokazu Suwa, Mitsuyoshi Ota, Chikara Kunisaki, and Itaru Endo. Indocyanine green fluorescence imaging to reduce the risk of anastomotic leakage in laparoscopic low anterior resection for rectal cancer: a propensity score-matched cohort study. *Surgical endoscopy*, 34(1):202–208, 2020.

[174] Hiro Hasegawa, Yuichiro Tsukada, Masashi Wakabayashi, Shogo Nomura, Takeshi Sasaki, Yuji Nishizawa, Koji Ikeda, Tetsuo Akimoto, and Masaaki Ito. Impact of intraoperative indocyanine green fluorescence angiography on anastomotic leakage after laparoscopic sphincter-sparing surgery for malignant rectal tumors. *International journal of colorectal disease*, 35(3):471–480, 2020.

[175] Christoph Schwarz, Immanuel Plass, Fabian Fitschek, Antonia Punzengruber, Martina Mittlböck, Stephanie Kampf, Ulrika Asenbaum, Patrick Starlinger, Stefan Stremitzer, Martin Bodingbauer, et al. The value of indocyanine green clearance assessment to predict postoperative liver dysfunction in patients undergoing liver resection. *Scientific reports*, 9(1):1–7, 2019.

[176] Hokuto Ushijima, Junichiro Kawamura, Kazuki Ueda, Yoshinori Yane, Yasumasa Yoshioka, Koji Daito, Tadao Tokoro, Jin-ichi Hida, and Kiyotaka

Okuno. Visualization of lymphatic flow in laparoscopic colon cancer surgery using indocyanine green fluorescence imaging. *Scientific Reports*, 10(1):1–7, 2020.

[177] Giovanni Merola, Antonio Sciuto, Felice Pirozzi, Jacopo Andreuccetti, Giusto Pignata, Francesco Corcione, Marco Milone, Giovanni Domenico De Palma, Rossana Castaldo, Leandro Pecchia, et al. Is robotic right colectomy economically sustainable? a multicentre retrospective comparative study and cost analysis. *Surgical endoscopy*, 34(9):4041–4047, 2020.

[178] Hong-min Ahn, Gyung Mo Son, In Young Lee, Sang-Ho Park, Nam Su Kim, and Kwang-Ryul Baek. Optimization of indocyanine green angiography for colon perfusion during laparoscopic colorectal surgery. *Colorectal Disease*, 23(7):1848–1859, 2021.

[179] Wei Zhang and Xu Che. Effect of indocyanine green fluorescence angiography on preventing anastomotic leakage after colorectal surgery: a meta-analysis. *Surgery Today*, 51(9):1415–1428, 2021.

[180] Sameh Hany Emile, Sualeh Muslim Khan, and Steven D Wexner. Impact of change in the surgical plan based on indocyanine green fluorescence angiography on the rates of colorectal anastomotic leak: a systematic review and meta-analysis. *Surgical Endoscopy*, pages 1–13, 2022.

[181] Luigi Boni, Giulia David, Gianlorenzo Dionigi, Stefano Rausei, Elisa Cassinotti, and Abe Fingerhut. Indocyanine green-enhanced fluorescence to assess bowel perfusion during laparoscopic colorectal resection. *Surgical endoscopy*, 30(7):2736–2742, 2016.

[182] Jeffrey Dalli, Eamon Loughman, Niall Hardy, Anwesha Sarkar, Mohammad Faraz Khan, Haseeb A Khokhar, Paul Huxel, Donal F O'Shea, and Ronan A Cahill. Digital dynamic discrimination of primary colorectal cancer using systemic indocyanine green with near-infrared endoscopy. *Scientific Reports*, 11(1):1–12, 2021.

[183] Roberto Peltrini, Mauro Podda, Simone Castiglioni, Maria Michela Di Nuzzo, Michele D'Ambra, Ruggero Lionetti, Maurizio Sodo, Gaetano Luglio, Felice Mucilli, Salomone Di Saverio, et al. Intraoperative use of indocyanine green fluorescence imaging in rectal cancer surgery: The state of the art. *World Journal of Gastroenterology*, 27(38):6374, 2021.

[184] Toshiaki Wada, Kenji Kawada, Ryo Takahashi, Mami Yoshitomi, Koya Hida, Suguru Hasegawa, and Yoshiharu Sakai. Icg fluorescence imaging for quantitative evaluation of colonic perfusion in laparoscopic colorectal surgery. *Surgical endoscopy*, 31(10):4184–4193, 2017.

[185] Jörg Zehetner, Steven R DeMeester, Evan T Alicuben, Daniel S Oh, John C Lipham, Jeffrey A Hagen, and Tom R DeMeester. Intraoperative assessment of perfusion of the gastric graft and correlation with anastomotic leaks after esophagectomy. *Annals of surgery*, 262(1):74, 2015.

[186] M Diana, V Agnus, P Halvax, Y-Y Liu, B Dallemagne, A-I Schlagowski, B Geny, P Diemunsch, V Lindner, and J Marescaux. Intraoperative fluorescence-based enhanced reality laparoscopic real-time imaging to assess bowel perfusion at the anastomotic site in an experimental model. *Journal of British Surgery*, 102(2):e169–e176, 2015.

[187] Christian D Lütken, Michael P Achiam, Morten B Svendsen, Luigi Boni, and Nikolaj Nerup. Optimizing quantitative fluorescence angiography for visceral perfusion assessment. *Surgical Endoscopy*, pages 1–11, 2020.

[188] Vivek Kaul, Sarah Enslin, and Seth A Gross. The history of artificial intelligence in medicine. *Gastrointestinal endoscopy*, 2020.

[189] Chayakrit Krittanawong, Albert J Rogers, Mehmet Aydar, Edward Choi, Kipp W Johnson, Zhen Wang, and Sanjiv M Narayan. Integrating blockchain technology with artificial intelligence for cardiovascular medicine. *Nature Reviews Cardiology*, 17(1):1–3, 2020.

[190] Stan Benjamens, Pranavsingh Dhunnoo, and Bertalan Meskó. The state of artificial intelligence-based fda-approved medical devices and algorithms: an online database. *NPJ digital medicine*, 3(1):1–8, 2020.

[191] Yong Wang, Mengqi Ji, Shengwei Jiang, Xukang Wang, Jiamin Wu, Feng Duan, Jingtao Fan, Laiqiang Huang, Shaohua Ma, Lu Fang, et al. Augmenting vascular disease diagnosis by vasculature-aware unsupervised learning. *Nature Machine Intelligence*, 2(6):337–346, 2020.

[192] Leon von der Emde, Maximilian Pfau, Chantal Dysli, Sarah Thiele, Philipp T Möller, Moritz Lindner, Matthias Schmid, Monika Fleckenstein, Frank G Holz, and Steffen Schmitz-Valckenberg. Artificial intelligence for morphology-based function prediction in neovascular age-related macular degeneration. *Scientific reports*, 9(1):1–12, 2019.

[193] Domenico Parmeggiani, Nicola Avenia, Alessandro Sanguinetti, Roberto Ruggiero, Giovanni Docimo, Mattia Siciliano, Pasquale Ambrosino, Imma Madonna, Roberto Peltrini, and Umberto Parmeggiani. Artificial intelligence against breast cancer (annes-bc-project). *Ann Ital Chir*, 83(1):1–5, 2012.

[194] Alistair Martin, Jama Nateqi, Stefanie Gruarin, Nicolas Munsch, Isselmou Abdarahmane, Marc Zobel, and Bernhard Knapp. An artificial intelligence-based first-line defence against covid-19: digitally screening citizens for risks via a chatbot. *Scientific reports*, 10(1):1–7, 2020.

[195] Stuart Keel, Pei Ying Lee, Jane Scheetz, Zhixi Li, Mark A Kotowicz, Richard J MacIsaac, and Mingguang He. Feasibility and patient acceptability of a novel artificial intelligence-based screening model for diabetic retinopathy at endocrinology outpatient services: a pilot study. *Scientific reports*, 8(1):1–6, 2018.

[196] Zhi Zhen Qin, Melissa S Sander, Bishwa Rai, Collins N Titahong, Santat Sudrungrot, Sylvain N Laah, Lal Mani Adhikari, E Jane Carter, Lekha Puri, Andrew J Codlin, et al. Using artificial intelligence to read chest radiographs for tuberculosis detection: A multi-site evaluation of the diagnostic accuracy of three deep learning systems. *Scientific reports*, 9(1):1–10, 2019.

[197] Maria Amodeo, Vincenzo Abbate, Pasquale Arpaia, Renato Cuocolo, Giovanni Dell'Aversana Orabona, Monica Murero, Marco Parvis, Roberto Prevete, and Lorenzo Ugga. Transfer learning for an automated detection system of fractures in patients with maxillofacial trauma. *Applied Sciences*, 11(14):6293, 2021.

[198] Andrew J Steele, Spiros C Denaxas, Anoop D Shah, Harry Hemingway, and Nicholas M Luscombe. Machine learning models in electronic health records can outperform conventional survival models for predicting patient mortality in coronary artery disease. *PloS one*, 13(8):e0202344, 2018.

[199] RA Cahill, DF O'shea, MF Khan, HA Khokhar, JP Epperlein, PG Mac Aonghusa, R Nair, and SM Zhuk. Artificial intelligence indocyanine green (icg) perfusion for colorectal cancer intra-operative tissue classification. *British Journal of Surgery*, 108(1):5–9, 2021.

[200] Sang-Ho Park, Hee-Min Park, Kwang-Ryul Baek, Hong-Min Ahn, In Young Lee, and Gyung Mo Son. Artificial intelligence based real-time microcirculation analysis system for laparoscopic colorectal surgery. *World Journal of Gastroenterology*, 26(44):6945, 2020.

[201] Takahiro Igaki, Daichi Kitaguchi, Shigehiro Kojima, Hiro Hasegawa, Nobuyoshi Takeshita, Kensaku Mori, Yusuke Kinugasa, and Masaaki Ito. Artificial intelligence-based total mesorectal excision plane navigation in laparoscopic colorectal surgery. *Diseases of the Colon & Rectum*, 65(5):e329–e333, 2022.

[202] Luisa F Sánchez-Peralta, Luis Bote-Curiel, Artzai Picón, Francisco M Sánchez-Margallo, and J Blas Pagador. Deep learning to find colorectal polyps in colonoscopy: A systematic literature review. *Artificial intelligence in medicine*, 108:101923, 2020.

[203] Daichi Kitaguchi, Nobuyoshi Takeshita, Hiroki Matsuzaki, Tatsuya Oda, Masahiko Watanabe, Kensaku Mori, Etsuko Kobayashi, and Masaaki Ito. Automated laparoscopic colorectal surgery workflow recognition using artificial intelligence: Experimental research. *International Journal of Surgery*, 79:88–94, 2020.

[204] Rui Yao, Shixiong Xia, Fumin Shen, Yong Zhou, and Qiang Niu. Exploiting spatial structure from parts for adaptive kernelized correlation filter tracker. *IEEE Signal Processing Letters*, 23(5):658–662, 2016.

[205] Zijun Zhang. Improved adam optimizer for deep neural networks. In *2018 IEEE/ACM 26th International Symposium on Quality of Service (IWQoS)*, pages 1–2. IEEE, 2018.

[206] Sebastian Bock and Martin Weiß. A proof of local convergence for the adam optimizer. In *2019 International Joint Conference on Neural Networks (IJCNN)*, pages 1–8. IEEE, 2019.

[207] Sylvain Arlot, Alain Celisse, et al. A survey of cross-validation procedures for model selection. *Statistics surveys*, 4:40–79, 2010.

[208] Statistics Calculators. Statistics Kingdom. http://www.statskingdom.com.